Alma Mater Studiorum · Università di Bologna

Scuola di Scienze
Corso di Laurea Magistrale in Fisica

EXPERIMENTAL SET UP AND CHARACTERIZATION OF A PROTOTYPE FOR BREAST MICROWAVE IMAGING

Relatore:
Prof. Nico Lanconelli

Presentata da:
Federico Nanetti

Correlatori:
Dott. Simone Masetti
Dott. Massimiliano Grandi

Sessione III
Anno Accademico 2014/2015

Abstract

Nella presente tesi è stato sviluppato un sistema di acquisizione automatico finalizzato allo studio del breast microwave imaging.

Partendo da un sistema preesistente, è stata creata una struttura meccanica studiata per ospitare la strumentazione necessaria all'acquisizione dei dati e alla movimentazione del fantoccio che rappresenta il tessuto mammario. Le misure sono state eseguite in configurazione monostatica, in cui viene acquisito un segnale da diverse posizioni lungo il perimetro dell'area di indagine. A questo scopo, è stato installato un motore ad alta precisione che, in sinergia con un VNA a cui è collegata una antenna dipolo di tipo "sleeve", permette la rotazione del fantoccio e l'esecuzione automatica delle misure da un numero di posizioni fissato. Per automatizzare il processo di acquisizione, è stato inoltre sviluppato appositamente un software in ambiente LabView, che permette di selezionare i parametri necessari per eseguire la misura tramite interfaccia grafica.

Successivamente, è stata eseguita una intensa sessione di misure finalizzate alla caratterizzazione del sistema sviluppato al variare delle condizioni di misura. Inizialmente, è stato selezionato un range di frequenze ottimale in cui eseguire le misure, partendo da considerazioni sul funzionamento dell'antenna e sulla corretta ricostruzione delle immagini. Abbiamo quindi utilizzato dei fantocci di tumore di diverse dimensioni e permittività elettrica per studiare la sensibilità della strumentazione in condizione di mezzo omogeneo. Dall'analisi delle ricostruzioni multifrequenza effettuate tramite diversi algoritmi di tipo TR-MUSIC sul range di frequenze selezionato, abbiamo notato che il tumore è ricostruito correttamente in tutti gli scenari testati.

Inoltre, abbiamo creato un ulteriore fantoccio per simulare la presenza di una disomogeneità nel dominio di imaging. In questo caso, abbiamo studiato le performances del sistema di acquisizione al variare della posizione del tumore, le cui caratteristiche sono state fissate, e della permittività associata al fantoccio. Dall'analisi dei risultati appare chiaro che le performances di ricostruzione sono significativamente condizionate dalla presenza della disomogeneità, in modo particolare se il tumore è posizionato all'interno di essa.

Infine, abbiamo eseguito un'ultima sessione di misure finalizzata allo studio delle performance di due algoritmi di ricostruzione 3D: uno di essi è basato sulla sovrapposizione tomografica e sfrutta metodi di interpolazione, l'altro si basa sull'utilizzo di un propagatore 3D per il dipolo Hertziano in approssimazione scalare. A questo scopo,

sono state effettuate misure a diverse profondità, sia in mezzo omogeneo che eterogeneo. Analizzando i risultati prodotti dai due algoritmi, abbiamo notato che nel primo caso si ottiene una ricostruzione ad alto contrasto a discapito della risoluzione lungo l'asse verticale, mentre nel secondo metodo si ottiene un contrasto molto ridotto e una buona risoluzione verticale.

Abstract

In the present thesis, it was developed an automatic acquisition system aimed at the study of microwave breast imaging.

Starting from an existing system, it was created a mechanical structure designed to accommodate the necessary equipment for data acquisition and handling of the the breast phantom. The measurements were performed in monostatic configuration, where a signal is acquired from different positions along the perimeter of the imaging area. For this purpose, a high-precision engine has been installed, in synergy with a VNA to which is connected an antenna dipole of "sleeve" type. This instrumentation allows the rotation of the phantom antenna and the automatic execution of the measures from a fixed number of positions . To automate the process of acquisition, it was also specifically developed a LabView software, which allows to select the parameters needed to perform measurement through a graphical interface.

Subsequently, an intense session of measures aimed at the characterization of the system developed was performed, under varying measurement conditions. Initially, a range of optimum frequencies was selected in which measurements were performed, starting from considerations on the antenna features and the correct reconstruction of the images. We then used tumor phantoms of different sizes and electrical permittivity to study the sensitivity of the instrumentation in homogeneous-medium condition. From the analysis of multifrequency reconstructions made through different TR-MUSIC-like algorithms on the selected frequency range, we noticed that the tumor is correctly reconstructed in all tested scenarios.

In addition, we have created an additional phantom to simulate the presence of an inhomogeneity in the imaging domain. In this case, we studied the performances of the acquisition system varying the position of the tumor, of fixed size and dielectric parameter, and the permittivity associated to the inhomogeneous phantom. From the analysis of the results, it appears that the reconstruction performance is significantly influenced by the presence of inhomogeneities, particularly if the tumor is positioned inside of it.

Finally, we performed the last session of measures aimed at the study of the performance of two 3D reconstruction algorithms: one of them is based on the tomographic overlap and uses interpolation methods, the other is based on the use of a 3D propagator for the Hertzian dipole scalar approximation. For this purpose, measurements were carried out at different depths, both in homogeneous and heterogeneous

medium. Analyzing the results produced by the two algorithms, we noticed that in the first case is obtained a high contrast reconstruction with a low resolution along the vertical axis, while the second method produces a low contrast image characterized by a good vertical resolution.

Contents

Chapter 1

Introduction

1.1 Motivations

Since breast cancer is the most widespread kind of tumor diagnosed in women worldwide, it is necessary and important to detect it as soon as possible. Sadly, breast cancer is also the paramount cause of cancer death in women, therefore the importance of identification and prevention is becoming indispensable. This is the main reason why more and more countries are implementing screening protocols.

Breast cancer screening is the medical screening of asymptomatic and apparently healthy women for breast cancer in an attempt to achieve an earlier diagnosis. The assumption is that early detection will improve the final outcome.

Many different approaches are employed to detect tumors properly, i.e., X-ray mammography, Magnetic Resonance Imaging (MRI) and Ultrasounds. Despite their recognized value in screening procedures, they have peculiar limitations that motivate further studies to improve precision and reduce invasiveness of diagnostic tools available to radiologists.

In this thesis, Microwave Imaging will be discussed. It is a new imaging technique based on electromagnetic waves in the microwave frequency range developed over the last decades by different research groups in order to outdo limits of current breast cancer screening methods. Microwave Imaging exploits the dielectric contrast between normal and malignant breast tissues that should be greater than X-ray mammography.

1.2 The Value of Prevention

Cancer constitutes an enormous burden on society in more and less economically developed countries alike. The occurrence of cancer is increasing because of the growth and aging of the population, as well as an increasing prevalence of established risk factors such as smoking, overweight, physical inactivity and environment changing due to urbanization and economic development. According to GLOBOCAN[1] estimates, about 14.1 million new cancer cases and 8.2 million deaths occurred in 2012 worldwide. Over the years, the burden has shifted to less developed countries, which currently account for about 57% of cases and 65% of cancer deaths worldwide [1]. The most commonly diagnosed tumor is the lung cancer (1.8 million new cases in 2012), and it has overtaken breast cancer as the main cause of cancer death among females in more developed countries (Figure 1.1).

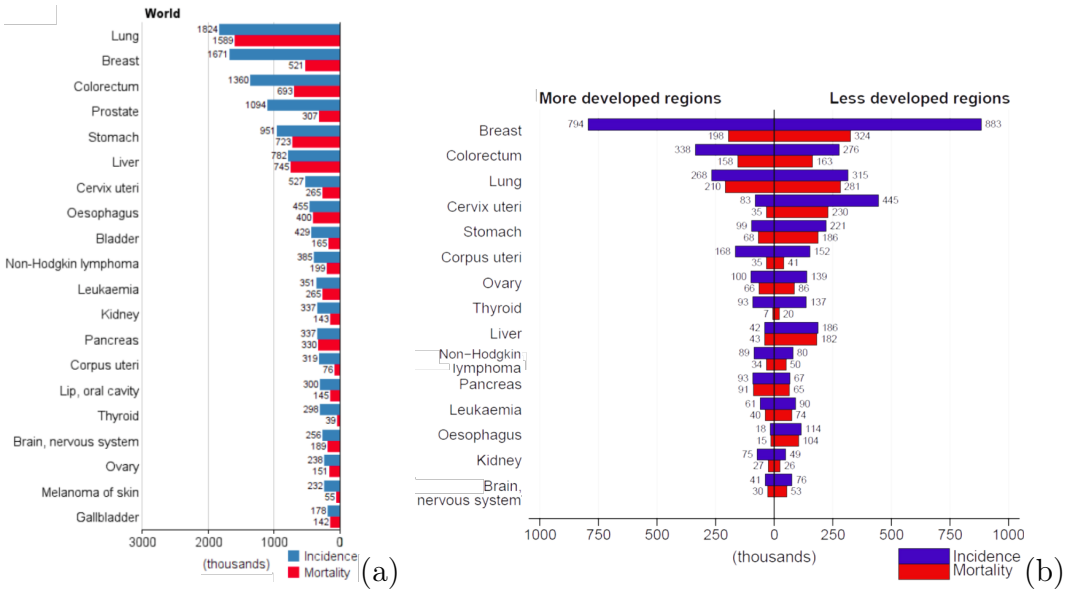

Figure 1.1: (a) Cancer Incidence and mortality rates by World Area, all ages. (b) Estimated numbers (thousands) of new cancer cases and mortality (female population) in more and less developed regions of the world in 2012 [2].

As concerns worldwide female population, breast cancer emerged as the most frequently diagnosed cancer, counting almost 1.7 million cases and 521,900 deaths in 2012. In Italy, breast cancer affects 13% of women and represents the 29% of female cancer cases [3].

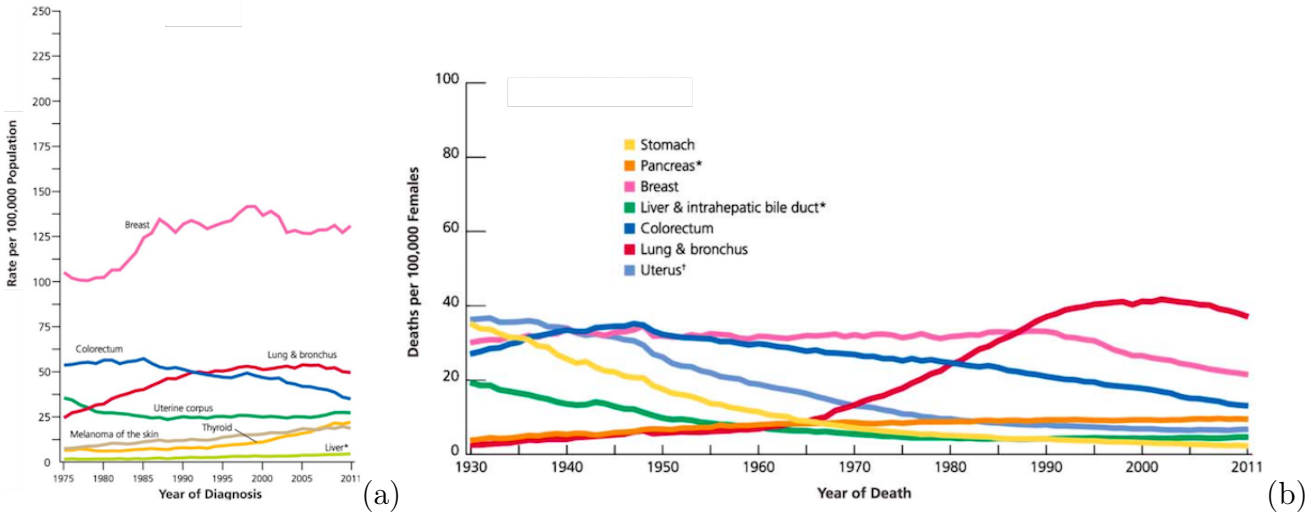

Figure 1.2: Trends in Incidence (a) and Death (b) rates for selected cancers in female population, United States, 1975 to 2011 [4].

Figure 1.2a illustrates long-term trends in cancer incidence rates for selected cancer sites in the female population. Cancer incidence patterns in the United States reflect behavioral trends and improvements in cancer prevention and control, as well as changes in medical practice. The boost in breast cancer incidence in the early 1980s probably reflects the increased diagnoses due to introduction of mammography screening and changes in reproductive patterns. Figure 1.2b shows a decreasing trend in death rates due to breast cancer. Even if it showed a smoothly increasing trend in the past (1975-1990), breast cancer death rate has been decreasing constantly for women of all ages. Declines in breast cancer mortality have been attributed to both improvements in treatment and early detection. In spite of this, breast cancer still remain the most commont cancer in female population, and the probability of developing is highly age-correlated (it goes from 1.9% in females younger than 49 years to 6.7% in females older than 70, reaching the incidence of 12.3% over the birth-to-death period). It's worth noticing that breast cancer affects also male population, even if in a marginal frequency (about 1% of new cases and deaths) [4].

In the light of this, it clearly appears that a substantial portion of cancer deaths could be prevented by broadly applying effective prevention measures. It follows that the most important prerequisite for an effective therapy is an early diagnosis. Early detection tests and treatment of breast cancer can arrest disease progression, decrease the rate of advanced cancers, and reduce breast cancer mortality in the screened population.

When high quality breast screenings are offered at regular intervals to women

aged from 40- to 74-year-old, over 50% of the invasive cancers will be detected in the size range of 1-14mm, fewer than 20% will be axillary node positive, and only about 20% will be poorly differentiated [5].

1.3 Complementary Imaging Techniques

A big number of tests have been employed for breast cancer diagnosis, including clinical and self breast exams, mammography, ultrasound, and magnetic resonance imaging. A clinical or self breast exam involves feeling the breast for lumps or other abnormalities. These tests are recommended and bring benefits in the prevention of breast cancer. Medical evidence, however, does not support its use in women with a typical risk for breast cancer, so they should be integrated with more accurate screening tests.

1.3.1 X-ray Mammography

X-ray mammography is currently the golden standard for breast cancer screening [5]. Despite of this, X-ray mammography doesn't provide totally reliable outcomes.

Mammography is a non-invasive medical test which uses low-energy X-rays, tipically around 20 keV, in order to examine human breast.

Equipment for mammography has evolved over at least the last 40 years to the current state of the art. While there are some differences from one manufacturer to another, there are also many characteristics and features that are common to all (Figure 1.3):

- X-ray Tube Anode: mammography equipment uses molybdenum and tungsten as the anode material or in some designs, a dual material anode with an additional rhodium track, they produce a characteristic radiation spectrum that is close to optimum for breast imaging.
- Filter: whereas most x-ray machines use aluminium or "aluminium equivalent" to filter the x-ray beam to reduce unnecessary exposure to the patient, in addition mammography uses molybdenum filters to enhance contrast sensitivity.
- Focal Spots: the typical x-ray tube for mammography has two selectable focal spots.
- Grid: a grid is used in mammography (as in other X-ray procedures) to absorb scattered radiation and improve contrast sensitivity.

· Receptor: Both film/screen and digital receptors are used for mammography. Each has special characteristics to enhance image quality.

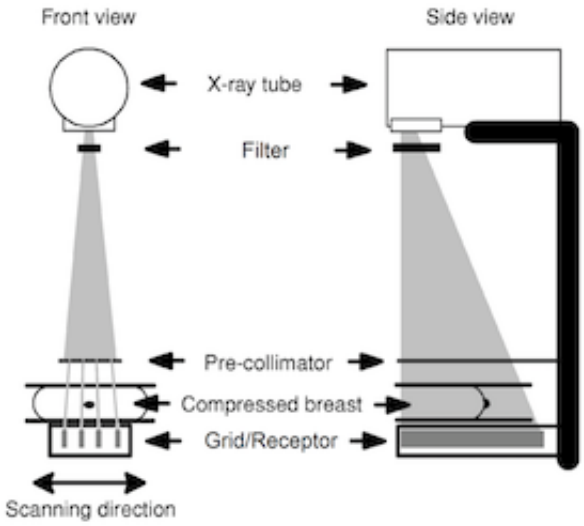

Figure 1.3: Principal components of a mammography system.

Being realtively fast and low-cost, mammography has become an accessible exam in the last decades. The death rate suddenly began a steady decline since its adoption. Despite of this, mammography suffers from its own limitations. The rate of failure (false negative) in detecting breast cancer is relatively high, it can vary from 4/100 to 34/100 [6]. In a large-scale study, a total of 9762 screening mammograms were performed, with a median of 4 mammograms per woman over a past 10-year period. Of the women who were screened, 23.8% had at least one false positive mammogram and the estimated cumulative risk of a false positive result was 49.1% after 10 mammograms [7].

Furthermore, this technique involves ionizing rays wich represent a worrisome risk for women's health capable of increasing the chance of tumor growth [8]. This is caused by the exposition of the breast to a small dose (about 0.4 mSv) of ionizing radiation.

Also, investigations performed by this approach are often painful because require breast compression in order to produce a better result, since compression reduces blurring due to patient motion and improves contrast sensitivity

1.3.2 Breast Ultrasound

Ultrasound Imaging, also called ultrasound scanning or sonography, is a safe and painless method to produce pictures of the inside of the body using sound waves. It involves the use of a small transducer (probe) and ultrasound gel placed directly on the skin. High-frequency sound waves are transmitted from the probe through the gel into the body. The ultrasound wave travels through different tissues at different speeds. The point at which adjacent tissues with different speeds of sound meet is referred to as an acoustic interface. This technique exploits the creation of an echo when sound hits an acustic interface. The transducer collects the sounds that bounce back and a computer then uses those sound waves to create an image.

Since this screening method doesn't use ionizing radiation, there is no radiation exposure for the patient. Also, it is a non-invasive and painless test. Because ultrasound images are captured in real-time, they can show the structure and movement of the body's internal organs, as well as blood flowing through blood vessels.

Sadly, a major limitation of ultrasound is that breast fat and most cancer cells have similar acoustic properties, which makes detecting many tumors impossible with ultrasound. As a result, ultrasound primarily remains a tool for distinguishing cysts from solid tumors and for guiding biopsy procedures. Nevertheless, ultrasound has been used in breast cancer detection with a false negative rate of 17/100, but highly specialized doctors are required to perform the exams [9].

1.3.3 Breast MRI

An alternative technique for breast cancer detection is the MRI. Magnetic Resonance Imaging exploits the interaction of Radio Frequency (RF) energy and magnetic fields with the magnetic properties of certain atoms to produce high resolution images. A strong magnet is first used to align the protons of the nucleus (tipically hydrogen), and then pulsed RF energy is used to tip the protons out of alignment. Once the RF pulse ends, protons return to alignment (T_1 relaxation) and begin to precess at different rates (T_2 relaxation) emitting a RF signal that is detected by MR device. Imaging is possible because these return signals vary in phase and intensity based on the strength of the magnetic field, the frequency and pattern of the RF pulses, and the properties of the tissue. By encoding location information using magnetic field gradients and different sequences of RF pulses, the tissue properties at each location can be mapped to form high resolution 3D images.

In this method, images are acquired before and after the intravascular injection of

a contrast agent (Gadolinium Diethylene Triamine Pentaacetic Acid (DTPA)). The first images are subctracted from the seconds, and any areas that have increased blood flow are seen as bright spots on a dark background. Since breast cancers generally have an increased blood supply, the contrast agent causes these lesions to "light up" on the images.

Despite it is proved that MRI is the only availabe technique to detected some types of breast cancers, MRI suffers from a high false positive rate. A previous study showed that MRI had a specificity of only 95.4%, compared to 96%, 99.3%, and 99.8% for ultrasound, clinical breast exam, and mammography, respectively [10].

This low specificity, along with the high costs associated with MR imaging, limit MRI's usefulness. Therefore, MRI is not currently used for breast cancer screening except for high risk cases [11].

1.3.4 Optical Imaging

Optical breast imaging is a novel imaging technique that uses near-infrared light to assess the optical properties of breast tissue.

Optical breast imaging uses near-infrared light in the wavelength range of 600–1000 nm to assess the optical properties of tissue. Functional information on tissue components can be obtained by combining images acquired at various wavelengths. When using only intrinsic breast tissue contrast in optical breast imaging, this is referred to as optical breast imaging without contrast agent. The other modality, i.e. optical breast imaging with a contrast agent, uses exogenous fluorescent probes that target molecules specific for breast cancer. The use of fluorescent probes has great potential in early breast cancer detection, since in vivo imaging of molecular changes associated with breast cancer formation is technically feasible. Additional advantages of optical breast imaging are that it uses no ionizing radiation and it is relatively inexpensive, which can lead to repeated use (also in young women) and easy access to the technique [12].

Chapter 2

Microwave Imaging

2.1 A Brief Overview

The opening of microwave imaging in biomedical applications was performed by Larsen and Jacobi in 1978 [13], developing a water-immersed antenna for biomedical applications. This was the first time someone was able to penetrate a biological object with microwaves to create images of the internal structures. From those results a major interest have been focused on microwave imaging in biomedical applications [14]. Since the dielectric properties of biological tissues are highly temperature dependent, the initial focus was on remote measurements of internal temperature. Today, one of the most recent applications is the research of a new imaging system to diagnose breast cancer. The allure of this approach is chiefly due to the absence of ionizing radiations. Secondary, compared to mammography and MRI, it offers other advantages such as the elimination of breast compression and the cost reduction.

As concerns the performance, it has been supposed that in the range of microwave frequencies there is a notable contrast between normal and malignant breast tissues, not inferior to the radiographic density (X-ray mammography) [15, 16, 17], acoustic impedance (Ultrasound) and nuclear spin relaxation (MRI).

The physical principle on which the microwave imaging is based upon is the electromagnetic field reflection when an inhomogeneity in the constitutive electromagnetic parameters (i.e. permittivity and conductivity) is present.

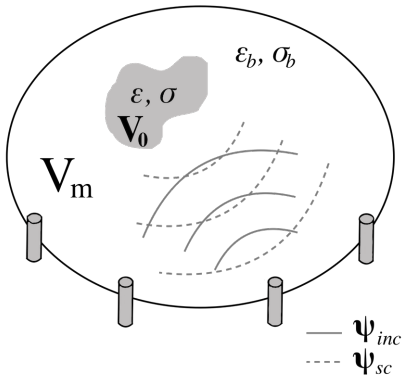

Figure 2.1: In a microwave imaging system, the system of antennas irradiate a background medium with ε_b and σ_b in which is embedded a target with ε and σ. V_0 and V_m are respectively the target and the domain volume.

In Figure 2.1 the microwave imaging system is sketched out. The circular area in the center of the antenna group represents the imaging domain, that is irradiated by a transmitting antenna and the total field may be measured by one or more antennas positioned outside the domain. When an object with contrast in the dielectric parameters is positioned inside the imaging domain, a scattered field will arise. The receiving antennas will measure a total field equals to the sum of the incident and scattered fields:

$$\psi^{tot}(\mathbf{r}) = \psi^{inc}(\boldsymbol{r}) + \psi^{sc}(\mathbf{r}) \tag{2.1}$$

where $\mathbf{r}$ denotes position vector, $\psi^{sc}(\boldsymbol{r})$ denotes the scattered field and represents the interaction between the incident field and the target, $\psi^{tot}(\boldsymbol{r})$ represents the perturbated field. This field is clearly different from the field generated by the source when the object is not present, which is indicated as incident or unperturbated field $\psi^{inc}(\boldsymbol{r})$. The incident field is a known quantity if the source is completely characterized. Thus, when a scattering object (usually termed *scatterer*) is introduced, the measured field changes, and information about location or constitutive parameters of the scattering object may be obtained.

Two situations usually occur. In the first one, called *direct scattering problem*, the object is completely known. The goal is the computation of the scattered fields $\psi^{sc}(\boldsymbol{r})$ everywhere, knowing all the other quantities, such as $\psi^{inc}(\boldsymbol{r})$, $\forall \boldsymbol{r} \in \mathbb{R}$, the background's ($\varepsilon_b$, σ_b) and target's (ε, σ) dielectric parameters, the space region V_0 occupied by the object. In this approach, the following Fredhol linear integral equation of the second kind (Equation 2.2) must be solved in order to compute the total

electric field vector $\psi^{tot}(\boldsymbol{r})$ for every $\boldsymbol{r}$ inside and outsite V_0, which is the only unknown,

$$\psi^{tot}(\mathbf{r}) = \psi^{inc}(\boldsymbol{r}) + j\omega\sigma_b \int_{V_0} \tau(\mathbf{r'})\psi(\mathbf{r'})G(\mathbf{r},\mathbf{r'})d\mathbf{r'} \tag{2.2}$$

where $\tau(\mathbf{r}) = j\omega[\varepsilon(\mathbf{r}) - \varepsilon_b]$ is the *scattering potetial.*

In the second situation considered, called *inverse scattering problem*, which is a more realistic scenario, one has to infer information on the unkown object from an arbitrary number of measurements of the perturbed field generally collected outside the object. For the free-space configuration considered, in this second approach, $\psi^{inc}(\boldsymbol{r})$, $\forall \boldsymbol{r} \in \mathbb{R}$ and the background's (ε_b, σ_b) dielectric parameters are still assumed to be known. Moreover, it is assumed that the total electric field $\psi^{tot}(\boldsymbol{r})$ is a known quantity (e.g., obtained by suitable measurements) only for $\boldsymbol{r} \notin V_0$. On the other hand, the location and the dielectric parameters of the target are unknown quantities and the goal is to determine them. The solution of the inverse problem consists in identifying the physical object that produces the external measured scattered field distribution in V_m consistent with the known incident field in V_0. In this second case, we exploit the Fredholm (data) equation of the first find defined as follows

$$\psi^{tot}(\mathbf{r}) = \psi^{inc}(\boldsymbol{r}) + j\omega\sigma_b \int_{V_0} \tau(\mathbf{r'})\psi(\mathbf{r'})G(\mathbf{r},\mathbf{r'})d\mathbf{r'} \tag{2.3}$$

$\mathbf{r} \in V_m$ which is formally similar to Equation 2.2, but now the field is known everywhere outside V_0

Also, another (state) equation realted to the internal field distribution must be solved, which describes the equivalent current density as

$$\mathbf{J}^{eq}(\mathbf{r}) = \tau(\mathbf{r})\psi^{inc}(\boldsymbol{r}) + j\omega\sigma_b\tau(\mathbf{r}) \int_{V_0} \mathbf{J}^{eq}(\mathbf{r'})G(\mathbf{r},\mathbf{r'})d\mathbf{r'} \tag{2.4}$$

$\mathbf{r} \in V_0$ [18].

Further considerations about the inverse scattering problem will be presented in Chapeter 3.2.

2.2 Breast Anatomy

The breast (Figure 2.2) is a modified skin gland that lies on the chest wall, usually between the clavicle and the sixth rib, and is bounded externally by skin and internally by the pectoralis muscle. Breast tissue also extends up into the axilla via

a pyramidal-shaped axillary tail. The breast tissue primarily consists of a combination of fat and glandular tissue, with the relative proportions of the two varying widely. The remainder of the breast is made up of connective tissue, vascular tissue, lymphatics, and nerves.

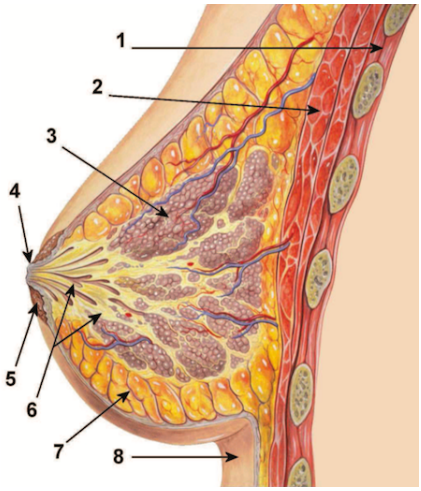

Figure 2.2: Anatomy of the Breast: 1. Chest wall 2. Pectoralis muscles 3. Lobules 4. Nipple 5. Areola 6. Ducts 7. Fatty tissue 8. Skin.

Skin and Connective Tissue

The breast is supported by a combination of connective tissue and skin, whose thickness varies between 0.8mm and 3mm. The skin also contains the nipple, which is slightly below the centerpoint of the breast and extends about 5-10mm above the skin surface, and the surrounding areola, which contains small bumps called Montgomery's glands. Finally, the breast is supported by a surrounding layer of connective tissues, which is interspersed with the subcutaneous and retromammary adipose tissue, and suspensory ligaments that provide an internal supporting framework for the breast lobes.

Adipose Tissue

The adipose tissue in the breast can be divided into three main groups: subcutaneous, retromammary, and intraglandular. The first two regions form a layer between the majority of the glandular tissue and the external boundaries of the breast. The majority of cancers develop in the region of glandular tissue within 1 cm of these fat layers.

Glandular Tissue

The glandular tissue in the breast consists of a number of discrete lobes, which are made up of *lobules* and *ducts*. There are approximately 15-20 lobes in each breast, and each lobe is thought to be exclusively drained by its own individual duct system. Within a lobe there are dozens of lobules 2-3 mm in diameter, and within each lobule there are as many as 100 alveoli, which are the basic secretory units of the breast.

Other tissues are present inside human breast, like Vascular, Nerve and Lymphatic tissues, which respectively provide blood supply, receptors and lymph fluid drainage.

2.3 Electrical Properties of Human Breast Tissue

Large differences exist in dielectric properties of biological materials. These differences are determined, to a large extent, by the fluid content of the material. For example, blood and brain conduct electric current relatively well. Lungs, skin, fat and bone are relatively poor conductors. Liver, spleen, and muscle are intermediate in their conductivities. In this section, the dielectric properties of human breast tissues will be discussed in order to explain the principles of microwave imaging [19].

In Microwave Imaging the dielectric properties are reconstructed regarding the differences in the *complex permittivity*, while non-metallic materials are considered in biomedical applications, defined by Equation 2.5:

$$\varepsilon_r = \varepsilon' - j\varepsilon'' \tag{2.5}$$

where $j = \sqrt{-1}$ is imaginary unit, $\varepsilon\prime$ describes the polarization effects of charged particles in the tissue and $\varepsilon\prime\prime$ describes the out-of-phase losses due to the displacement currents generated by the applied electromagnetic field. Considering the biological tissues as dielectrics, the losses often are described by the *conductivity* σ, which is approximated to the displacement current effect only, as Equation 2.6:

$$\sigma = 2\pi\nu\varepsilon_0\varepsilon'' \tag{2.6}$$

where $\varepsilon_0 = \frac{10^{-9}}{36\pi}\frac{\mathrm{F}}{\mathrm{m}}$ is the permittivity of free space and ν is the frequency. The dielectric properties are determined as $\varepsilon\prime$ and $\varepsilon\prime\prime$, or $\varepsilon\prime$ and σ,

$$\varepsilon_r = \varepsilon' - j\frac{\sigma}{2\pi\nu\varepsilon_0} \tag{2.7}$$

as function of the frequency.

In the microwave region the dominant relaxation is the dipolar relaxation of polar molecules (i.e. water and many proteins). Therefore, the dielectric properties of the tissues in microwave region are highly correlated to the water content. Permanent dipoles of polar biological molecules are randomly oriented, but if an external electric field is applied, they will reorient statistically and the induced dipoles will follow the direction of the applied field. The rotational force exerted by the field on a permanent dipole is defined by the torque:

$$\vec{M} = q\vec{L} \times \vec{E} \tag{2.8}$$

where q is the charge, $\vec{L}$ is charge separation, and $\vec{E}$ is the electric field strength.

The rotation of polar molecules in an applied electric field requires time, hence, causes a dispersion occurs. Equation 2.9 is valid for this kind of dispersion and it describes any one-time constant relaxation mechanism. However, a distribution of time constants will often be found due to molecular inhomogeneity and nonspherical shape. The time constant is proportional to the cube of the radius of the molecules, and typical characteristic frequencies are, e.g., 15-20 GHz for water and 400-500 MHz for simple amino acids. Proteins add another dispersion typically centered in the 1-10 MHz range [20].

Gabriel *et al.* [21, 22, 23, 24] made a major review of measured dielectric properties together with own measurements on healthy human tissues, in order to physical model human tissues for frequencies between 10 Hz–10 GHz. They showed that relative dielectric permittivity and conductivity of high-water-content tissues (i.e., muscle and malignant tumors) are about an order of magnitude greater than those of low-water-content tissues (i.e., fat and normal breast tissue). In Figure 2.3, it is shown the comparison of the conductivity of high-water-content tissue with low-water-content tissue. In both cases conductivity and relative permittivity were greater in malignant tissue than in normal tissue of the same type, especially at frequencies below 1 GHz. This suggests that microwave imaging is theoretically possible at many frequencies, and that the choice of frequency is largely a matter of balancing the added spatial resolution afforded by higher frequencies with the additional attenuation that comes with it.

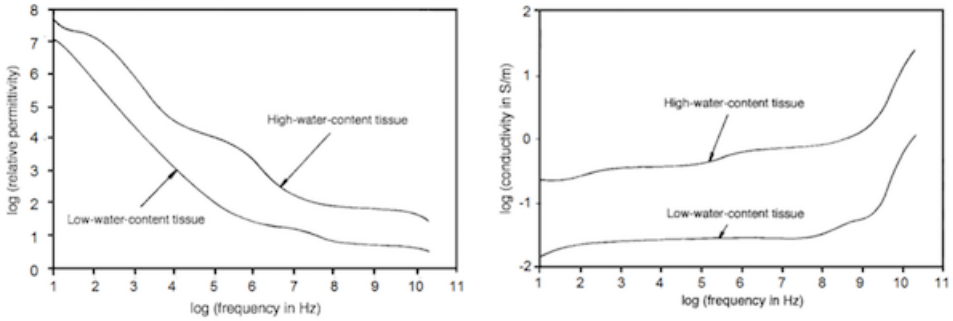

Figure 2.3: Comparison of permittivity and conductivity of high-water-content tissue with low-water-content tissue as a function of frequency [21, 22, 23, 24].

The basic model is the Debye expression in Equation 2.9:

$$\varepsilon_r = \varepsilon_\infty + \frac{\Delta\varepsilon}{1 + j2\pi\nu\tau} - j\frac{\sigma}{2\pi\nu\varepsilon_0} \tag{2.9}$$

where $\Delta\varepsilon = \varepsilon_s - \varepsilon_\infty$, τ is the time constant of the relaxation mechanism, ε_∞ is the permittivity at frequencies $2\pi\nu\tau \gg 1$, ε_s the permittivity at $2\pi\nu\tau \ll 1$.

Figure 2.4 shows the fit of dielectric properties of normal and cancerous tissues exploiting Debye model, over a spread frequency spectrum.

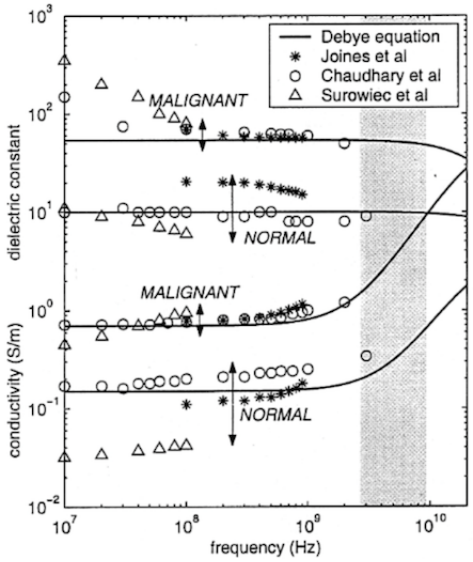

Figure 2.4: Single-pole Debye curve fits of measured baseline dielectric properties data for normal and malignant breast tissue at radio and microwave frequencies [16].

Due to the complexity of the structure and composition of biological tissues, Lazebnik *et al.* [25, 26] performed a large scale study in order to experimentally

characterize the dielectric properties of a significant number of normal breast tissues and malignant tissues, from 0.5 to 20 GHz. The study of distributions of sample tissue compositions demonstrates that the dielectric properties of breast tissue are primarily determined by the adipose content of the tissue sample (Figure 2.5). Furthermore, secondary factors such as patient age, tissue temperature and time between excision and measurement had only negligible effects on the observed dielectric properties. Also, the dielectric constant and effective conductivity values for normal breast tissue reported in this study span a much larger range than those reported in most of previous smaller-scale studies. In contrast with normal tissue, the dielectric properties of malignant tissues are high and span a relatively small range.

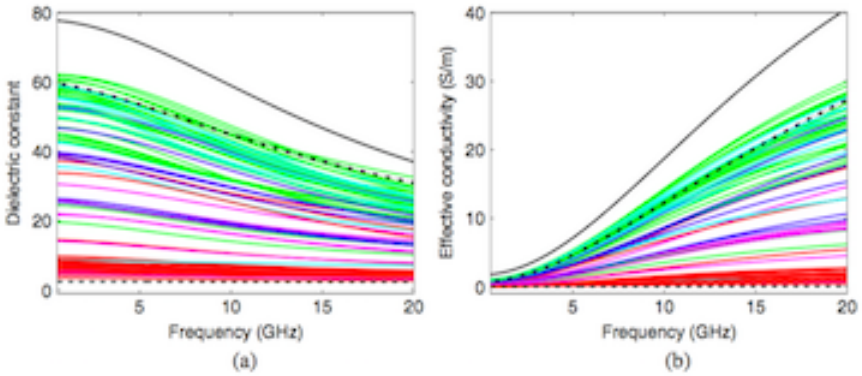

Figure 2.5: One-pole Cole–Cole fits to the 85 normal data sets. The curves are color coded based on the amount of adipose tissue present in each sample. The solid black (upper) curve represents the dielectric properties of saline, the dashed black (lower) curve represents the dielectric properties of lipids, and the dash-dot black (middle) curve represents the dielectric properties of blood. [26]

In addition, Lazebnik *et al.* found the dielectric properties for the groups: low adipose tissue content (0-30%), median adipose (31-84%), high adipose (85-100%), and cancer tissue. Dielectric constant and effective conductivity dispersion curves (Figures 2.6) are obtained for each group by fitting the data with single pole Cole-Cole model:

$$\varepsilon_r = \varepsilon_\infty + \frac{\Delta\varepsilon}{1 + (j2\pi\nu\tau)^{1-\alpha}} + j\frac{\sigma}{2\pi\nu\varepsilon_0} \tag{2.10}$$

The Cole-Cole Model offers an efficient and accurate representation of many types of biological tissues over a very wide frequency band and has been used to reduce the complexity of the experimental data obtained for various human breast tissues (brain, fat, breast, skin, bone, etc.) .

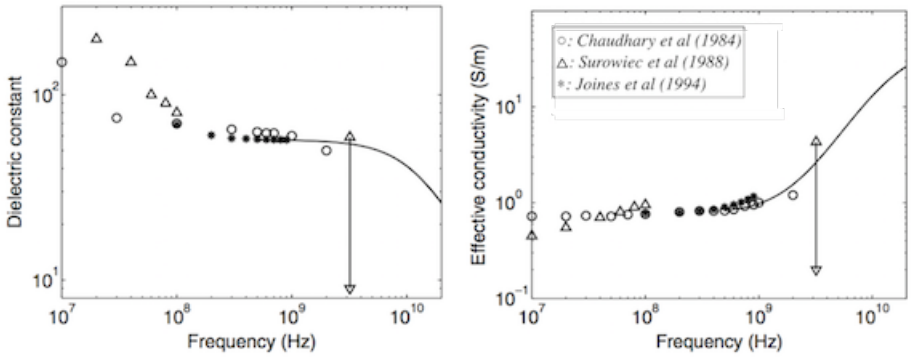

Figure 2.6: Comparison of data obtained from single-pole Debye curve fits with previous studies. Lines: median dielectric properties of the cancer samples with 30% or greater malignant tissue content. Vertical arrows: range of data reported by Campbell and Land (1992) at 3.2 GHz for malignant tissues. [26]

Median dielectric constant and effective conductivity dispersion curves were obtained for each group by first calculating the fitted values for each sample in the group at 50 equally spaced frequency points. Second, the median value at each frequency point was calculated across samples within the group. Finally, the Cole–Cole model was fit to these median values. The resulting 'median curves' fit the median values very well in all cases (Figure 2.7). In order to ensure that no systematic bias was present in the dielectric-properties characterization of the normal tissue samples obtained from cancer surgeries, these curves were compared with the curves obtained in the same manner from breast reduction surgeries.

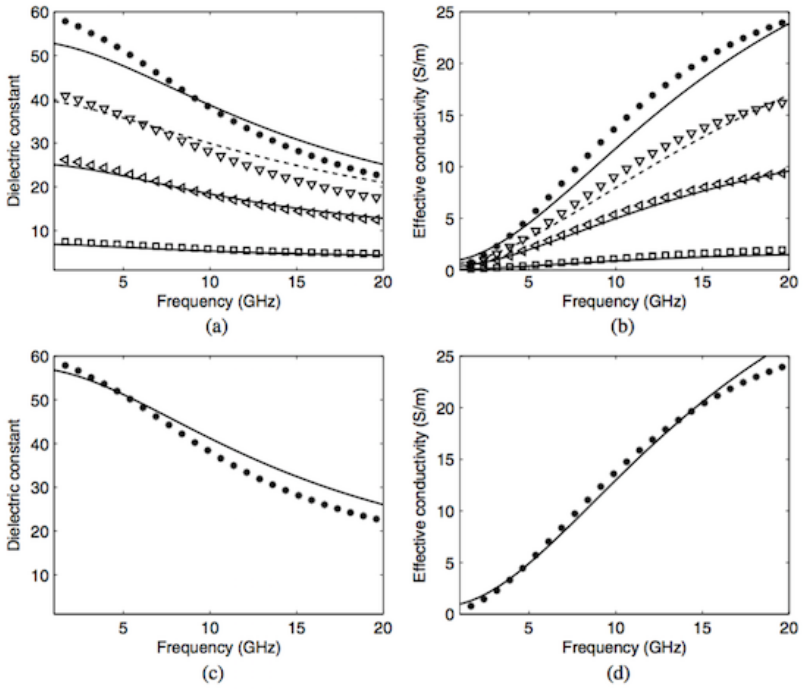

Figure 2.7: Comparison of median Cole–Cole curves for normal and malignant tissue with measured dielectric properties of tissue-mimicking phantom materials ([27]). (a) and (b) Dielectric constant and effective conductivity, respectively, for the three adipose-defined normal tissue groups. Solid lines: median Cole–Cole curves for normal tissue samples obtained from cancer surgeries (in the order of highest to lowest dielectric properties: group 1, group 2 and group 3). Dashed lines: median Cole–Cole curves for group 2 for normal tissue samples obtained from reduction surgeries. (c) and (d) Median Cole–Cole curves for the dielectric constant and effective conductivity, respectively, of cancer samples with minimum malignant tissue content of 30%. Symbols: measured dielectric properties of TM phantom materials ($*$, 10% oil; $\bigtriangledown$, 30% oil; $\triangleleft$, 50% oil; $\square$, 80% oil). [26]

They concluded that the contrast in the microwave-frequency dielectric properties between malignant and normal adipose-dominated tissues in the breast is considerable, as large as 10:1, while the contrast in the microwave-frequency dielectric properties between malignant and normal glandular/fibroconnective tissues in the breast is no more than about 10% (Table 2.1).

	ε_∞	$\triangle\varepsilon$	τ(ps)	α	σ_S(S/m)
Maximum	1.000	66.31	7.585	0.063	1.370
Glandular-high	6.151	48.26	10.26	0.049	0.809
Glandular-median	7.821	41.48	10.66	0.047	0.713
Glandular-low	9.941	26.60	10.90	0.003	0.462
Fat-high	4.031	3.654	14.12	0.055	0.083
Fat-median	3.140	1.708	14.65	0.061	0.036
Fat-low	2.908	1.200	16.88	0.069	0.020
Minimum	2.293	0.141	16.40	0.251	0.002
Malignant	9.058	51.31	10.84	0.022	0.889

Table 2.1: Single-Pole Cole–Cole parameters for normal [28] and malignant tissue [29] over the frequency band (3–10) GHz.

2.4 State of Art of MWI prototypes

Over the last decads, different prototipe systems for microwave imaging have been developed by various research groups. These systems are conceptually simple and can be divided in three main parts:

- An antenna array, which consists of a set of antennas properly arranged to be in contact directly with the breast or through a coupling liquid;
- Front-end circuits for generating and acquiring microwave signals. Between antennas and front-end circuits a switch matrix is connected, that allows individual activation of antennas;
- Back-end processing system for image reconstruction.

In many cases, the antennas have been developed and customized for the specific application, whereas the switch matrix and the front-end electronics use commercial components and a Vector Network Analyzer (VNA). In none of the cases custom integrated circuits have been developed for the specific application, even though the advancement of CMOS technology would permit nowadays to build those high-frequency components, to integrate them in order to reduce the bill of materials, and to simplify the connection between the antennas and the front-end. As for the back-end, a personal computer has been used, even if the reconstruction algorithms need high calculation capacity. This choice is allowed because most of the studies concern research prototypes, often tested with phantoms, in which processing performance is not the main goal.

The first MWI system for breast cancer detection (Figure 2.8) appeared in 2000 and was the first used in clinical environments [30]. That system was the precursor of various MWI systems developed in the following years. A significant limitation in dealing with microwave signals is the dynamic range needed to reliably acquire the weak signal originated by the tumor. This dynamic range is almost 100-120 dB, and it was quite difficult to achieve several years ago with commercial VNAs. This is one of the reasons why in the Dartmouth prototype the VNA was replaced by ad-hoc designed circuits, yet still using commercially available components [30]. Moreover, the crosstalk between different channels is another key parameter. An isolation of 100 dB is mandatory and it seems doable nowadays with commercial VNAs.

After this first prototype, various research groups built their own prototypes, which are listed here and some of them are presented in the following sections:

· Dartmouth college (USA)

· Politecnico di Torino (Italy)

· Chalmers University (Sweden)

· University of Bristol (UK)

· Technical University of Denmark (Denmark)

· University of Calgary (Canada)

· Shizuoka University (Japan)

· Electronics and Telecommunications Research Institute (ETRI, South Korea)

· University of Lisboa (Portugal).

Despite the great deal of work that has been done on microwave breast cancer imaging, most of the methods mentioned above have been mainly checked against synthetic data or under controlled laboratory conditions. In the first case numerical breast models of increasing complexity as the research progressed have been used. Now, breast models are directly derived from MR images. In the second case, laboratory phantom, 2D and 3D, mimicking the breast tissues have been used in laboratory.

2.4.1 Dartmouth College

This clinical prototype was the first prototype for microwave imaging breast analysis ever developed [30]. It provided useful information on the dielectric properties of breast tissues. From a technical point of view, the electronics circuits used were relatively old (it was the year 2000), but the building of such a system was quite an achievement. The system was developed to work at relatively low frequencies (300MHz-1GHz) and used an antenna array, front end electronics placed under the patient bed, and a PC for elaborating and visualizing the image. The analysis employed a tomographic technique.

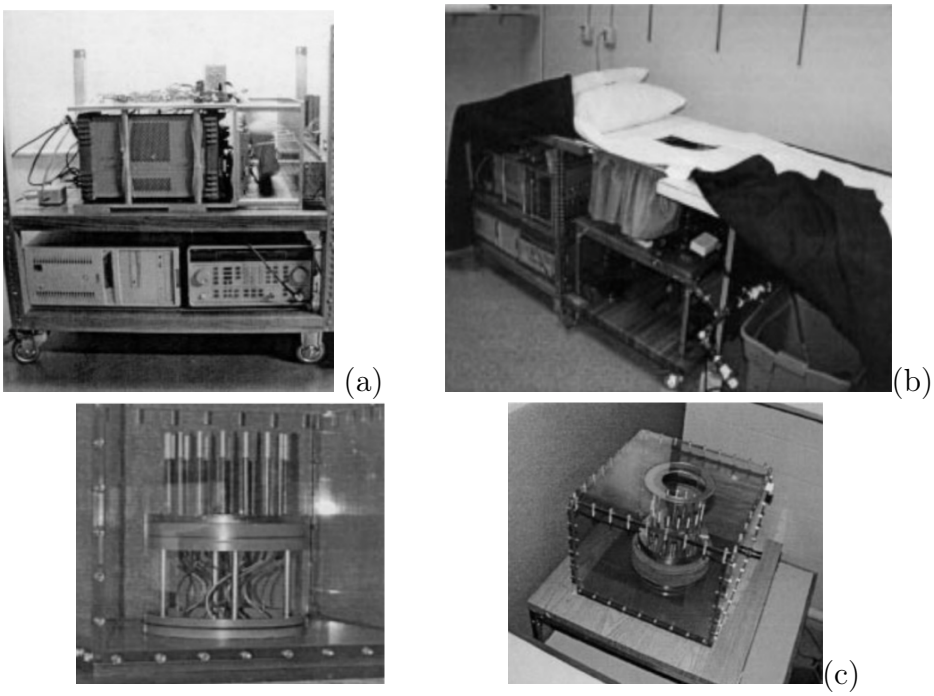

Figure 2.8: Different parts of the first MWI developed at Dartmouth College: (a) front-end electronics, (b) gurney and (c) antennas array.

16 vertical monopole antennas were used. Antennas protruded through the middle of the tank, with the radiating elements surrounding the breast on a 15-cm diameter. Each antenna was designed to work both as receiver and transmitter, maximizing the circuit flexibility. The liquid used as interface inside the tank was a saline solution. The antenna array and the tank are placed on a cart to be easily moved under the patient bed. The antenna array was connected with the front-end electronics (Figure 2.8a). The front-end was based on a heterodyne receiver, a 200-kHz A/D board, a function generator, a microwave source, while signal phase and amplitude extraction were performed in software with a Dell 300-MHz PC. The system was designed to

support up to 32 antennas through an electronic switch matrix that provides isolation greater than 120 dB and an overall linear dynamic range of 130 dB. An HP85070B Dielectric Probe Kit in conjunction with an HP 8753C Network Analyzer and a Dell Dimension 466V PC were used instead for system calibration. The whole system was placed on its own cart located under the patient bed.

The system was improved in 2005 (Meaney et al. 2005). The modulation scheme was again based on a superheterodyne approach and the frequency range was increased to 500MHz-3GHz. The radiofrequency signal was modulated and sent through an electronic switch matrix to 16 antennas. The same radiofrequency signal without modulation was sent to 16 transceiver boards through power dividers. The illumination tank and the antenna array were similar to the previous prototype. Signals generated by each transceiver were sampled by a National Instruments data acquisition board, and sent to a PC for image visualization. When the board works in transmitter mode, the modulated radiofrequency signal is sent directly to the antenna. When it works in receiver mode the signal received by the antenna is sent to the mixer for being demodulated.

Using this device and further improvements, 80 patients with abnormal mammograms and 50 patients with normal mammograms have been considered. The electrical permittivity and conductivity in the region of interest (ROI), the region which was suspicious in the mammogram, were reconstructed using the measured microwave data. The electrical permittivity and conductivity in the ROI were then compared to the background permittivity and conductivity outside the ROI in the ipsilateral breast (the breast with the suspicious legion) and to the mirrored ROI in the contralateral breast (the other breast). In the normal patients pseudo-ROI were selected. The results showed that cancerous tumors more than 1 cm in diameter exhibited twice as large conductivity in comparison to the background tissue. This ratio was statistically larger than that of benign tumors or that exhibited by healthy patients.

2.4.2 Politecnico di Torino - LACE Prototype

The microwave imaging system developed by LACE group of Politecnico di Torino is composed of the following parts:

· VNA

· Tank filled with coupling liquid

· Antenna array

This prototype uses 8 antennas (Figure 2.9a) interfaced with the breast through a tank (Figure 2.9b) containing a liquid used to reduce the unwanted reflections from the tank walls. In this prototype (which was not meant for clinical use) alcohol has been used as coupling liquid because of its optimal properties (from a microwave point of view): the return loss measured for the used antenna is below -10 dB from 0.5 GHz up to 5 GHz. Thinking to a clinical application, this is not the best choice. A possible mixture could be a bath composed of glycerin and water in different proportions. This liquid is not hazardous for the patient, and provides a good mechanical contact. The antenna (Figure 2.9c) is a simple monopole designed to work immersed in a liquid. It exhibits wideband behavior from few hundreds of MHz up to few GHz. A multi input VNA is used to generate and acquire microwave signals.

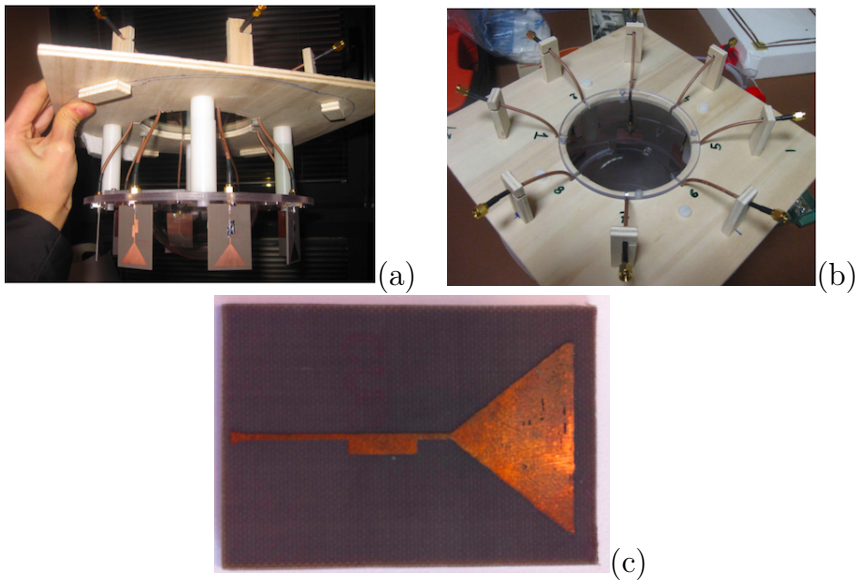

Figure 2.9: PoliTo-LACE prototype: (a) antenna array, (b) array with liquid tank and (c) monopole antenna.

2.4.3 Technical University of Denmark

This prototype for microwave imaging developed at Technical University of Denmark is based on a 3D nonlinear inverse scattering algorithm. The antenna array is made of 32 horizontally aligned monopole antennas (Figure 2.11b) in a cylindrical setup with a radius of 8 cm. Antennas are organized in a 3D volume to provide a 3-dimensional picture of the breast (Figure 2.10). These antennas are immersed in a tank filled with a glycerin-water mixture.

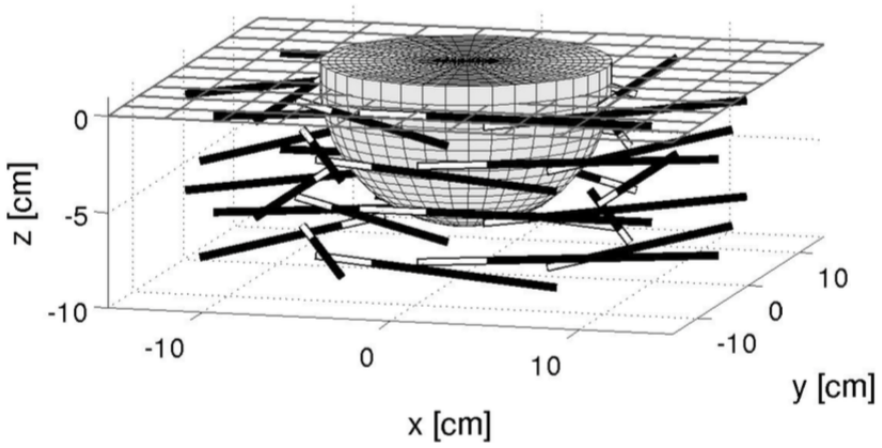

Figure 2.10: Antennas position in the prototype developed at the Technical University of Denmark.

The system works between 500 MHz and 3 GHz and each antenna operates both as transmitter and receiver. The electronics front-end uses instead custom electronics. Every antenna is connected to its own transceiver module (Figure 2.11a). The transceiver contains a low noise amplifier and a radiofrequency amplifier. The signal received from the antenna is amplified and then mixed with the local oscillator signal. A value of 1 KHz is chosen as intermediate frequency. The signals generated by the transceiver modules are then fed to 18-bit Analog-To-Digital (ADC) converters with built in 10 KHz low pass filters. The total measurement time with this set up is 2 minutes for each breast.

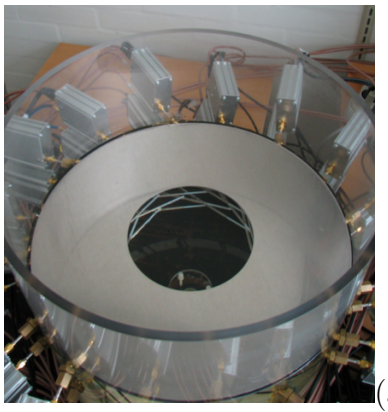
(a)

(b)

Figure 2.11: (a) Antenna array, tank and transceiver modules; (b) Detail of a monopole antenna.

The clinical results of this microwave imaging system provided qualitative agree-

ment with the images obtained by X-ray mammography for certain patients.

2.4.4 University of Lisboa

University of Lisboa realized a tumor classification exploiting a pre-clinical UWB prototype imaging system developed at the University of Manitoba (Canada). The system is composed of a Field Fox N9923A VNA by Agilent Technology, a Vivaldi antenna which is connected to the VNA through a 50-ohm cable and is attached to the inner part of a Plexiglas tank filled with canola oil (Figure 2.12).

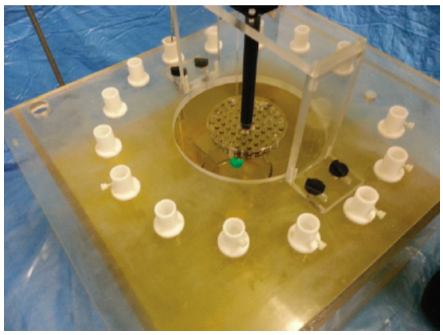

Figure 2.12: Microwave system developed at the University of Manitoba.

The breast phantom consists of a styrene-acrylonitril cylinder with a diameter of 13 cm and an height of 35 cm filled with glycerin, while the tumor phantoms were emulated with a mix of TX151 solidifying powder and water. A set of 13 benign and 13 malignant tumors (Figure 2.13) with a diameter ranging from 13 mm to 40 mm were considered for the classification. Spiculated and microlobulated shapes emulate the malignant tumors, while the spheres represent the benign tumors.

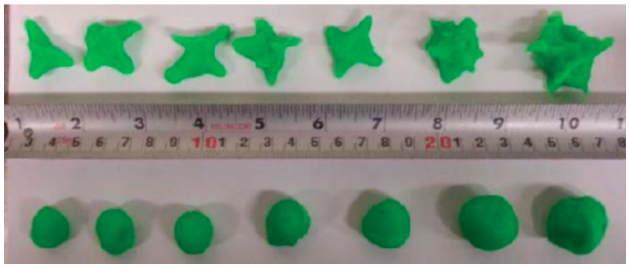

Figure 2.13: Tumor phantoms.

During the experimental acquisitions, a monostatic radar system was considered, thus the VNA worked as both microwave waveform generator and receiver for the reflected waves. The frequency was swept from 1 to 6 GHz for each tumor model

and at 144 different angular positions. The results of benign and malignant tumor classification was performed through a further post-processing of the acquired data, based on the Radar Target Signature (RTS) of the tumors. The results are in good agreement with simulations.

Chapter 3

Reconstruction Algorithm

Microwave imaging is a technique aimed at investigate a given domain by means of microwaves and reconstruct the scattering scenario, starting from the equations that govern electromagnetic scattering phenomena. Several approaches can be applied to localize, shape and reconstruct an unknowkn target located in the area of interest, surrounded by an arbitrary number of measurement probes able to acquire the samples of the scattered field. Those considered in this thesis are inverse scattering procedures. Inverse scattering is an *ill-posed* problem (i.e., small variations in the measured data can lead to large errors in the reconstructions), whose solution is achieved through Time-Reversal Imaging (TR). The scatterer is localized by MUltiple SIgnal Classification algorithm (MUSIC)[31]. This method, called TR-MUSIC, has been developed by Devaney [39, 44, 45].

In this work a Multi-frequency approach is exploited. Data collected at different frequencies through a Vector Network Analyzer are employed to overtake limits of the single-frequency case and combined in MUSIC-like methods.

In order to obtain an image of the domain under test, it is conventient to accomplish a pre-processing analysis of the measured data that consists in:

- Clutter mitigation: the reflections due to the skin layer and internal antenna reverberations produce raw data in which clutter is different orders of magnitude greater than the signal corresponding to the scatterers. In order to clean the data from these useless contributions the low frequency content is filtered out (i.e., the average component is subtracted from the data)
- Preliminary assessment of scattering scenario: in this step, mean value for Debye parameters are estimated to reduce blurring in the detection procedure
- Reconstruction algorithm (§3.3)

· Evaluation of the reconstruction through the study of spatial and contrast features (§3.4)

3.1 Basic Ideas in Direct and Inverse Scattering

Scattering theory, in the time dependent formulation, is the study of the long time behaviour of solutions of an evolution equation that move out to infinity. The evolution equation might be the time dependent Schrödinger equation (quantum scattering), the scalar wave equation (acoustical scattering), Maxwell's equations (electromagnetic scattering) or even a non-linear evolution equation. The underlying space might be Euclidean space or a Riemannian manifold. In each problem there is a localized scattering target. Moving in space away from the target to infinity, the equations, or the geometry, become simpler. The idea is that in the distant past and in the far future, the scattered wave will be located in the region where the equation or geometry is simple. It then becomes possible to compare distant past input to the far future output. Inverse scattering is how we obtain a large part of our information about the world. Form a physical point of view, it is generally recognized that the differences between direct and inverse problems are related to the concepts of cause and effect. By the way, it is arbitrary to define whether a problem is the direct or inverse part respect to its counterpart, since one generally calls two problems inverse to each other if the formulation of one problem involves the other one, and the direct problem is usually referred to the simpler one or the one which was studied earlier [32].

The inverse scattering problem considered here belongs to the category of inverse problems. An everyday example is human vision: from the measurements of scattered light that reaches our retinas, our brains construct a detailed three-dimensional map of the world around us. Our knowledge about interior structure of the Earth is given by the solution of the inverse problem of determining the sound speed by measuring travel times of seismic waves. Many other cases exist in different areas of nature (the way dolphins construct a detailed three-dimensional map of the world around them, etc.), science (the investigation of the DNA structure solving X-ray diffraction problems, etc.) and industry (non-destructive evaluation of materials to find cracks and corrosions, oil exploration, etc.). Medical imaging uses scattering of X-rays, ultrasound waves and electromagnetic waves to make images of the human body which is of invaluable help with medical diagnosis.

In a *well-posed* problem, one wants to find $x \in X$ given $y \in Y$, such that

$$Kx = y$$

where K is an operator mapping elements of the normed space X into elements of the normed space Y. The problem turns out to be *well posed* if the operator K is bijective and the inverse operator K^{-1} is continuous, so that the solution depends continuously on the data and the stability is guaranteed.

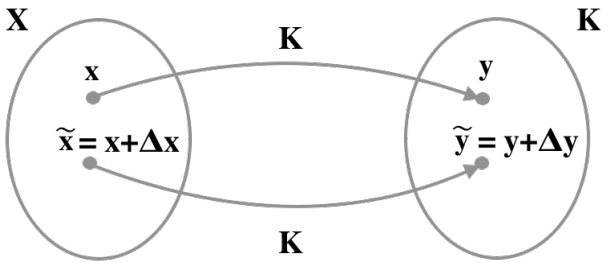

Figure 3.1: If a problem is ill-posed, small variations on the data ($\triangle x$) produce big variations on the solution ($\triangle y$), such that $|\triangle x| \leq c|\triangle y|$, $c \gg 1$.

The most critical aspect of an inverse problem is usually its ill-posedness. According to Hadamard's definition, a problem is well posed if its solution exists, depends continuosly on the data and is unique, so that a small perturbation of tha data results in a small perturbation of the solution. If one of the previous condition is not satified, the problem is called *ill-posed* or *improperly-posed* (Figure 3.1). In orer to make the solution of ill-posed problems more stable, *regularization methods* may be applied. Theis aim is to find a tradeoff between accuracy and stability of the solution exploiting additional *a-priori* information which reduces the instability of the solution at the price of finding an approximate version of it [18].

In imaging applications, we obtain information on the object subjected to the incident radiation starting from the measurements of the scattered field, and the ill posedness may lead to different scenarios. If two or more different objects produce the same measured data, the solution of the problem is not unique. Moreover, if two significantly different objects produces very similar set of measurements, the problem solution does not dipend continuosly on the data, since small measurement errors result in large errors in the solution. The information exploited to obtain a more stable solution regards the knowledge of some physical features of the target to be detected or the noise level of measured data.

To sum up, the goal of direct scattering theory is to determine the relation be-

tween the input and output waves, given the details about the physical laws and the scattering target. On the other hand, the aim of inverse scattering theory is to determine properties of the target from future observations through the calculation of the evolution of the system backwards in time, given sufficiently many input-output pairs. In fact, most often scattering problems are stated in a time independent formulation that results after taking a Fourier transform in the time variable. Although the immediate connection to the original scattering experiments is obscured, it can be easier to state and study scattering problems in this formulation.

3.2 Inverse Scattering Problem

3.2.1 Linear Inverse Scattering

The imaging problem for point targets can be roughly defined to be that of forming an "image" of the distribution of target scattering centers from measurements of the fields generated in a suite of N scattering experiments that employ the set of incident fields ψ^{inc}. The goal of inverse scattering problem is the *quantitative* determination of both the target positions and the target scattering strengths τ_m, $m = 1, \ldots, M$, from the available scattered field data. It is assumed that one knows the background Green function $G_0(\boldsymbol{r}, \boldsymbol{r'})$ of the medium in which the targets are embedded. The background medium can also be heterogeneous with possible sharp boundaries and reflecting surfaces. The inverse scattering problem consists in deducing the target positions and scattering strengths from knowledge of the full Green function specified at all transmitter/receiver pairs as well as of the background Green function at all pairs of points $(\boldsymbol{r}, \boldsymbol{r'})$ within the background medium [33]. This semplified model is able to produce only qualitative informations, thus a further classification step is generally needed. From a pratical point of view, problems of reliability and computational burden are avoided.

In the last two decades, different linear inversion techniques have been developed and applied in breast cancer detection field.

The classical time-domain techniques to solve linear inversion problems belong to beamforming methods framework, in which different approaches have been developed. The simplest algorithm of this family, called Delay And Sum (DAS), provides the reconstructed image as a sum of the contribution obtained by delaying the registered time-domain signals knowing the wave propagation speed in the space domain. Different improvements of this method was carried out, such as Delay Multiply And

Sum (DMAS), Improved Delay And Sum (IDAS). O'Halloran *et al.* [34] proved that both the IDAS and DMAS significantly outperform the DAS beamformer where the breast is mainly composed of adiposetissue and is primarily dielectrically homogeneous. However, in the more dense model, where fibroglandular tissue contributes to a significant mismatch between the assumed and actual channel propagation models, the improved performance promised by both IDAS [35] and DMAS is significantly reduced. Other approaches belonging to the beamforming family are the Microwave Imaging via Space-Time (MIST [36]) and Confocal Microwave Imaging (CMI [16]) beamforming techiques.

In addition to these methods, a Time-Reversal (TR) methods are based on the time reversibility of the wave equation in a stationary and lossless medium [37][40]. In TR imaging one or more unknown scatterers are sequentially probled using a set of N antennas and the backscattered returns are measured at all the antenna locations and involves physical or synthetic retransmission of signals acquired by a set of transceivers in a time-reversed fashion, i.e. last-in first-out. The retransmitted signals propagate "backwards", naturally reversing the path that they underwent during forward propagation, which results in (automatic) energy focusing around initial source location (Figure 3.2). The "source" in this case can be either active or passive.[38].

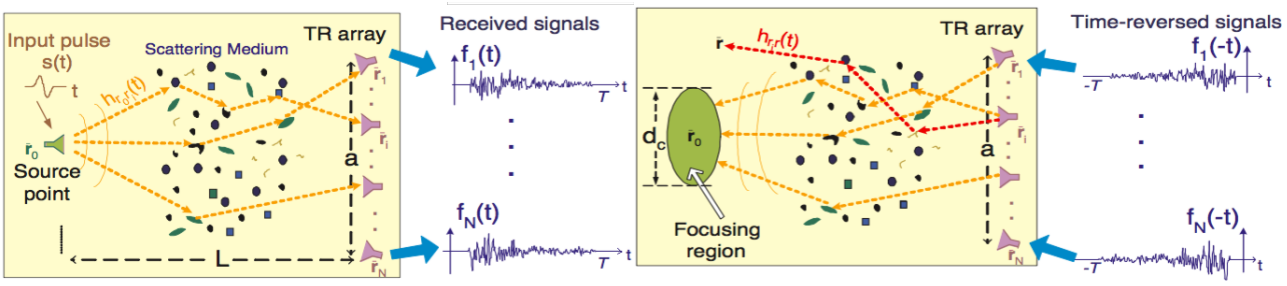

Figure 3.2: A point source located at $\bar{r}$ transmits a short Ultra Wide Band pulse s(t). (left) The transmitted signal propagates through the medium and is received by an antenna array (forward propagation). (right) The signals received at each array element are recorded, reversed in time, and transmitted back to the same medium.

The TR techniques that rely on ultrawideband (UWB) operation are further attractive because they can exploit advantages of simultaneous operation at low (e.g., more penetration into lossy materials) and high frequencies (e.g., better resolution), and because they enable imaging techniques in random media that depend only on the statistical properties (instead of a particular realization) of the random media,

i.e., they are statistically stable. Also, they allow to achieve superresolution, meaning that the resulting resolution beats the classical diffraction limit[38]. The most significant development of TR algorithm are Decomposition of the TR Operator (DORT) and TR MUltiple Signal Classification (TR-MUSIC).

3.2.2 Non-Linear Inverse Scattering

The inverse problem is formalized by finding the unknown contrast distribution of the object from the measured scattered field at the receivers, for a known incident field, such as the dielectric and conductivity maps of the breast.

The non-linear inverse scattering problem may be solved by an iterative optimization process, where the difference between the measured field and the computed field from the direct problem is minimized. When the error is sufficient small the reconstructed image of the object is the complex permittivity map used in the direct problem. In these algorithms, the distribution of the constitutive parameters in the imaging domain is updated by steps. In each iteration, the scattered field from the current parameter distribution is calculated and compared with the measured field. This optimization process may be arranged in a Least Square formulation called Newton-Kantorovich [41], Levenberg-Marquardt [42] or Gauss-Newton algorithm [43]. These techniques require that the scattered field is calculated in each iteration using a forward solver, such as Finite Difference Time Domain (FDTD), Finite Element Method (FEM) or Method of Moments (MoM).

Forward solvers are heavy from a computational point of view. For this reason non-linear imaging algorithms are less applied than linear algorithm.

3.3 Time Reversal and MUSIC

3.3.1 The general approach

We consider an array of N antennas centered at the space point $\boldsymbol{R_j}$, $j = 1, 2, ..., N$ not necessarily regularly spaced or belonging to a plane. Each antenna is assumed to radiate a scalar field $\psi_j(\boldsymbol{r}, \omega)$ in a domain D in wich are embedded one or more targets. The antennas and the targets are respectively assumed to be monopoles (point antennas) and ideal point scatterers. Also, all multiple scattering between targets are neglected.

Under these simplifying assumptions, the wavefield radiated by the j-th antenna element and the resulting scattered field are equal to

$$\psi_j^{inc}(\boldsymbol{r},\omega) = G(\boldsymbol{r},\boldsymbol{R}_j,\omega)e_j(\omega) \tag{3.1}$$

$$\psi_j^{sc}(\boldsymbol{r},\omega) = \sum_{m=1}^{M} G(\boldsymbol{r},\boldsymbol{X}_m,\omega)\tau_{mj}(\omega)G(\boldsymbol{X}_m,\boldsymbol{R}_j,\omega)e_j(\omega) \tag{3.2}$$

where M is the number of the targets, ω is the frequency, $\tau_m(\omega)$ is the scattering amplitude, $\boldsymbol{X_m}$ is the location of the m-th target, $\tau_m(\omega)$ is the input voltage applied at the terminals of the j-th antenna element, e_j is the j-th antenna excitation voltage and $G(\boldsymbol{r},\boldsymbol{r}')$ is the Green's function of the background medium.

When all antenna elements are simultaneously excited using the voltages $e_j(\omega)$ the total incident scattered wavefields are given respectively by

$$\psi^{inc}(\boldsymbol{r},\omega) = \sum_{j=1}^{N} \psi_j^{inc}(\omega) = \sum_{j=1}^{N} G(\boldsymbol{r},\boldsymbol{R}_j,\omega)e_j(\omega) \tag{3.3}$$

$$\psi^{sc}(\boldsymbol{r},\omega) = \sum_{j=1}^{N} \psi_j^{sc}(\omega) = \sum_{j=1}^{N}\sum_{m=1}^{M} G(\boldsymbol{r},\boldsymbol{X}_m,\omega)\tau_{mj}(\omega)G(\boldsymbol{X}_m,\boldsymbol{R}_j,\omega)e_j(\omega) \tag{3.4}$$

The voltage output $v_l(\omega)$ corresponding to l-th antenna is assumed to be equal to the amplitude of the scattered field as measured at the l-th antenna ans is given by

$$v_l(\omega) = \sum_{j=1}^{N} \psi_j^{sc}(\boldsymbol{R}_l,\omega) = \sum_{j=1}^{N}\sum_{m=1}^{M} G(\boldsymbol{R}_l,\boldsymbol{X}_m,\omega)\tau_m(\omega)G(\boldsymbol{X}_m,\boldsymbol{R}_j,\omega)e_j(\omega) \tag{3.5}$$

Equation 3.5 can be expressed in a compact matrix notation as follows

$$v_l(\omega) = \sum_{j=1}^{N} K_l(\omega)e_j(\omega) = \boldsymbol{K}(\omega)\boldsymbol{e}(\omega) \tag{3.6}$$

where $\boldsymbol{e}(\omega) = [e_1(\omega), e_2(\omega), ..., e_N(\omega)]^T$ is the N-dim column vector formed from the set of input voltages applied at the antenna terminals and K is named *Multistatic Response Matrix* (MSR). It represents the matrix propagator, whose (i,j) element stands for the total field received by the j-th element when i-th element is "fired", ans is defined as follows

$$\boldsymbol{K}(\omega) = \{\boldsymbol{K}_{l,j}(\omega)\} = \sum_{m=1}^{M} G(\boldsymbol{R}_l, \boldsymbol{X}_m, \omega)\tau_m(\omega)G(\boldsymbol{X}_m, \boldsymbol{R}_j, \omega) = \sum_{m=1}^{M} \tau_m(\omega)\boldsymbol{g}_m(\omega)\boldsymbol{g}_m^T(\omega) \tag{3.7}$$

and $g_m(\omega)$ is the N-dim Green function column vectors:

$$\boldsymbol{g_m}(\omega) = \{G(\boldsymbol{R}_l, \boldsymbol{X}_m, \omega)\} = [G(\boldsymbol{R}_1, \boldsymbol{X}_m, \omega), G(\boldsymbol{R}_2, \boldsymbol{X}_m, \omega), ..., G(\boldsymbol{R}_N, \boldsymbol{X}_m, \omega)]^T \tag{3.8}$$

The Green functions $G(\boldsymbol{r}, \boldsymbol{r'})$ are completely general since the above formulation applies to both homogeneous and non-homogeneous media. It is possible to define the correlation matrix, called *Time Reversal Matrix* (TRM), given by

$$\boldsymbol{T}(\omega) = \boldsymbol{K}^{\dagger}(\omega)\boldsymbol{K}(\omega) = \boldsymbol{K}^{*}(\omega)\boldsymbol{K}(\omega) \tag{3.9}$$

where $\boldsymbol{K}^{\dagger}(\omega)$ and $\boldsymbol{K}^{*}(\omega)$ are the Hermetian and the complex conjugate of $\boldsymbol{K}(\omega)$, respectively. The equality $\boldsymbol{K}^{\dagger}(\omega) = \boldsymbol{K}^{*}(\omega)$ holds because MSR is symmetric. From Equation 3.9 and Equation 3.7 we obtain the final result

$$\boldsymbol{T}(\omega) = [\sum_{m=1}^{M} \tau_m(\omega)\boldsymbol{g}_m(\omega)\boldsymbol{g}_m^T(\omega)]^*[\sum_{m=1}^{M} \tau_m(\omega)\boldsymbol{g}_m(\omega)\boldsymbol{g}_m^T(\omega)] = \sum_{m=1}^{M}\sum_{m'=1}^{M} \Lambda_{m,m'}\boldsymbol{g}_m^*(\omega)\boldsymbol{g}_{m'}^T(\omega) \tag{3.10}$$

where

$$\Lambda_{m,m'} = \tau_m^*\tau_{m'} \langle \boldsymbol{g}_m(\omega), \boldsymbol{g}_{m'}(\omega) \rangle \tag{3.11}$$

and the angular brackets stand for the standard inner product in $\mathcal{C}^N$.[39]

The TRM possesses a complete set of orthonormal eigenvectors corresponding to non-negative eigenvalues, because $\boldsymbol{T}(\omega)$ is Hermetian and non-negative. TRM eigenvectors correspond one-to-one with the different targets, and if $M \leq N$, the rank of $\boldsymbol{T}(\omega)$ will be equal to M, so that there are exactly M non-zero eigenvalues.

The goal now is to estimate the locations of the targets from the measured scatterer field data. One of the main approach emploied to reach this goal is the MUSIC algorithm , that is to be used in conjunction with time-reversal processing. We still will require multi-static data and the multi-static response matrix $\boldsymbol{K}(\omega)$ and will compute the time-reversal matrix $\boldsymbol{T}(\omega) = \boldsymbol{K}^{*}(\omega)\boldsymbol{K}(\omega)$ and the eigenvalues and

eigenvectors of this matrix. Through MUSIC algorithm it is possible to deal both with non-resolved targets as well as with sparse antenna arrays.

The MUSIC algorithm makes use of the fact that the time-reversal matrix $\boldsymbol{T}(\omega)$ is a projection operator onto the subspace of $\mathcal{C}^N$ spanned by the complex conjugates of the Green's function vectors (i.e. the signal subspace $\mathcal{S}$) and that the noise subspace $\mathcal{N}$ is spanned by the eigenvectors of $\boldsymbol{T}(\omega)$ having zero eigenvalue, where $\mathcal{C}^N = \mathcal{S} \oplus \mathcal{N}$. It follows that the complex conjugte of each Green's function vector is orthogonal to the noise subspace and, in particular, to the eigenvectors of TRM having zero eigenvalues:

$$\langle \boldsymbol{\mu}_{m0}(\omega), \boldsymbol{g}_m^*(\omega) \rangle = \langle \boldsymbol{\mu}_{m0}^*(\omega), \boldsymbol{g}_m(\omega) \rangle = 0 \tag{3.12}$$

for $m = 1, 2, ..., M$ scatterers, N antennas and $m_0 = M+1, ..., N$ eigenvectors having zero eigenvalue, where $\boldsymbol{\mu}_{m0}(\omega)$ are the eigenvectors of $\boldsymbol{T}(\omega)$ having zero eigenvalue.

Now it it possible to form a *pseudo-spectrum* through the following equation, that is the key equation of MUSIC algorithm for time-reversal imaging

$$\Phi(\boldsymbol{r}_k, \omega) = \frac{1}{\left| P\left[\boldsymbol{A}_k(\omega)\right] \right|^2} = \frac{1}{\left| \sum_{m0=M+1}^{N} \langle \boldsymbol{A}_k(\omega), \boldsymbol{\mu}_{m0}^*(\omega) \rangle \right|^2} \tag{3.13}$$

where $P[\cdot]$ is the projection operator onto $\mathcal{N}$, $\boldsymbol{\mu}_{m0}$ is the m_0-th eigenvector of $\boldsymbol{T}(\omega)$ having zero eigenvalue and

$$\boldsymbol{A}_k(\omega) = G_k(\omega) \tau_m(\omega) G_k^T(\omega) \tag{3.14}$$

is the *steering matrix*, that is the MSR matrix in the trial points $\boldsymbol{r}_k$ of domain D and $G_k(\omega) = [G(\boldsymbol{R}_1, \boldsymbol{r}_k, \omega), G(\boldsymbol{R}_2, \boldsymbol{r}_k, \omega), \ldots, G(\boldsymbol{R}_N, \boldsymbol{r}_k, \omega)]^T$. The inner product in Equation 3.13 will vanish in a deterministic way when $\boldsymbol{r}_k$ is equal to the actual location of one of the scatterers both for resolved and non-resolved targets, and this happens because the signal subspace is orthogonal to the noise subspace [39]. In other words, the pseudospectrum will show a theoretically infinite peak at each target location in a deterministic way.

The achievable performance can be equivalently and more conveniently studied by employing the projector over the signal subspace $\mathcal{S}$, uising $Q[\cdot]$ instead of $P[\cdot]$ as follows [48]

$$\left| P\left[\boldsymbol{A}_k(\omega)\right] \right|^2 = \left| (I - Q)\left[\boldsymbol{A}_k(\omega)\right] \right|^2 \tag{3.15}$$

The acquisition system considered so far is called *Multistatic configuration* (Figure 3.3). In this configuration, the acquisition system is composed of N equidistant antennas positioned around the imaging domain, along a circumference. In each measure, an antenna trasmits and receives the signal from its position ($\boldsymbol{R_i}$), whereas the other N-1 antennas receive only. This operation is performed N times, once for each antenna.

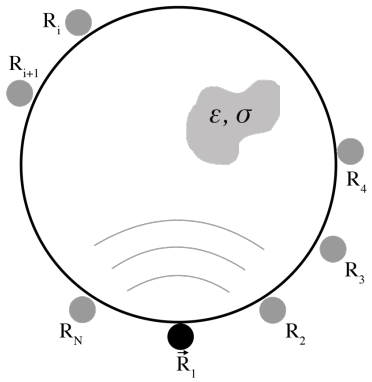

Figure 3.3: In multistatic configuration an antenna trasmits and receives the signal and the other N-1 antennas receive only.

Multistatic apporach will not be explored in this work but a short description was given because it is the general case from which we can derive the equations for the approach used in this work, called *monostatic configuration*.

3.3.2 Monostatic configuration

In *monostatic configuration*, the acquisition system is composed of only one antenna, which acts both as trasmitter and receiver. This antenna rotates around the imaging domain and stops in different equispaced positions $\boldsymbol{R}_1, \ldots, \boldsymbol{R}_N$ where the measures are performed (Figure 3.4). Once the acquisition is completed, the antenna goes back in its original position.

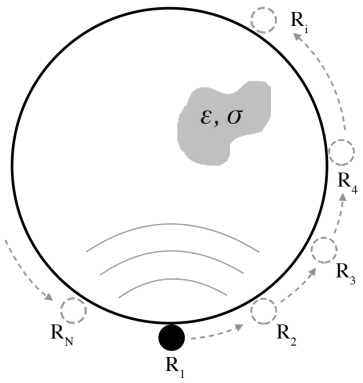

Figure 3.4: In monostatic configuration the antenna moves in different positions around the domain, from which it transmits and receives the signal from different positions.

In this system configuration, we can semplify the description given in §3.3.1 thanks to the presence of only one antenna, indeed the response matrix $\boldsymbol{K}(\omega)$ reduces to a vector because the collected signal is always associated to the same antenna that produce the excitation pulse. The vector of voltage output from N antenna positions can be defined as

$$\boldsymbol{v}(\omega) = [v_1(\omega), v_2(\omega), \ldots, v_N(\omega)] = \boldsymbol{K}(\omega)e(\omega) \tag{3.16}$$

where $v_l(\omega)$ is the voltage output from l-th antenna position derived from Equation 3.5 as follows

$$v_l(\omega) = \psi_j^{sc}(\boldsymbol{R}_l, \omega) = \sum_{m=1}^{M} G(\boldsymbol{R}_l, \boldsymbol{X}_m, (\omega))\tau_m(\omega)G(\boldsymbol{X}_m, \boldsymbol{R}_l, (\omega))e(\omega) \tag{3.17}$$

and $\boldsymbol{K}(\omega) = [K_1(\omega), K_2(\omega), \ldots, K_N(\omega)]^T$ is the *Monostatic Response vector* (MoSR).

Now we can define the *steering vector* $\boldsymbol{A}_k(\omega)$ as MoSR calculated in the trial points $\boldsymbol{r}_k$ of domain D as follows

$$\boldsymbol{A}_k(\omega) = [A_{k1}(\omega), A_{k2}(\omega), \ldots, A_{kN}(\omega)] \tag{3.18}$$

whose elements are given by Equation 3.14. The goal of the imaging procedure is to detect the scattering source by finding the steering vector, that will produce the pseudospectrum peak because it is orthogonal to the noise subspace in $\boldsymbol{r}_k$.

Now, recalling Equation 3.15, it is possible to calculate the pseudo-spectrum as follows

$$\Phi(\boldsymbol{r}_k, \omega) = \frac{1}{\left|(I - Q)\left[\boldsymbol{A}_k(\omega)\right]\right|^2} = \frac{1}{1 - \left|\langle \boldsymbol{A}_k(\omega), \boldsymbol{\mu}(\omega)\rangle\right|^2} \tag{3.19}$$

where $\boldsymbol{\mu}(\omega)$ is the single eigenvector corresponding to the theoretically strongest evigenvalue different from zero in the single scattering source hypothesis, given by the measured signal at each antenna position.

Hence, the pseudospectrum value at the corresponding trial point $\boldsymbol{r}_k$ can be calculated as

$$\Phi(\boldsymbol{r}_k, \omega) = \frac{1}{1 - \left|\cos\eta_k\right|^2} \tag{3.20}$$

where the projection of the steering vector on $\boldsymbol{\mu}(\omega)$ was performed though the n-dimensional scalar product

$$\cos\eta_k = \frac{\langle \boldsymbol{A}_k(\omega), \boldsymbol{\mu}(\omega)\rangle}{\left|\boldsymbol{A}_k(\omega)\right| \left|\boldsymbol{\mu}(\omega)\right|} \tag{3.21}$$

which enhances the correlation between test and signal vectors while forming the visual image and peaks in the proximity of the scatterer position[46]. It can assume values in the range [0,1] and its square modulus, called *correlation term*, represents the probability that the measured signal vector $\boldsymbol{\mu}(\omega)$ is actually given by a single scattering process occurring in $\boldsymbol{r}_k$.

3.3.3 Background Green's Functions

In order to describe scattering problems, it is necessary to deduce equations relating the measured values of the electromagnetic field to the properties of the scatterer under test.

We consider the mathematical model in which wave propagation is governed in a inhomogeneous medium by the Helmholtz equation:

$$(\nabla^2 + k^2)\psi(\mathbf{r}) = f(\mathbf{r}) \tag{3.22}$$

where $f : \mathbb{R}^n \to \mathbb{C}$ is a given function with compact support and $k = {}^{\omega}/_{c}$ is the wavenumber. The Helmholtz equation describes the radiation of waves in a dispersive medium characterized by an index of refraction $n(\omega)$ and wavenumber $k(\omega) = n(\omega) \cdot \omega/c$. We thus take the Helmholtz equation to be the fundamental equation governing radiation and wave propagation in a dispersive medium characterized by a complex background wavenumber $k(\omega)$. This equation can be expressed in terms of radiation

integral as:

$$\psi(\boldsymbol{r}) = \int_{\mathbb{R}^n} f(\boldsymbol{R}) G(\boldsymbol{r}, \boldsymbol{R}) d\boldsymbol{R}$$

where $\boldsymbol{R}$ is the observation point, $f(\boldsymbol{R}) = \tau(\boldsymbol{R})\psi(\boldsymbol{R})$ and $\tau(\boldsymbol{R})$ represents the scattering amplitude. $G(\boldsymbol{r}, \boldsymbol{R})$ is the free-space Green's function of the medium in which the targets are embedded (background medium) , and depends on the dimension of the space. For a two-dimensional space, where the antennas and the targets can be considered as point like sources in R^2, it is given by

$$G_{2D}(\boldsymbol{r}, \boldsymbol{R}, \omega) = -\frac{j}{4} H_0^{(2)}(k|\boldsymbol{r} - \boldsymbol{R}|) \tag{3.23}$$

where $|\cdot|$ represents Euclidean distance, $H_0^{(2)}$ is the Hankel function of 0-th order and 2-nd kind.

The background Green's function can be calculated also for the 3-dimensional case, according to the relationship between the incident field and the source current, that is characteristic of the antenna in use. If we consider a z-polarized ideal dipole-antenna of lengh l characterized by a z-directed source current I_0, the corresponding Dyadic Green's function (DGF) can be calculated as

$$\overleftrightarrow{G_b} = \frac{1}{k\eta I_0 l} \begin{bmatrix} 0 & 0 & 0 \\ 0 & 0 & 0 \\ E_x(\boldsymbol{r}, \omega) & E_y(\boldsymbol{r}, \omega) & E_z(\boldsymbol{r}, \omega) \end{bmatrix} \tag{3.24}$$

where η is the wave impedence and k is the wave number. The first two rows of the tensor are equal to zero since no x-directed or y-directed sources are used. When the scalar field approximation is used, cross polarization scattering effects are assumed to be negligible, hence E_x and E_y are set to zero and the tensor reduces to a single element [47]. From this simplify assumption, the Green's function propagator reduces as

$$G_{3D}(\boldsymbol{r}, \boldsymbol{R}, \omega) = \frac{E_z(\boldsymbol{r}, \omega)}{k\eta I_0 l} \tag{3.25}$$

Also, $E_z(\boldsymbol{r}, \omega)$ has been computed evaluating the z-axis projection of the field components E_θ, E_r associated to the Hertzian dipole (Appendix A) total electric field:

$$E_z(\boldsymbol{r}, \omega) = E_\theta(\boldsymbol{r}, \omega)\sin\theta + E_r(\boldsymbol{r}, \omega)\cos\theta \tag{3.26}$$

In radiation scattering, we exploit the far field approximation, so that E_r vanishes and we obtain

$$G_{3D}(\boldsymbol{r}, \boldsymbol{R}, \omega) \simeq \frac{E_\theta(\boldsymbol{r}, \omega)\sin\theta}{k\eta I_0 l} = iG_0(\boldsymbol{r}, \boldsymbol{R})\sin^2\theta \tag{3.27}$$

where is the three-dimensional Green's function in free space.

3.3.4 Multi-frequency analysis

A single-frequency approach suffers from two main limitations. First, when data are undersampled, many source's replica corrupt the pseudospectrum and, consequently, actual sources result indiscernible. As a consequence, artefacts may rise and prevent the scatterer detection. Secondly, due to the rank deficiency of $\boldsymbol{T}(\omega)$, when multiple sources populate the scene, achievable performance quickly degrades.

Data collected at different frequencies can be employed to improve the performance of the single-frequency reconstruction. A simple way to achieve this goal is combine incoherently different pseudospectra obtained at each frequency. Different methods can be exploited to perform the recombination procedure, starting from the single frequency imagedefined by means of the single frequency pseudospectrum obtained at freqeuncy ω_i as it follows

$$P_i = P(\omega_i) = \frac{1}{1 - \|cos\eta_i\|^2} \tag{3.28}$$

Ruvio *et al.* [48] propose two MUSIC-like methods to combine different pseudospectra corresponding to N_ν frequencies:

Wide-band Music algorithm (WB-MUSIC):

$$\Phi_{WB}(\boldsymbol{r}_k) = \frac{1}{\sum_{i=1}^{N_\nu} \left|P_i\left[\boldsymbol{A}_k(\omega_i)\right]\right|^2} \tag{3.29}$$

Interferometric MUSIC algorithm (I-MUSIC):

$$\Phi_I(\boldsymbol{r}_k) = \frac{1}{\prod_{i=1}^{N_\nu} \left|P_i\left[\boldsymbol{A}_k(\omega_i)\right]\right|^2} \tag{3.30}$$

In [48] it was shown that I-MUSIC enables a clearer and higher dynamic range reconstruction by retaining resolution due to the highest frequencies. Also, the effects of mismatch between the permittivity of the background and host medium appeared as a delocalization error in the radial direction.

Also, we exploited another recombination algorithm defined as follows:

Interferometric Logarithmic MUSIC algorithm (ILOG-MUSIC):

$$\Phi_{ILOG}(\boldsymbol{r}_k) = \frac{1}{\left| log\left(\prod_{i=1}^{N_\nu} \|cos\eta_i\|\right)\right|} \tag{3.31}$$

Through these multi-frequencies algorithm we expect to reduce the presence of artefacts and obtain a more reliable image. Also, ILOG-MUSIC should strongly enhance the contrast in respect of the clutter surrounding the signal.

3.4 Metrics

In this thesis a large number of measurements and image reconstruction were performed. The aim of this massive work was to characterize the performances of the automatic acquisition system (§4.1) developed in the last few months. In order to reach this goal it was necessary to have some numerical references able to represent a certain feature of the reconstructed image, both from spatial and contrast point of view.

MUSIC algorithm locates the scatterer in corrispondence of the maximum in the pseudospectrum. From a theoretical point of view, the source is represented by a point source, whose mathematical description is a Dirac delta function of infinite value. In real cases, as always with real optical systems, the resulting image shows a spread curve with a finite non-symmetric maximum. Also, in particular cases the presence of strong artefact was faced (Figure 3.5). To study these intrinsic behaviours as a function of the frequency and of the contrast, Full Width at Half Maximum (FWHM) and Signal-to-clutter Mean Ratio (SMR) were computed.

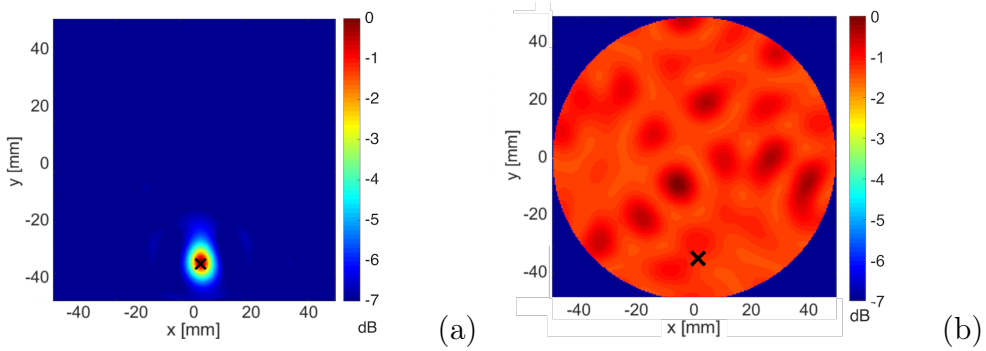

Figure 3.5: Comparison between a good single-frequency reconstruction of the tumor position (a) and a recostruction strongly affected by clutter and artefacts (b). In this second case, the maximum of the pseudospectrum is very delocalized.

Full Width at Half Maximum

Full Width at Half Maximum is a parameter commonly used to describe the width of a curve. It is given by the distance between points on the curve at which the function reaches half of its maximum value. Since we have a 2D problem, we need to identify the two directions along which the variance is maximized. The computation of these two directions is performed by the Principal Component Analysis (PCA), that is a statistical procedure that uses an orthogonal transformation to convert a set of observations of possibly correlated variables into a set of values of linearly uncorrelated variables called principal components. This transformation is defined in such a way that the first principal component has the largest possible variance (that is, accounts for as much of the variability in the data as possible), and each succeeding component in turn has the highest variance possible under the constraint that it is orthogonal to the preceding components [49]. This trasformation brings the data to a new polar coordinate system (ρ, ϕ).

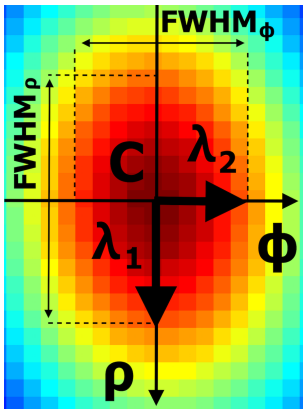

Figure 3.6: Centroid C and $FWHM_{\rho,\phi}$ along the directions obtained from PCA.

The FWHM along these two directions is defined as:

$$FWHM_{\rho,\phi} = 2\alpha\sqrt{\lambda_{1,2}} \tag{3.32}$$

where $\lambda_{1,2}$ are the eigenvectors of the covariance matrix of the data computed thought PCA and $\alpha = 1,96$ represents the 95% confidence interval. Through FWHM we can estimate the target position as the centroid of the curve at half maximum (Figure 3.6).

Signal-to-Clutter Mean Ratio

Clutter is an important phenomenon for the evaluation of the recostruction process perform. When the contrast is high, clutter tends to be very low in comparison to the target signal, whereas its relative importance gets higher the lower the contrast is. In addition to this, we may bump into situations where for some reasons the clutter is higher than the signal. It is necessary to have a measure of the useful part of the signal produced by the target in respect to the background spread signal. In order to separate the *signal area* from the *clutter area* we define two concentric ellipses whose axes length a_ϕ , a_ϕ verify the following conditions:

$$a_{\rho,\phi} \leq 3 \cdot \sigma_{\rho,\phi} \tag{3.33}$$

$$3 \cdot \sigma_{\rho,\phi} \leq a_{\rho,\phi} \leq 6 \cdot \sigma_{\rho,\phi} \tag{3.34}$$

where $\sigma_{\rho,\phi}$ is the standard deviation defined as

$$\sigma_{\rho,\phi} = \frac{FWHM_{\rho,\phi}}{2\sqrt{2ln(2)}} \tag{3.35}$$

We define Signal-to-clutter Mean Ratio as:

$$SMR = \frac{\frac{1}{N_S}\sum_{\boldsymbol{r}_i \in signal} \phi(\boldsymbol{r}_i)}{\frac{1}{N_C}\sum_{\boldsymbol{r}_i \in clutter} \phi(\boldsymbol{r}_i)} \tag{3.36}$$

where ϕ is the signal value, N_S and N_C are the number of points in Signal and Clutter areas, respectively (Figure 3.7).

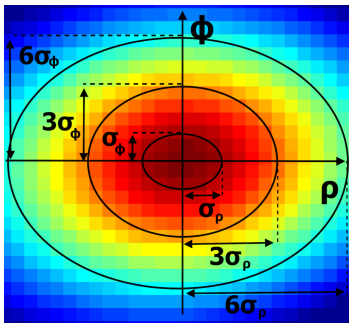

Figure 3.7: Ellipses centered on the Centroid C in the PCA coordinate system. The "signal area" is defined as the area included between $3\sigma_{\rho,\phi}$, whereas the elliptical corona from $3\sigma_{\rho,\phi}$ to $6\sigma_{\rho,\phi}$ corresponds to the "clutter area" .

Chapter 4

Experimental Setup

This chapter introduces a brief description of the instruments used to carry out the measurements. The first two sections are about the phantoms and the hardware components used to set up the acquisition system. The third section is focused on the development of a LabView software which aims to automatically acquire data through a monostatic approach. Concluding, it is presented a LabView algorithm set up to manage 12 antennas in a multistatic approach.

4.1 Breast and Tumor Phantoms

The breast phantom, called ACHILLE, is the second phantom prototype built at the University of Bologna (Figure 4.1a). The measuring system is composed by the dipole antenna ANT-24G-905-SMA developed by RF Solutions, the CR1- M-Z6 Motorized Continuous Rotation Stage driven by OptoDCDriver ODC001 motor developed by ThorLabs and the Copper Mountain - S5048 Vector Network Analyzer. The LabView software specifically developed for this work is able to drive the motor and perform automatic data acquisition.

The breast phantom consists of four main elements: the breast, the skin layer, the fibroglandular tissue and the tumor. The breast is a PVC cylindrical plastic tube, characterized by a radius r_b = 55mm and height h_b = 500mm. It is filled with seed oil, whose relative permittivity is ε_b=2.5, that simulates the breast adipose tissue. For the second set of measurements, performed with heterogeneous medium, a 25mm radius cylinder was inserted, fixed on the wall of the bigger cylinder (Figure 4.1b) and filled with solutions to simulat different fibroglandular tissuese. The bigger cylinder is connected to the motor by a belt and rotated around the vertical axis. This phantom is supported by an upper wood structure and by a fixed circular guide at the bottom.

On the upper wood structure a ball bearing is inserted in order to reduce the friction during the rotation. The wall of the cylinder represents a skin layer with thickness t_s = 2mm and relative dielectric constants $\varepsilon_{PVC} \approx 3.2$. If necessary, this cylinder would be upholstered with a specific film to simulate skin dielectric properties in a more accurate way. The tumor is simulated by small PVC tubes of different diameter and filled with different chemical solutions. The tubes employed in this work have a radius (r) equals to 5, 10 or 16mm and height h=500mm, which can be used in infinite cylinder approximation, since their diameter is much smaller than the heigth. Also, two finite-dimension scatterer was developed to perform 3D reconstructions in the last set of measurements. The chemical solutions are developed to study the features of the reconstructed images as a function of ε, starting from $\varepsilon \approx 3$ to $\varepsilon \approx 81$. Fianlly, the breast phantom phantom is embedded in a coupling medium with $\varepsilon_d = \varepsilon_b$.


(a)
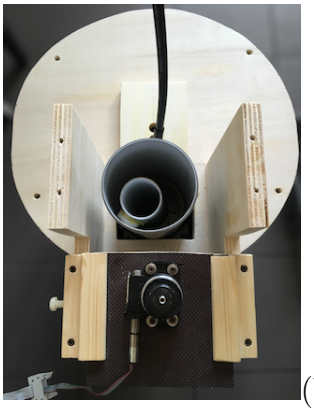
(b)
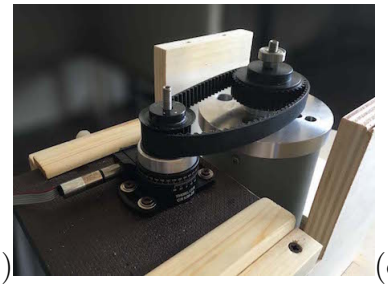
(c)

(d)

(e)
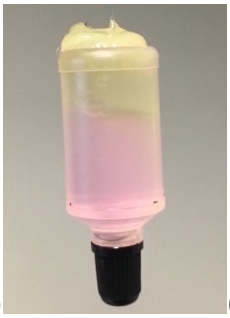
(f)

Figure 4.1: (a) LabView software drives the motor and VNA, which perform measurements on ACHILLE. (b) The brest phantom with the motor and the coaxial cable. The bigger cylinder stands for the skin layer. Inside of it, the tumor phantom is inserted. The smaller cylinder is used to reproduce fibroglandular tissue in the second data acquisition, whereas during the characterization stage only the big cylinder is used to simulate the breast. (c) The motor connected to the breast phantom through a belt. The trasmission gear is 1:2, so that a complete rotation of the breast phantom corresponds to a 720° rotation of the motor. (d) Three different tumor phantoms of 16, 10 and 5mm diameter developed to exploit the infinite cylinder approximation. (e), (f) Finite dimension targets which can be considered as sphere of 1.6cm diameters and characterized by (e) $\varepsilon \simeq 4.5$ and (f) $\varepsilon \simeq 47$.

Breast tissues are characterized by a large percentage of fat. In particular, normal tissue has a low dielectric permittivity, whereas fibroglandular and malignant tissues are characterized by an higher dielectric constants. One of the main issues of microwave imaging is that the tumor is often into the fibroglandular area, so that its contrast on the dielectric parameters is low. Our goal is to study the ability of the acquisition system developed during this work to find a low contrast object into both an homogeneous and heterogeneous medium. Therefore, tumor phantoms of different dimensions and dielectric properties were required.

A breast phantom was manufactured in order to reproduce a scatterer with stable electromagnetic properties using different percentages of oil, acetone, alcool, glycer

and water. Indeed, breast phantoms based on oil emulsions can reproduce the electric properties of various normal and malignant breast tissues. We were inspired by *Ruvio et al.* [51] , whose breast phantoms was composed of a properly mixing of kerosene and safflower oil solution with a formaldehyde-based emulsion. Their phantom was also mechanically stable, i.e. they created a solid gelatine of the different mixtures, whereas we emploied liquid emulsions and solutions to fill the scatterers.

In this work, different chemical solutions (Figure 4.2) were investigated and realized to study the performance of ACHILLE on varying the relative permittivity of the tumor phantom (Table 4.1)), that is correlated with the scattering efficiency. For this purpose, varius emulsions[1] of seed oil ($\varepsilon = 2,5$) with acetone ($\varepsilon = 21$), and solutions of water ($\varepsilon = 81$) and alcool ($\varepsilon = 24$) were created. Moreover, some samples made of glycerol ($\varepsilon = 51$) and water were used aswell.

We tried many different approaches to realize stable emulsions, since we needed to use oil to produce targets characterized by low dielectric constant. At the beginning we tried to emulsify seed oil with water and seed oil with alcool through lecithin, that is a natural emulsionant derived from soy. We noticed that the emulsions were stable only for a short while (approximatively from 1 to 20 minutes) according to the different percentages of the two components, so they were not good candidates for our study since our measurements last about 15 minutes. Therefore, we tried to emulsify other substances exploiting also liquid lecithin, that is lecithin previously dissolved in oil to improve its emulsifying properties. After many other attempts we realized completely stable emulsions of seed oil and acetone in different percentages in order to sample the behaviour of our experimental system at low values of ε.

The evaluation of the relative permittivity constant of the solutions containing the volume V_A of element A and V_B of the element B was done using the followng formula (Equation 4.1)

$$\varepsilon = \frac{V_A \cdot \varepsilon_A + V_B \cdot \varepsilon_B}{V_A + V_B} \tag{4.1}$$

whose error was estimated by Equation 4.2:

$$\frac{\triangle \varepsilon}{\varepsilon} = \frac{\triangle V_A \cdot \varepsilon_A + \triangle V_B \cdot \varepsilon_B}{V_A \cdot \varepsilon_A + V_B \cdot \varepsilon_B} + \frac{\triangle V_A + \triangle V_B}{V_A + V_B} \tag{4.2}$$

[1] In order to stabilize the emulsions, a negligibile part of lecithin was added.

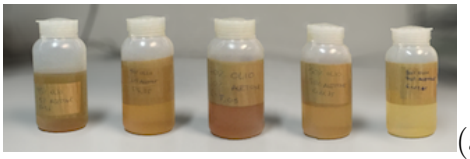
(a)

(b)
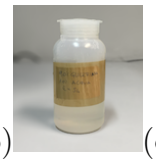
(c)

Figure 4.2: (a) Emulsions of oil and acetone, the brownish colour is given by lecithin; (b) Solutions of alcool and water; (c) Solution of glycerol and water.

Seed Oil (%)	Acetone (%)	ε	$\triangle\varepsilon$
100	0	2.5	0
95	5	3.4	0.4
90	10	4.4	0.6
70	30	8.1	0.8
50	50	11.8	0.9
30	70	15	1
0	100	21	0

Alcool (%)	Water (%)	ε	$\triangle\varepsilon$
100	0	24	0
80	20	35	4
60	40	47	4
40	60	58	4
20	80	70	5
0	100	81	0

Glycerol (%)	Water (%)	ε	$\triangle\varepsilon$
90	10	54	5

Table 4.1: Percentual proportions in volume and relative permittivity of the salmple solutions used to fill the target. The relative permittivity of pure elements were taken from literature and considered without errors.

Finally, we developed two finite dimension tumor phantom to test the acquisition system with a 3D reconstruction algorithm in both homogeneous and heterogeneous medium. In the homogeneous experiment, we have used GLASSBURGER (Figure 4.1e), that was realized gluing two hemispherical glass stones. The dielectric property of this phantom is assumed to be equal to the relative permittivity of glass ($\varepsilon_{glass} = 5$). Also, we have developed a scatterer with higher dielectric permittivity to perform measurements in heterogeneous medium. In this experiment, we employied PATROCLO, that is a plastic bottle of cylindrical shape of height $h_P = 30$mm and radius $r_P = 8$mm. In order to approximate the form of this scatterer with a 16mm diameter sphere, we filled this scatterer with a proper volume of the solution characterized by $\varepsilon = 47$, and the remaining volume was filled with seed oil. Those two

scatterers were individually glued with a nylon string, that was necessary to fix the correct depths.

4.1.1 Existing Phantom

The first phantom developed at University of Bologna, called ARCHIMEDE (Figure 4.3), was a simpler prototype but it had a similar structure. Indeed, on the upper wood structure there was a goniometric indicator used to read the angle of rotation, since the phantom motion and data acquisition were performed manually. Also, measurements were carried using only a scatterer filled with water characterized by ε=81. It was used to perform preliminary measurements to test the reconstruction algorithm on real data.

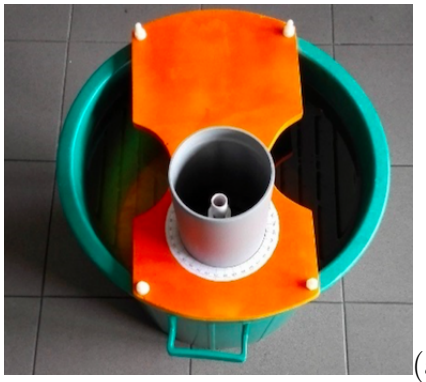
(a)

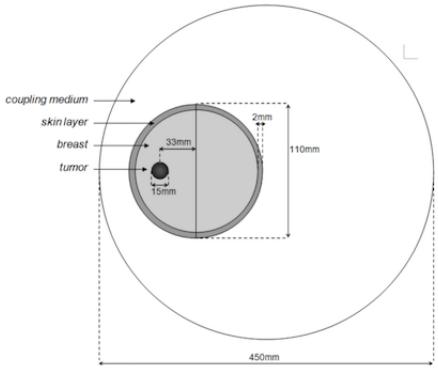

(b)

Figure 4.3: (a)The breast phantom ARCHIMEDE and (b) its geometry.

4.2 Hardware

4.2.1 Dipole Antenna

The antenna used is an half-wave sleeve dipole antenna and it is fixed on the upper wood support of the breast phantom and it can be located at three different distances from the breast.

An half-wave dipole antenna consists of two quarter-wavelength conductors placed end to end for a total length of approximately $L = \lambda/2$ (Figure 4.4). A "sleeve" antenna is a vertical dipole with the feed (transmission line) entering from one end of a hollow element. This design allows to easily insert the antenna on our phantom because the coaxial cable enters inside the antenna in the parallel direction of its axis, and not orthogonally as it happens with other antennas.

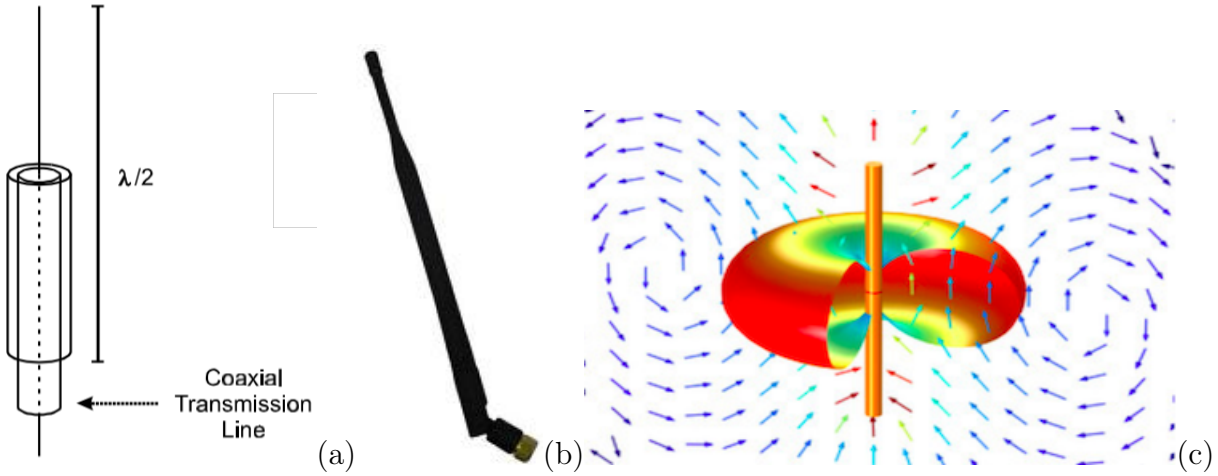

Figure 4.4: (a) Design of sleeve antenna; (b) ANT-24G-905-SMA Dipole antenna used to produce the the electromagnetic field and its radiation pattern (c) (Barcolor: from red color, high value in dB, to blue, low values).

The current distribution is that of a standing wave, approximately sinusoidal along the length of the dipole, with a node at each end and an antinode (peak current) at the center (feedpoint):

$$I(z) = I_0 e^{jwt} cos(kz)$$

where $-L/2 \leq z \leq L/2$, $w = 2\pi f$ is the radiant frequency, $k = 2\pi\lambda$ is the wavenumber and j is the imaginary unit.

In the far field, this produces a radiation pattern whose electric field is given by

$$E_\theta = \frac{-jZ_0 I_0}{2\pi r} \cdot \frac{cos(\frac{\pi}{2}cos(\theta))}{sin(\theta)} \cdot e^{j(wt-kr)}$$

where $Z_0 = (c\varepsilon_0)^{-1}$ is the free-space impedance and the feedpoint current is assumed to be $I_0 e^{jut}$. The term $cos[(\pi/2)cos(\theta)]/sin(\theta)$ is called directional factor [50].

Figure 4.4c shows the radiation pattern of such kind of antenna.

ANT-24G-905-SMA Dipole antenna

The dipole antenna used is the ANT-24G-905-SMA antenna (Figure 4.4b) developed by RF Solutions. It is an omni-directional gain antenna, its specifications are:

· Frequency Group: 2.4 - 2.5 GHz

· Active gain: +5dB

· Vertical Polarization

· Internal/External usage

· Adjustable 90deg SMA Connector.

4.2.2 Vector Network Analyzer

In its simplest form, a network analyzer is an instrument used to measure impedance. At low frequencies, you can measure impedance with relatively simple tools, including a sine wave generator, a volt meter, a current meter, and a calculator. Using these tools, you can measure the ratio between voltage and current and calculate the resulting impedance. At RF and microwave frequencies, measurements of voltage and current become more complex. As a result, a VNA uses a more complex design to measure incident and reflected waves (Figure 4.5). In many ways, the VNA marries the principles of the basic impedance measurement with hardware appropriate for microwave frequencies. When using a VNA to measure the impedance or the reflection factor, a sine generator stimulates the device under test (DUT). In addition, two receivers take the place of the combination of a volt meter and current meter. These receivers, with the help of signal separation hardware, characterize the response of the device by measuring the phase and amplitude of signals that are both incident to and reflected from the DUT. Finally, calibration capabilities are required to eliminate systematic errors and compute the appropriate ratios (similar to the impedance) necessary to produce scattering parameters. These parameters, also called S-parameters, describe the electrical behavior of linear electrical networks when undergoing various steady state stimuli by electrical signals.

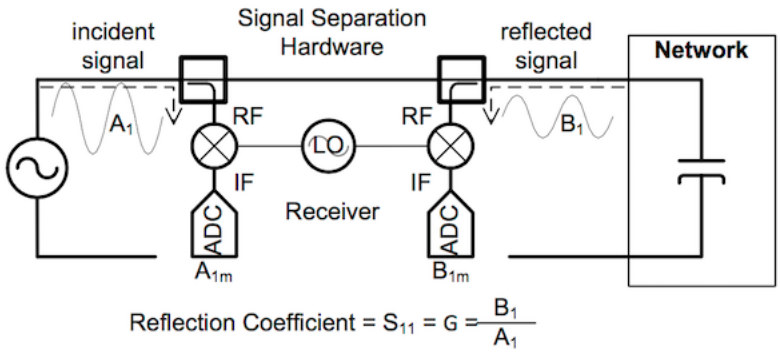

Figure 4.5: Schematized architecture of a simplified VNA. The signal separation hardware separates incident and reflected waves using directional couplers.

The primary use of a VNA is to determine the S-parameters of a myriad of passive components, such as cables, filters, switches, bridges, transformers, attenuators, antennas, and so on. In addition, VNAs can also characterize active devices such as transistors and amplifiers using S-parameters, as long as they are operating in their linear mode of operation. High-frequency devices can have one or two or more ports.

Over time, VNAs have even found their way into applications besides the pure S-parameter measurement capability. Nowadays, the VNA has also become widely used in signal integrity applications. In fact, the relatively high dynamic range of a VNA, in comparison to the traditional oscilloscope, makes it a useful diagnostic tool. Additionally, electromagnetic imaging is one of the growing fields where VNA technology is fast becoming an essential tool since it is possible to reconstruct images from reflected waves by performing a form of scanning.

S-parameters

S-parameters provide complete insight into the linear behavior of RF and microwave components and are independent of the characteristics of the VNA itself. Through the VNA calibration, impairments of the instrument are completely removed from the measurement. Thus, S-parameters are an extremely accurate representation of the linear behavior of the component under test, describing how it behaves and how it interacts with other devices when cascaded. These parameters are usually given as a function of the frequency and they are the result of solving a set of equations after measuring ratios of wave quantities while exciting the device at its various ports, since they are not directly measurable.

Let's consider a wave generator. It has a certain source impedance, and the electrical power travels across the wire from the source to the load as the combination of an electric and magnetic field, whose propagation speed (v_p) depends on the dielectric properties of the medium. The wavelength λ of the electrical signal is defined as

$$\lambda = \frac{v_p}{f_0}$$

where f_0 is the sine wave generator frequency. If f_0 is low, λ is large, and the length of the cable is negligible compared to the size of the wavelength, so that the measured voltage and current are independent of the location on the cable (Figure 4.6).

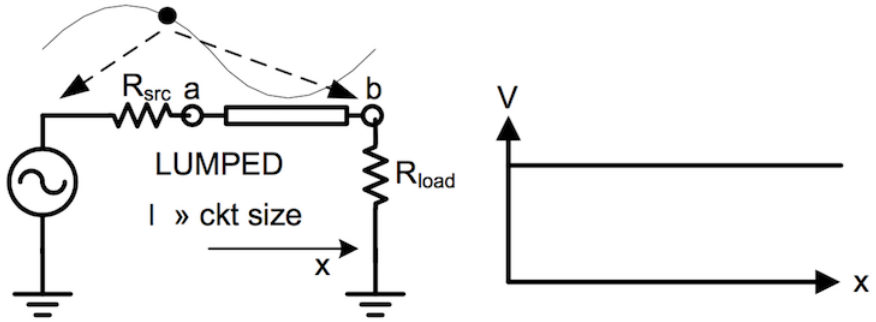

Figure 4.6: A Lumped Circuit.

In the other hand, as frequency increases, the wavelength eventually becomes similar in size or even smaller than the length of the cable, and consequently the measured voltage and current will depend on the position (Figure 4.7). Thus, measuring the voltage with a voltage probe is invalid because the result will be dependent on the probe's position. In this case, the circuit must be treated as a distributed element circuit rather than as a lumped circuit. Analysis of a distributed circuit is complex and involves the use of transmission line theory.

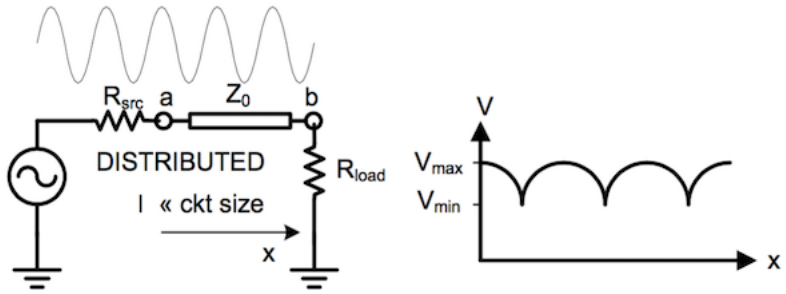

Figure 4.7: A Distribuited Circuit.

Broadly speaking, transmission line theory states that it is possible to think of the electrical power as it travels along the line starting from the source. While traveling, a certain voltage and current relation is imposed by the electrical properties of the line. In fact, the cable itself will behave such that it is characterized by an inherent impedance that does not change as long as the properties of the line or cable do not change. This impedance is called the characteristic impedance (Z_0, that is considered to be real). When the electrical power hits the termination (R_{load}), the voltage to current relationship is now imposed by the impedance of the load. If the

load impedance is equal to the characteristic impedance, the power is fully absorbed, whereas if the load impedance is different from the characteristic impedance, the ratio of voltage and current will change at the point where the transmission medium occurs. As a result, the load will not absorb fully the power, and a portion of the power will travel back toward the source. Now it is clear that the system is characterized by both an incident and reflected wave. Thus, while measurements from simple volt and current meters are able to determine impedances and transfer functions of circuits at lower frequencies, measuring similar characteristics at higher frequencies requires the measurement of incident and reflected waves. One of the most important functions of a VNA is to separate these incident and reflected waves by means of either couplers or bridges in order to measure each of these waves independently. The magnitude and phase relationship between incident and reflected waves are described by S-parameters.

An intuitive example of S-parameters can be taken from field of optics, that is the behavior of light through varying transmission mediums. Let's consider a light beam shining on a lens; some light will pass through the lens, undergoing the influence of the lens. However, some light will also be reflected back by the lens towards the direction of the light source. Once the light passes through the lens, if there is no obstacle behind the lens, the light will continue to travel forever. If an obstacle exists, part of the transmitted beam is reflected back towards the lens. This light will be partially reflected back towards the obstacle and will be partially transmitted through the lens. Thus, the reflection from the obstacle is added to the initial reflection from the light source. As a result, the reflected wave before the lens consists of two parts: the original beam reflected by the lens and a part of the reflection from the obstacle. Similarly, the transmitted wave consists of the original beam transmitted through the lens and partially the reflected beam from the obstacle (Figure 4.8).

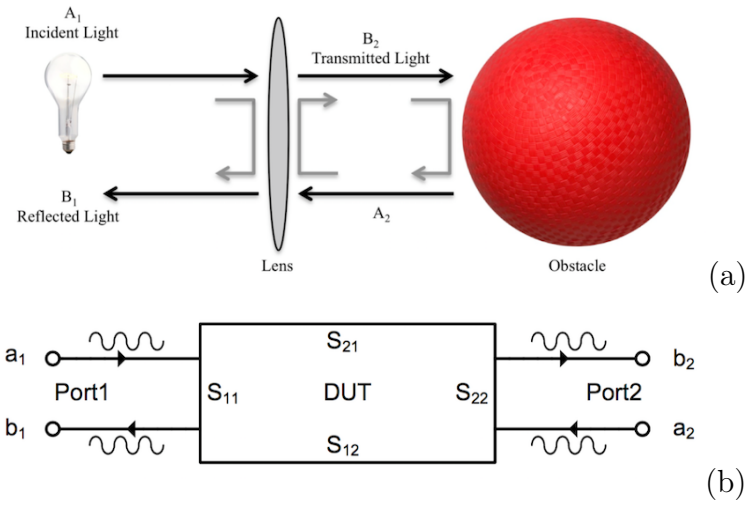

Figure 4.8: (a)Optical equivalent of S-parameter behavior. (b) A two-port device under test (DUT) along with the corresponding four S-parameters and the four waves [52].

This example can be easily translated to the electrical circuit's problem, since lens and light act like DUT and waves. Both the B_1 and the B_2 waves can be described as a combination of both the A_1 wave and the A_2 wave. These relationships can be formally represented as S-parameter equations for a two-port device as follow (Equations 4.3)

$$\begin{aligned} b_1 &= S_{11}a_1 + S_{12}a_2 \\ b_2 &= S_{21}a_1 + S_{22}a_2 \end{aligned} \tag{4.3}$$

For a generic multi-port network, the ports are numbered from 1 to N, where N is the total number of ports. For port n, the associated S-parameter definition is in terms of incident and reflected 'power waves', a_n and b_n, respectively. Kurokawa [53] defines the incident and reflected power wave for each port as (Equation)

$$\begin{aligned} a &= \tfrac{1}{2}k(v + ZI) \\ b &= \tfrac{1}{2}k(v - Z^*I) \end{aligned} \tag{4.4}$$

where Z, is the diagonal matrix of the complex reference impedance for each port and Z^* is the complex conjugate, V and I are respectively the column vectors of the voltages and currents at each port and k is defined as

$$k = |\mathfrak{Re}(Z)|^{-1/2} \tag{4.5}$$

According to Equation 4.3, a wave leaving the DUT (b_1 or b_2) is a linear combi-

nation of the waves entering the DUT (a_1 or a_2), so that terminating the DUT in the characteristic impedance (Z_0) allows the extraction of the individual S-parameters. S_{11} and S_{21} are determined by measuring the magnitude and phase of the incident, reflected and transmitted voltage signals when the output is terminated in a perfect Z_0 (a load that equals the characteristic impedance of the test system). This condition guarantees that a_2 is zero, since there is no reflection from an ideal load. S_{11} is equivalent to the input complex reflection coefficient or impedance of the DUT, and S_{21} is the forward complex transmission coefficient. Likewise, by placing the source at port 2 and terminating port 1 in a perfect load (making a_1 zero), S_{22} and S_{12} measurements can be made. S_{22} is equivalent to the output complex reflection coefficient or output impedance of the DUT, and S_{12} is the reverse complex transmission coefficient (Figure 4.9). By setting the reflection parameters to zero, it is possible to derive the equation for S-parameters:

$$\begin{aligned} S_{11} &= \frac{reflected}{incident} = \frac{b_1}{a_1}\bigg|_{a_2=0} \quad S_{12} = \frac{trasmitted}{incident} = \frac{b_1}{a_2}\bigg|_{a_1=0} \\ S_{21} &= \frac{trasmitted}{incident} = \frac{b_2}{a_1}\bigg|_{a_2=0} \quad S_{22} = \frac{reflected}{incident} = \frac{b_2}{a_2}\bigg|_{a_1=0} \end{aligned} \tag{4.6}$$

As a consequence of Equations 4.6, the parameters S_{11} and S_{22} are called reflection coefficients , whereas S_{12} and S_{21} are called transmission coefficients.

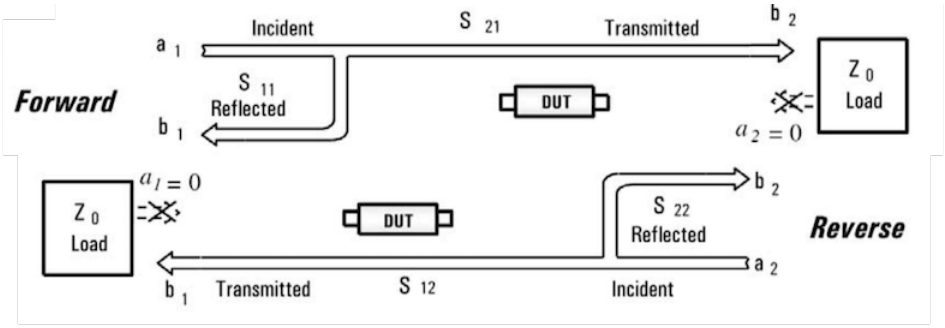

Figure 4.9: Measurement of S-parameters [54].

Ratios shown in Equation 4.6 are complex-valued, and they carry both a magnitude and phase component as a function of frequency. According to the common notation, S_{mn} is the S-parameter corresponding to the m-th receiver port and the n-th source port. Thanks to this convention, it is possible to write the S-parameters matrix for a any number of ports:

$$S = \begin{bmatrix} S_{11} & \cdots & S_{1n} \\ \vdots & \ddots & \vdots \\ S_{n1} & \cdots & S_{nn} \end{bmatrix}, \qquad S_{ij} = \left.\frac{b_i}{a_j}\right|_{a_k=0}, \forall k \neq j \tag{4.7}$$

In theory, determining the S-parameters using a VNA is a straightforward process. In practice, however, it is impossible to terminate the port opposite to the driving port exactly in the characteristic impedance (Z_0), resulting in the presence of a reflected wave at all times. A solution of this problem is to first connect the source to port 1 and terminate port 2, which allows the VNA to measure ratios b_1/a_1, b_2/a_1 and a_2/a_1 as a function of frequency. Next, for a two-port device, the VNA switches the source to the output and terminates the input port of the DUT. With this configuration, the VNA can now measure ratios b_1/a_2, b_2/a_2 and a_1/a_2. Using basic linear algebra, it is possible to calculate the S-parameters as a function of frequency.

In practice, a VNA will generally measure the incident and reflected waves through a series of couplers or bridges, referred to as directional devices. The directional device is able to separate the incident from reflected waves. Using this measurement practice, the resulting measurements will be quantities that are subject to imperfections of the VNA, such as the coupling factor and directivity of the directional devices. Thus, more complicated calculations are needed in order to determine calibrated S-parameters starting from a set of raw quantities.

Copper Mountain - S5048 VNA

In this work it has been used the S5048 VNA (Figure 4.10) developed by Copper Mountain Technolo- gies. The highly compact S5048 VNA is a 4.8 GHz, 2-port instrument, capable of 120 dB dynamic range and designed for operation with PC. The key features are:

· Frequency range: 20 kHz - 4.8 GHz

· Measured parameters: S11, S12, S21 and S22

· Wide output power adjustment range: -50 dBm to +5 dBm

· 120 dB dynamic range (10 Hz IF bandwidth)

· Measurement time per point: 200 μs per point

· Up to 200,001 measurement points

· Multiple precision calibration methods and automatic calibration

Figure 4.10: Copper Mountain - S5048 VNA.

This kind of VNA uses a single RF source that is switched between port 1 and port 2. This single source is used to create the incident "a" waves, which are used as the reference signals in determining the S-parameters. Because there is only one source, and because S-parameters are defined as having only one port driven at a time, a two port VNA is said to have a forward and reverse state. In the forward state, port 1 is driven by the RF source, and an incident wave is produced at this port while port 2 is terminated; during this state S_{11} and S_{21} are measured. In the reverse state, port 2 is driven by the source and an incident wave is produced at port 2 while port 1 is terminated during this S_{22} and S_{12} are measured [55].

As previously mentioned, the VNA is connected to the computer via USB and delivers accurate testing and measurement through a graphical interface distributed by Copper Mountain Software. The S- parameters are measured as a function of the frequency (Figure 4.11), and can be expressed as complex values (module and phase) or gain (dB), write as:

$$g = 20log_{10}(S_{ij}) \tag{4.8}$$

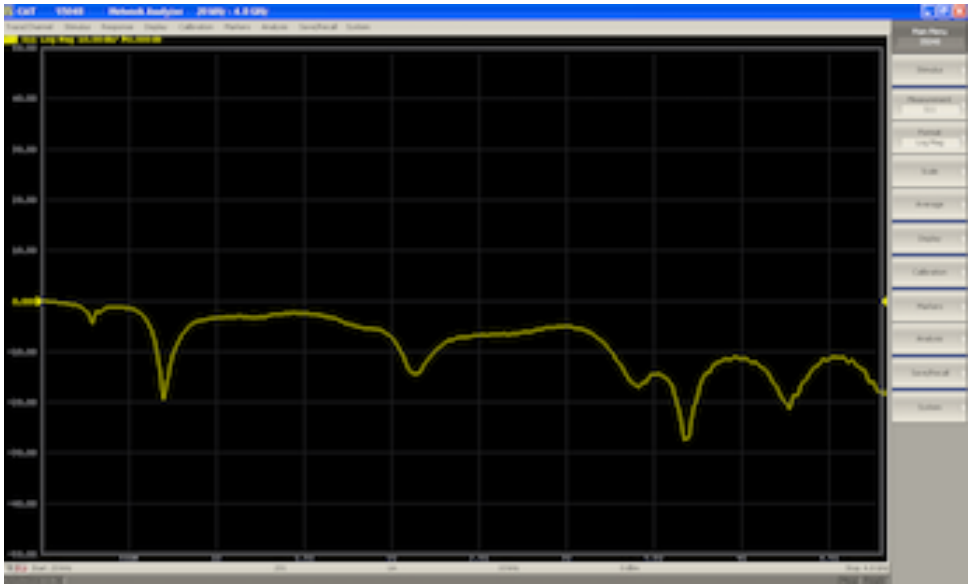

Figure 4.11: Graphical interface of Copper Mountain Software: the trace in the graph is the Log Mag (gain signal) of S11 collect by the antenna ANT-24G-905-SMA, in oil medium with alcool scatterer.

In this thesis only S_{11} was used, since the measurements were perfomed employing only one antenna and the aim was to measure the wave reflected by the scatterer. For every antenna's position and frequency, real and imaginary part of this S-parameter were acquired and saved in a .csv file used in further steps of this work.

4.2.3 Mechanics

In order to automatically perform the measurements, a precision motor (CR1/M-Z6 ThorLabs driven by OptoDCDriver ODC001 (Figure 4.12)) was used for the rotation of the breast phantom. It was driven by a LabView software developed during this work and integrated in the in the main LabView Virtual Instrument (VI) in order to synchronize the motion of the phantom and the data acquisition.

The OptoDCDriver is a very compact single channel DC servo controller and driver designed to operate with a veriety of DDC brushed motors up to 5V operation equipped with encoder feedback. This driver unit contains a full embedded controller and driver circuit that can operate with or without a PC. Although compact in footprint, this unit offers a fully featured motion control capability including velocity profile settings, limit switch handling, "on the fly" changes in motor speed and direction for more advanced operations. The OptoDCDriver has been specifically de-

signed as a member of the Advanced Positioning Technology (APT) controller family, that incudes high specification motors and piezo controllers aimed at high resolution positionning applications.

The CR1-Z6 motor has been developed for use in high precision applications, and it provides 360° of continuous high repeatibility motion. It utilizes a 12V DC servomotor that provides sufficient torwque for high load capabilities. Utilizing a 256:1 gear reduction, the rotator provides minute movements over the entire travel range.

(a)


(b)

Figure 4.12: (a) CR1/M-Z6 ThorLabs and (b) OptoDCDriver ODC001.

During the preliminary phase, a mechanical system was developed in order to connect the motor and the breast and allow the rotation.

As a first step, two aluminum supports were designed to fix the pulleys. Some holes were made in the bigger bracket with the aim of inserting and supporting tumor's phantoms (Figure 4.13). Secondly, a wooden handmade structure was devised and produced with the goal of supporting the motor and the breast phantom.

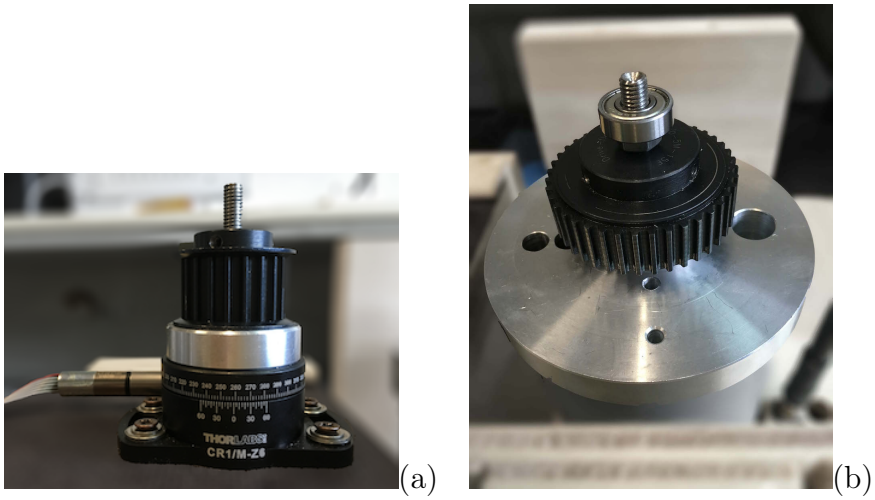

(a) (b)

Figure 4.13: (a)Pulleys supports for motor and (b) breast phantoms connected though a belt.

4.3 LabView Software

In this thesis, a software was specifically developed in order to realize an automatic acquisition system, able to drive both the Vector Netweork Analyzer and the stepper motor, and also accomplish the image reconstructions over a selected range of frequencies. This software was realized through LabView that gives the opportunity to realize an user-friendly interface, where parameters are set and virtual indicators show the progress of the acquisition phase (Figure 4.14).

Figure 4.14: User interface of the software realized to perform data acquisitions.

The SubVirtualInstrument developed receives as inputs the maximum and minimum value of the frequency range and the number of frequencies to span the selected range. At each stage of the acquisition process the corresponding virtual led is turned on. Also, the user can select the range of the frequencies on whitch the reconstruction is accomplished. The drivers supplied by Copper Mountains and ThorLabs were essential to correctly synchronize motion and acquisition.

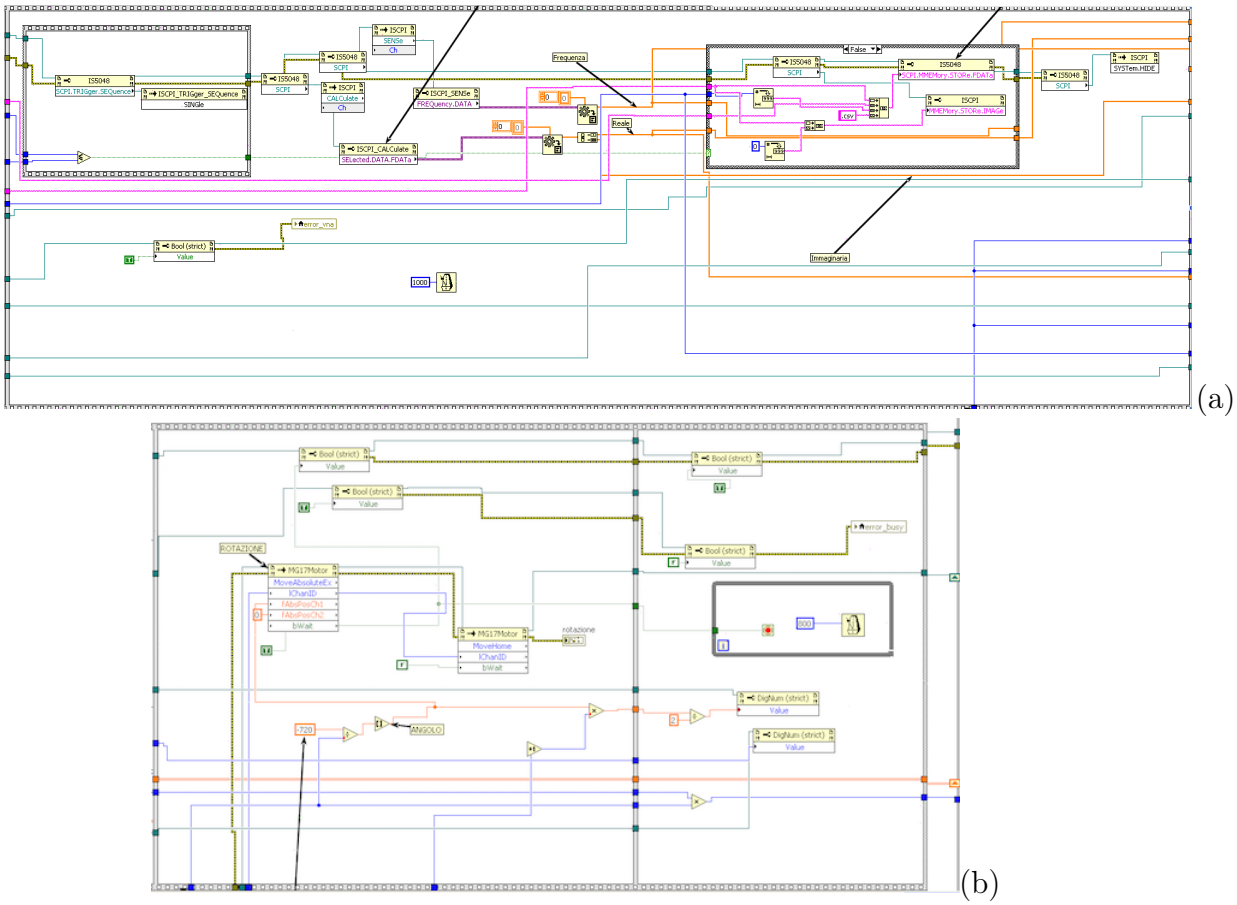

Figure 4.15: Two core parts of the LabView software: (a) once the VNA is turned on, data are aquired as Real and Imaginary part and the saved in a .csv file, for each antenna position. (b) The motion of the breast is accomplished by the motor, that is connected to the phantom with a gear ratio of 1:2, such that a complete rotation of the breast corresponds to a 720° rotation of the motor.

4.4 Preliminary Prototype for Multistatic configuration

During the study of the experimental set-up, in order to study the antenna management, a preliminary prototype for multistatic logic was developed. Figure 4.16 shows a circuit in which are embedded 12 leds, a switcher and two transistor arrays ULN2003A. When the switcher is turned on and the I/O device is connected to the LabView software, the first green led turns on and the yellows are turned on in sequence, as if they were receiving the signal emitted by the green led. Then the first green led turns off, and the second green led turns on and the simulated acquisition starts again, and so on. If the switcher is turned off, the sequences pauses untill it is turned on again.

This prototype wasn't used for any pratical application in this work, but it represents a preliminary work for further studies in microwave imaging which may involve the application of a multistatic approach.

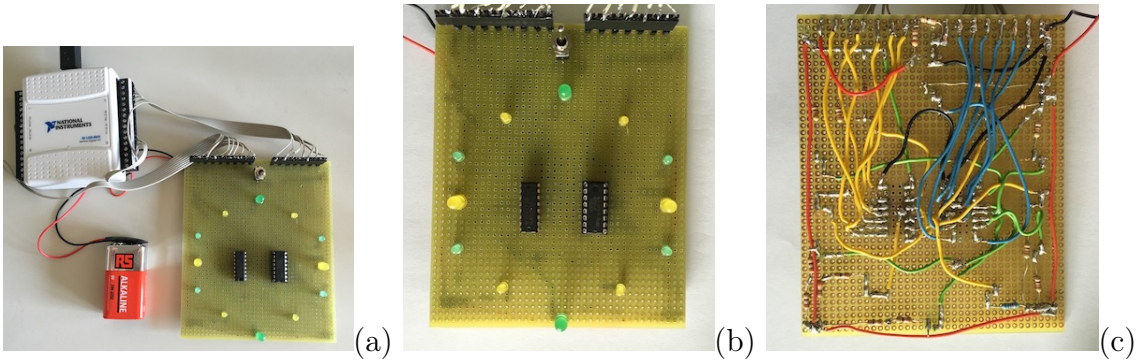

(a) (b) (c)

Figure 4.16: (a) National Instruments NI USB-6501. (b) Front and (c) rear of the prototype. Green leds stand for the transmitters, whereas yellow leds represent the receivers.

Chapter 5

Experimental Measurements

The physical basis for breast tumor detection with microwave imaging is the contrast in dielectric properties of normal and malignant breast tissues. In the monostatic approach exploited in this thesis, the breast is illuminated by an antenna from different positions from where the back-scattered signal is also acquired, and then the images are obtained though TR-MUSIC algorithm. From a technical point of view, the chief motivation for developing a microwave imaging technique for detecting breast cancer is the high expected contrast in the dielectric properties at microwave frequencies between normal adipose and malignant breast tissue. A big drawback of this approach is that the contrast between normal fibroglandular and malignant tissue is inferior than the adipose tissue. In spite of this physical limitation, microwave imaging is a very attractive approach since overcomes problems given by other imaging techniques, such as the employiment of ionizing radiations. However, the knowledge of dielectric parameter of breast tissues are not still completely clear, so the working framework must to be further investigated. Also, another big issue of this approach is that microwave imaging doesn't offer a spatial resolution high as in other diagnostic methods, such as X-Rays or MRI, which offer high contrast with respect to physical or physiological factors of clinical interest, such as water content, vascularization/angiogenesis, blood-flow rate, etc [56].

In this work, both hardware and software for an automatic microwave imaging system have been developed (§4.2,4.3). The goal is to characterize the imaging system and reconstruction algorithm starting from an ideal scenario where the tumor is inserted in a completely homogeneous medium, and later test the experimental setup on a more realistic configuration in which a disomogeneity is also embedded in addition to the tumor.

Spatial and contrast features (§3.4) of this system are analyzed in order to un-

derstand its optimal working range. All the measurements were perfomed using seed oil as coupling and background medium, varying size and dielectric properties of the scatterer. After the first steps, a study in the heterogeneous case was accomplished. All these measurements were performed using high[1] cylindrical tubes of different diameters to exploit the infinite cylinder approximation (Appendix B). Many different configurations were studied , changing the tumor dimension, position and its dielectric properties. Recalling the geometry of our phantom as concerns the possible locations and dimensions of our tumor phantom

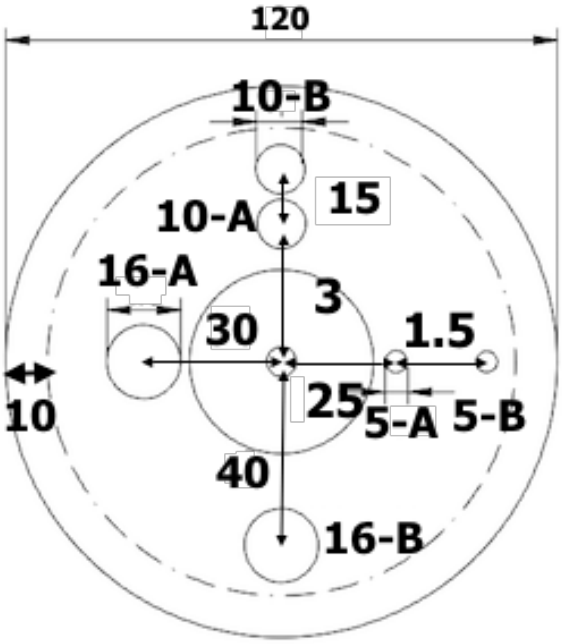

Figure 5.1: Different positions for tumor breast phantom of our acquiring system. Dimensuons are reported in mm.

we report the summary table of the diffrent configurations

[1]All the cylinders were characterized by an height equals to 50cm.

	diameter (mm)					
	homogeneous medium				heterogeneous medium	
ε	16	10	5 - A	5 - B	16 - A	16 - B
2.5	X	X				
3.4	X	X				
4.4	X	X	X	X		
8.1	X	X	X	X		
11.8	X	X	X	X		
15	X	X	X	X		
21	X	X				
24	X	X		X		
35	X	X	X	X		
47	X	X				
54	X	X			X	X
58	X	X				
70	X	X	X	X		
81	X	X	X	X		

Table 5.1: Summary of all the measurements sessions carried on in this work. "A" and "B" stand for the inner and outer position, respectively

As last step of the measurement session, a finite dimension scatterer was used to study the behaviour of this microwave system varying the distance between the target and the antenna's plane. Thanks to these measurements, 3D reconstructions were also realized through a proper algorithm able to exploit the additional information along the height. The results that have been achieved in this last stage derive from the partnership with Musca L. [57], colleague candidate responsible of 3D modelling and reconstructions.

5.1 Working Frequency Range Characterization

In this section, single-frequency reconstructions areare studied as a function of the frequency, scatterer diameters and dielectric properties. Contrast is studied by mean of SMR, that is a measure of rate between signal intensity and background clutter. In other words, SMR measures the amount of signal in respect of the quantity of clutter. To study the way in which the target is reconstructed, this parameter has to be calculated in the Region of Interest (ROI) surrounding target position.

This parameter was initially calculated in the area surrounding the maximum value of the pseudospectra. This ROI was selected through and automatic algorithm able to find the highest value in the pseudospectrum and select a region around

it equals to the 20% of the image. This approach is convenient in high contrast situations, where the presence of artefacts is neglectable. Since one of the aims of this work was to study the performances of the experimental set-up in low-contast conditions, an User Interface was developed. Thanks to this tool, the position of the tumor was manually selected and the SMR computed around this area. Following this method, we obtained two measures of SMR (SMR_{auto} and SMR_{man}), from which it is possible to study the behaviour of the imaging system and the reconstruction process. We expect to find well localized and clutter free reconstructions in high constrast scenarios, and a growing degradation as the dielectric properties of the scatterers lowers themselfs. Due to the intrinsic features of TR-MUSIC algorithm in monostatic configuration, we also expect a puntciform-like reconstructed target and no specific connection between the target dimensions and the reconstructed ones. Moreover, some artefacts could be reconstructed, and in certain conditions their signal could be higher than the one given by the target. Also, to estimate the errors and obtain stable values, three measurements for every size and dielectric properties were performed. SMR_{auto} and SMR_{man} are reported as a mean value and error bar calculated over this set of measurements as follows

$$\Delta = 1.96\sigma \tag{5.1}$$

where σ is the standard deviation.

5.1.1 Localization and Contrast vs Frequency

At this preliminary stage, the goal is to evaluate the optimal working range of the antenna. It is a WiFi antenna and its logsheet reports a working frequency range in air included between 2.4 and 2.5GHz. For our purposes, it is possible to find other or larger reliable working intervals, also as a consquence of the fact that the antenna is immersed in seed oil. To do this, we acquired the antenna signal over a wide range of frequencies (0.1-4GHz). Plotting these measured values as a function of the frequency (Figure 5.2), we note the presence of two different pleateau and three deep peaks, meaning that an only in three tight frequency ranges the has an high efficiency. Also, the frequency working range suggested by the constructor is exactly on the slope of one of these peaks, that appear to be slightly left-shifted in comparison to the air medium measurement (not reported).

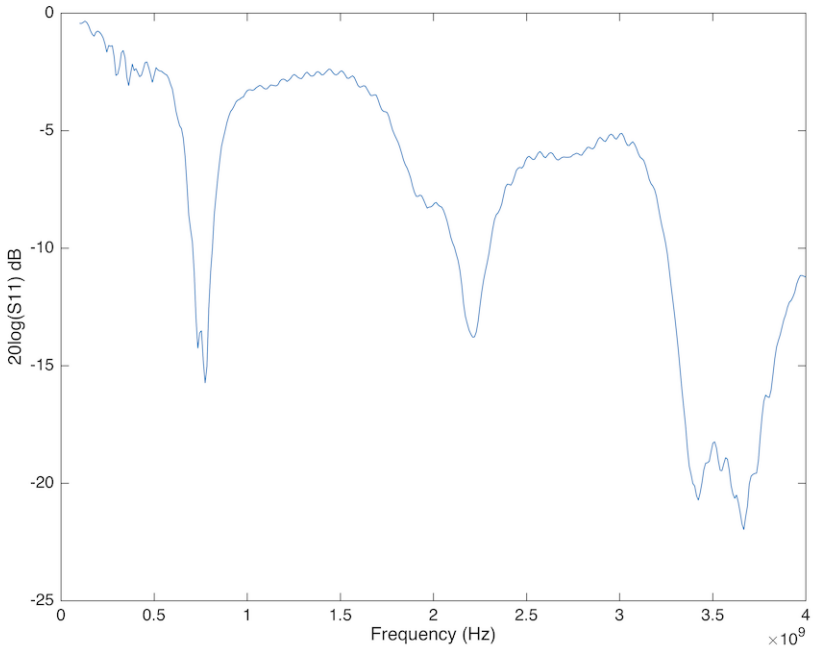

Figure 5.2: S_{11} signal (dB) as a function in the frequency range 0.1-4 GHz of the antenna in oil medium.

To exploit all the ability of our algorithm, we need to perform muti-frequency reconstructions over a wider range of frequencies than the one given by the constructor. To carefully select the frequency range, different acquisitions were carried out using the 5mm, 10mm and 16mm scatterer filled with solutions characterized by high dielectric constants, and delocalization of the target position in single-frequency reconstructions was studied as a function of the frequency.

Single-frequency reconstructions tend to produce Delta-like sources which create a punctiform peak in the pseudospectrum, and the localization of this kind of target corresponds to the position of the maximum value of the pseudospectrum. In real cases, the source has finite spatial dimensions that produces a spread peak, but the maximum of the pseudospectrum can still be considered a good extimation of the target position. Hence, in order to obtain a well reconstructed multi-frequency image, it is required a correct localization of the scatterer in the single-frequency pseudospectra, else the target will be represented as a wide peak in the final image. So far, we have seen that our imaging system produces high contrast images only in a tight frequency range in respect of the available one. In the next step, it will be studied the distribution of the maximum values of the single frequency pseudospectra as a function of the frequency. In order to study the correct scatterer localization,

the maximum position was plotted for every single frequency reconstruction. First of all, it will be shown that an high SMR value doesn't stand necessarly for a well reconstructed image, since strong artefacts, even higher than the signal, may be reconstructed instead of the scatterer.

In Figure 5.3 a, b the colours stand for respectively the frequency and SMR range at which they belong to. It is interesting the comparison between those two images, because the high values of SMR don't tend to group around the correct target position but, on the contrary, they tend to cluster in wrong positions.

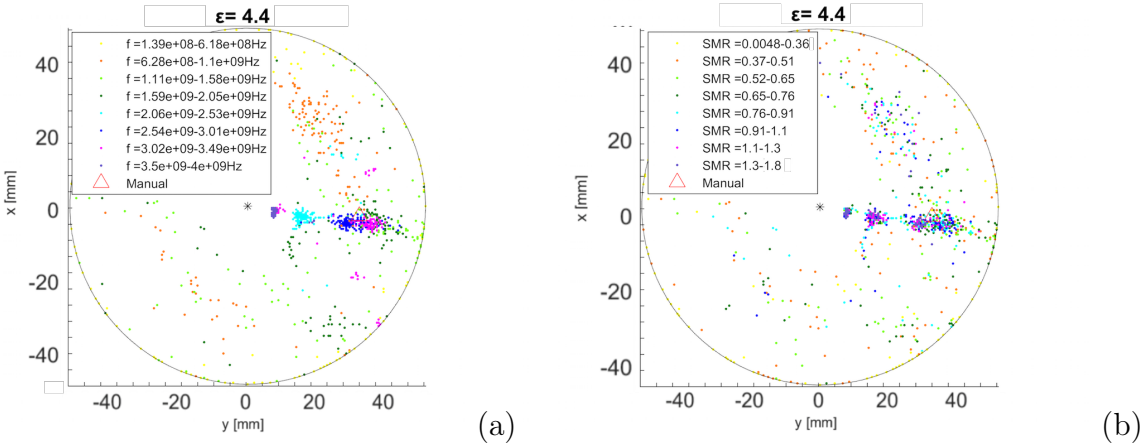

Figure 5.3: Distribution of the maxima computed on the data corresponding to the 16mm scatterer filled with the same solution. Colours show (a) the frequency and (b) the SMR range at which points belong to. SMR was computed over the maximum value of each pseudospectrum. The red triangle stands for the location identified by user interface. i and j are the indexes of the pseudospectrum matrix.

This is the worst scenario because multy-frequency reconstruction could not be able to neutralize the presence of "random" delocalization. Indeed, multi-frequency reconstruction produces a reconstructed image where each single-frequency contribution has a low weight on the final result, so that if no cluseter of artefacts is present, these wrong reconstructions are simply neglectable. On the contrary, if the maxima tend to group in certain areas, the final result will be strongly affected by artefacts, which also could be more relevant than the target contribution. For this reason, in sight of further measurements, it is very important to carefully select the optimal working range of this acquisition system.

In Figure 5.4 the distribution of the maximum is shown for scatterer filled with solutions characterized by different dielectric constants. When the scatterer is filled with oil (Figure 5.4a, b), the points are very spread out and no well defined cluster is present. Rising ε, points slightly group in some different areas, but only the

maxima belonging to a certain frequency range cluster around the real target position. Indeed, maxima are very spread out at low frequencies, whereas at high frequencies they tend to produce cluster of artefacts. Also, using scatterers of high dielectric parameters (Figure 5.4d) most of the maxima are clustered in the area surrounding the scatterer position, but with a large variation along the radial direction. Observing the frequencies which well localize the target, we notice that they belong to the deepest plateau in Figure 5.2, meaning that the acquisition system works properly only in the frequency range in which the aquired signal is relatively high and the antenna behaviour in quite stable aswell. Indeed, higher frequencies at which S_{11} shows a very deep peak (3.5GHz), strong artefacts may be produces (Figure 5.4).

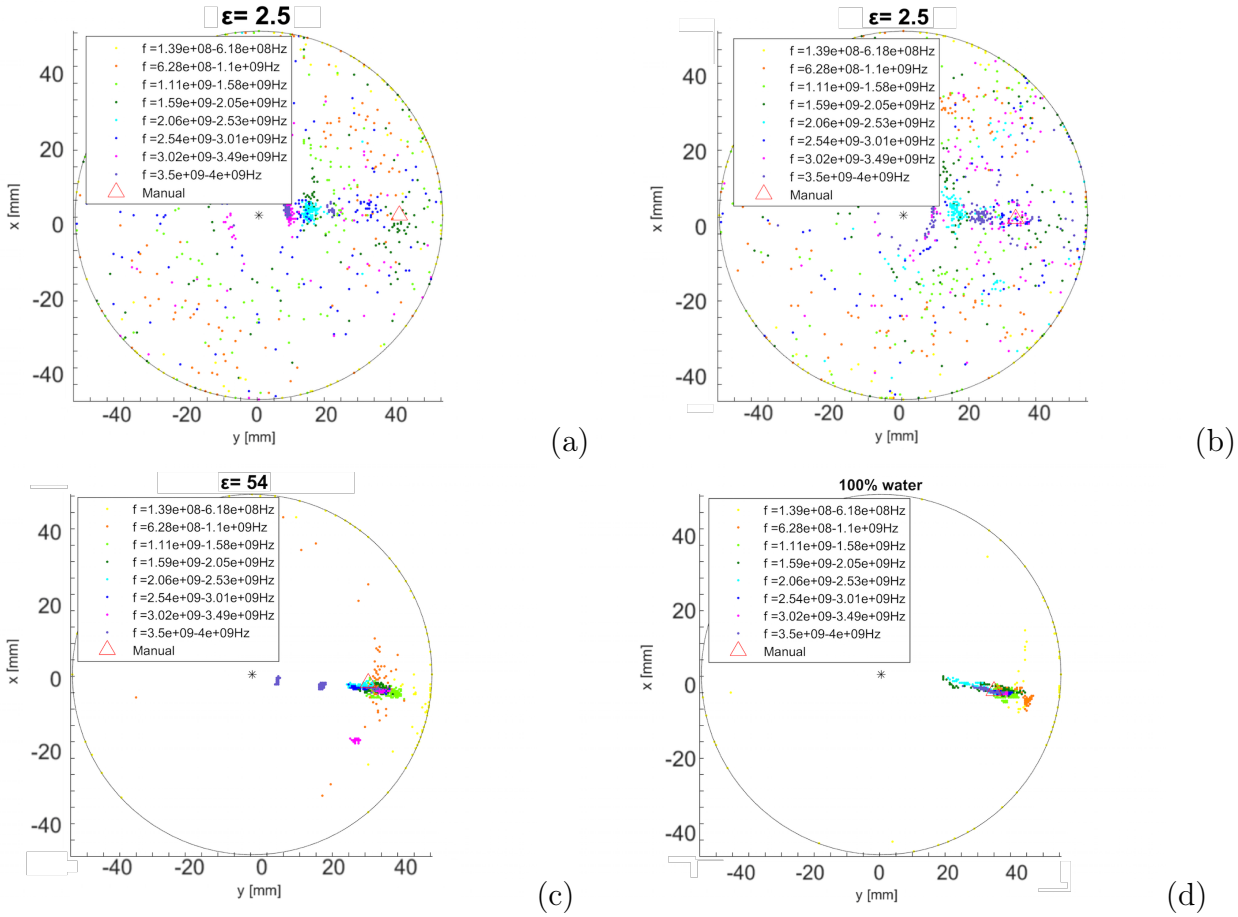

Figure 5.4: Union of the distributions of the maxima belonging to every single-frequency pseudospectrum of the three measurements accomplished for every sample, correspond to 16mm (a,c,d) and 10mm (b) diameter scatterer.

As a result of the considerations previously expressed, we discarded the signal given by the frequencies lower than 2.5GHz and higher than 3.2 GHz, that represents

our optimal frequency range. Hence, multi-frequencies studies presented in further sections were perfomed over the frequency range between 2.5 and 3.2 GHz. We could have selected a slighltly wider range of frequencies, but it is more convinient to exploit only the reliable contributes to avoid to ruin the reconstructed image.

Figure 5.5 shows the maximum localizations in the optimal frequency range through a comparison between the tumor position manually selected and the mean value and error bars [2] of the maximum distribution. In both cases the user selection belongs to the maxima distributions corresponding to the selected frequencies, and as the dielectric constant of the scatterer increases the error bars quickly decreases, that is the distribution tights itself around the real position of the scatterer.

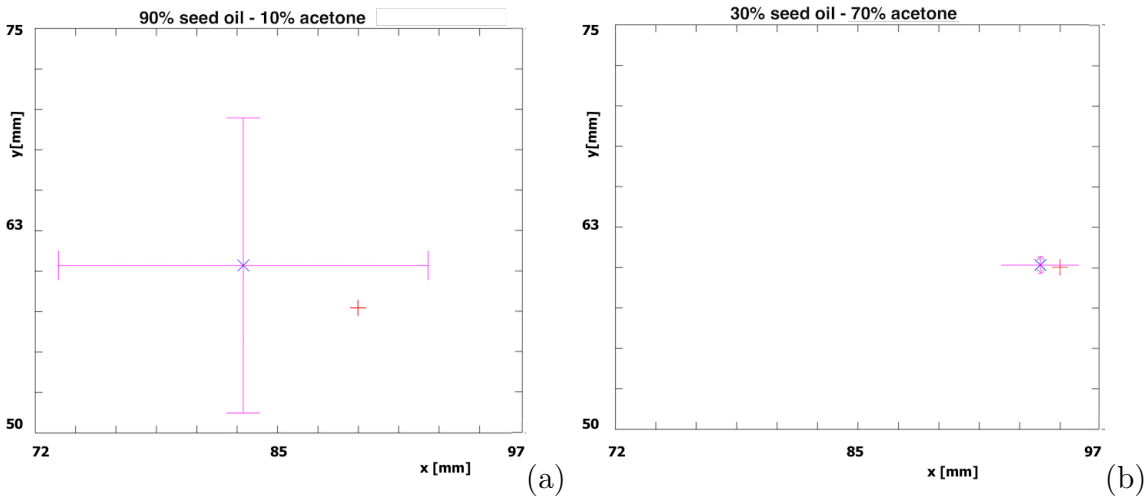

Figure 5.5: Comparison between the 10mm diameter scatterer position selected by user interface and the mean and the error of the maximum coordinates corresponding to a tight frequency range (2.5 and 3.2GHz).

A further proof to support this choice was obtainded with the 5mm diameter scatterer. Indeed, two set of measurements were perfomed with the target positioned at different distances from the center of the domain. Working at the selected frequencies, we obtained a correct localization of this scatterer aswell, and this appears to be a noteworthy results because the linear dimension of the target were really small in comparison to the wavelength of the incident waves ($\lambda \approx 7$ cm). Figure 5.6 shows some comparable examples of the maxima distribution in the optimal frequency range. As foreseen, maxima tend to create a tighter cluster the higher ε is.

[2] Computed through Equation 5.1

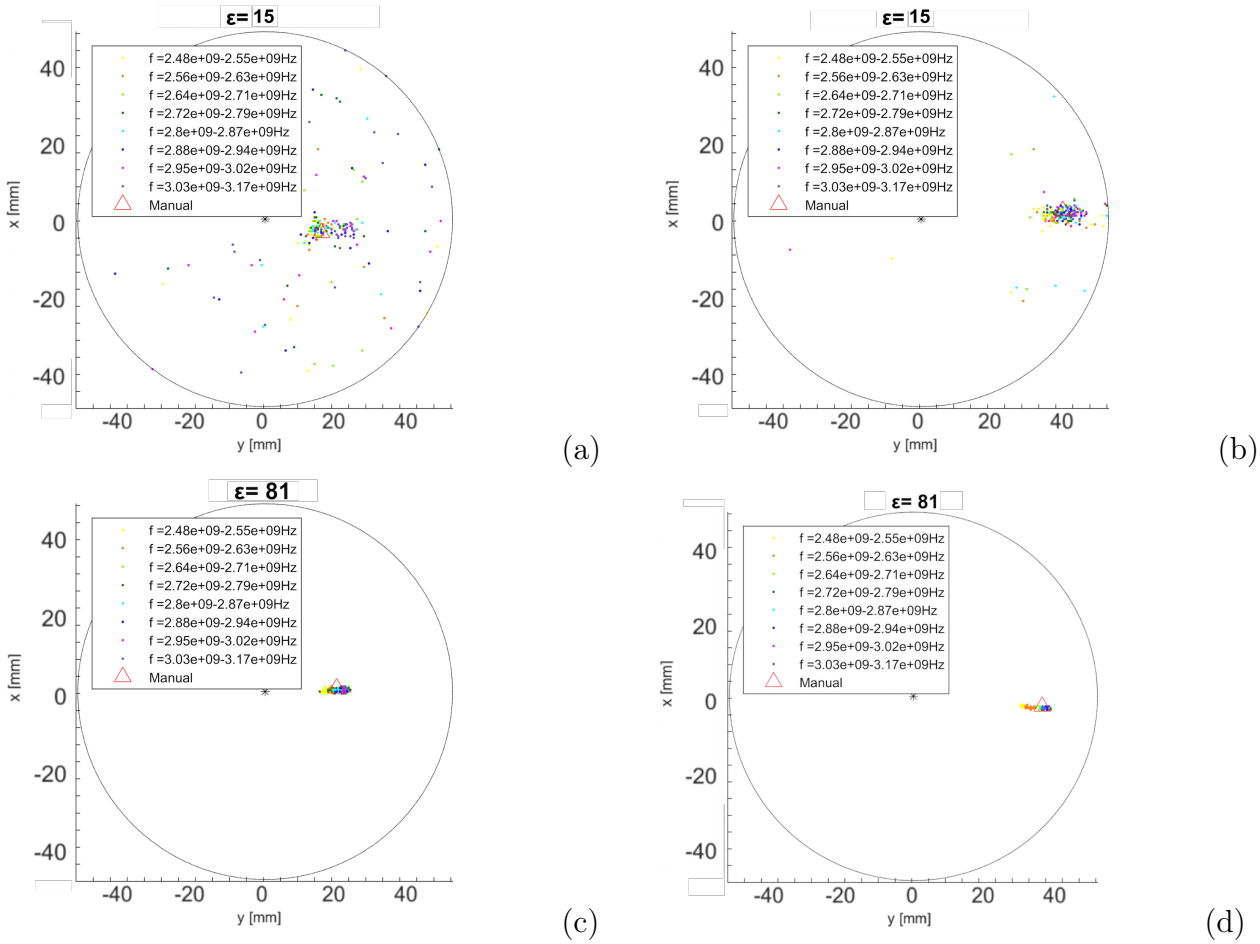

Figure 5.6: Distribution of the maxima in the optimal frequency range. The 5mm dimeter scatterer, filled with different solutions, is correctly localized in both internal (a,c) and external (b,d) position.

Figure 5.7 shows a comparison between two reconstructed images of the same scattering configuration. In both of them the target is correctly reconstructed through IMUSIC algorithm, but in Figure 5.7a it is clearly visible a tighter peak and also an higher dynamic than in 5.7b. This strong difference is due to the frequency range over which the reconstruction was performed. Indeed, Figure 5.7a was reconstructed over the optimal frequency range discussed above, whereas Figure 5.7b is the result of the reconstruction in the range (0.1-4) GHz. Our frequency selection produces similar results even in other scattering configurations, so we performed our further analysis only over this optimal working range.

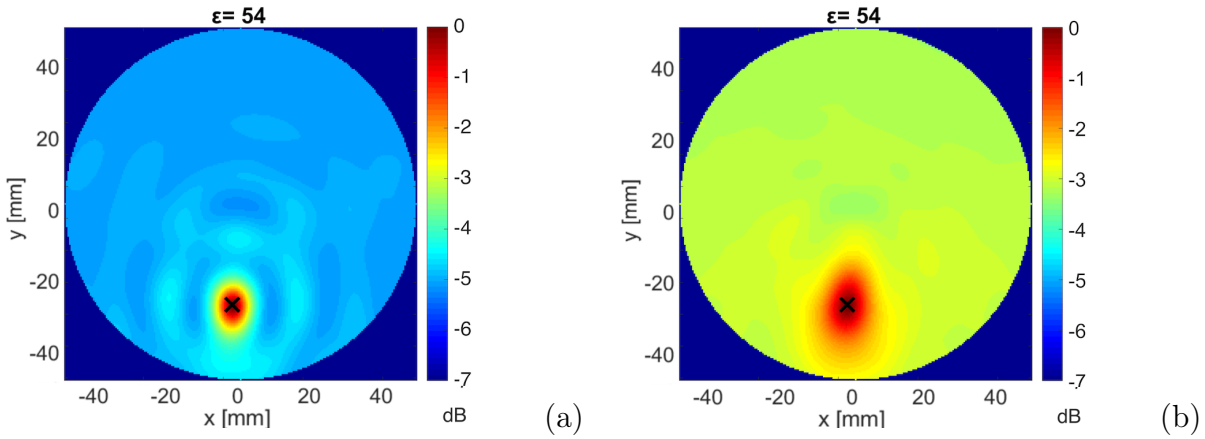

(a) (b)

Figure 5.7: Two different multifrequency images reconstructed over two different frequency range. In (a) it was used frequencies belonging to optimal range and in (b) all the frequencies available. Metrics show the difference from a numerical point of view: (a) $SMR = 1.6611$, $FWHM_\rho = 13.0479$, $FWHM_\phi = 9.4402$, (b) $SMR = 0.8933$, $FWHM_\rho = 17.9317$, $FWHM_\phi = 11.4127$.

Now, the SMR performances of our imaging system are studies as a function of the frequency. In Figure 5.8 we observe two SMR trends which are considered representative of all the other measurement sets performed with a scatterer filled with solutions characterized by high dielectric properties. We observe that SMR assumes very different values in the different frequency ranges. All of the aquired measurements show very low SMR values at low frequency and a fast increase around 1GHz. Moving toward 4GHz, SMR drops in some cases quite quickly, but later it arranges itself around relatively high values untill the 3.5 GHz step is passed and a further drop occours.

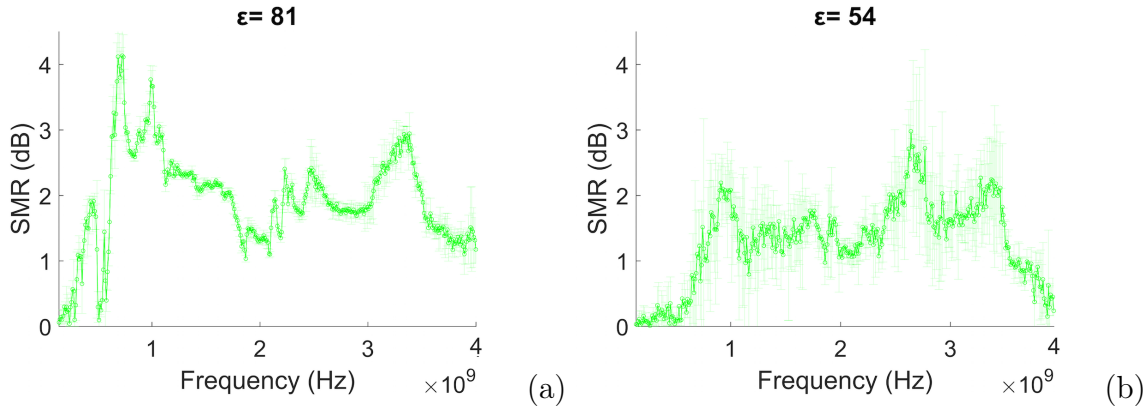

(a) (b)

Figure 5.8: SMR of the single-frequency reconstructions as a function of the frequency for (a) the 16mm and (b) 10mm diameter scatterer filled with a solution characterized by $\varepsilon = 81$ and $\varepsilon = 54$.

Lowering ε, we obtained similar trends for low frequencies. The high peak around 1GHz is very lowered now and, in addition to what prevoiusly described, an increase of SMR is visible in the range between 2.5 and 3GHz.

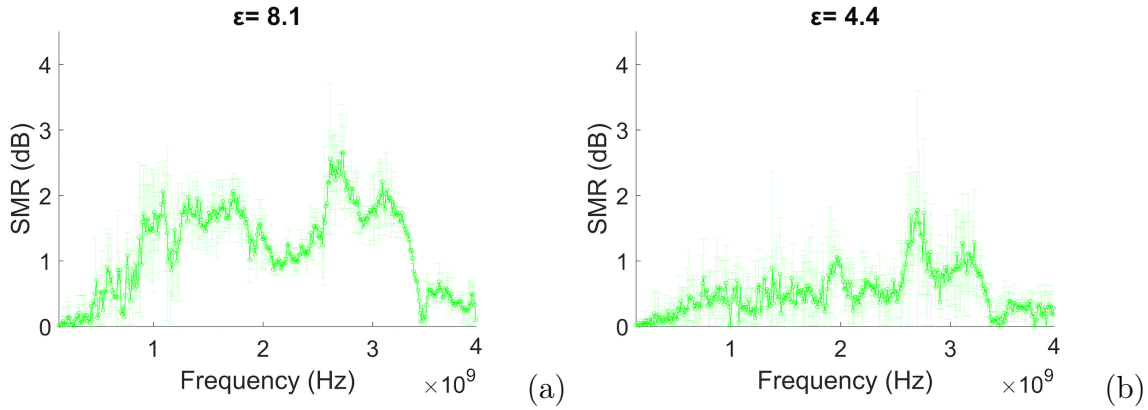

Figure 5.9: SMR of the single-frequency reconstructions as a function of the frequency for 16mm diameter scatterer filled with a solution characterized by (a) $\varepsilon = 8.1$ and (b) $\varepsilon = 4.4$.

This analysis confirms our range selection. Indeed, between 2.5 and 3.2 GHZ we obtain relativley high values of SMR over all the measurements. Sometimes high peaks are shown at very lows frequencies, but from the previous analysis about the target detection we have to discar those contributes since they don't produce a relaible tumor localization.

Finally, from the comparison between SMR trends obtained from the same scatterer filled with different solutions (Figure 5.8a and Figure 5.9 a, b) it appears that only a slight increase is given by the scatterer filled with high dielectric properities, as if the signal contrast would increase until it reaches an upper bound. This statement will be clearified in the next section.

5.1.2 Automatic ROI selection

An algorithm for the automatic tumor detection is embedded in our reconstruction tool-box. It is able to find the target position through the research of the maximum value of the signal on the pseudospectrum. Also, it automatically selects a ROI equals to the 20% of the imaging domain, in which metrics are computed.

We emploied this algorithm to calculate SMR automatically in every single-frequency reconstructions, whose values were compared with the same metric computed in the actual target position.

Figure shows a comparison between SMR_{auto} and SMR_{man} in two different scattering scenario. Il clearly appears that in Figure 5.10a the two trends correspond almost exactly, whereas in Figure 5.10b SMR_{auto} is moves away from SMR_{manual} for frequencies included between 2 and 2.5GHz and higher than 3.3 GHz. This behaviour is due to the possible creation of strong delocalized artefacts if not reliable frequencies are exploited. From this evidence a proper frequency selection appears essential.

.

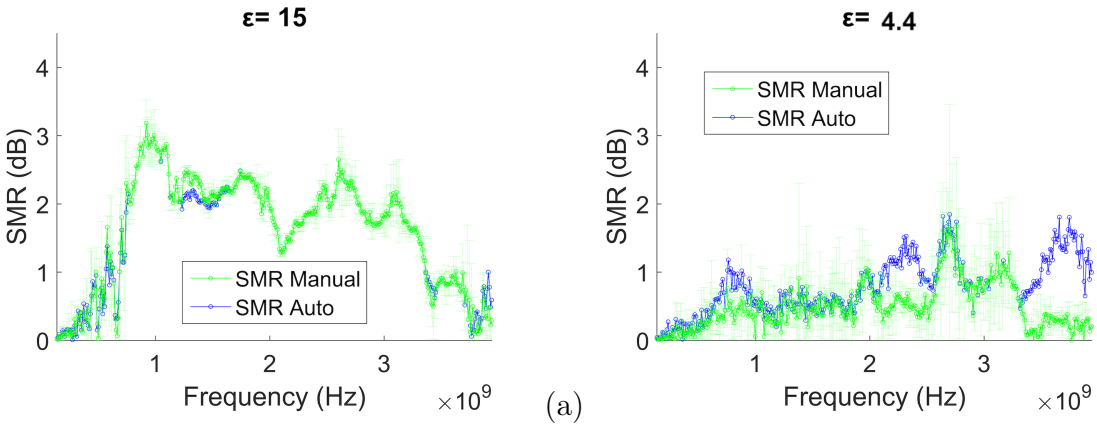

(a)
(b)

Figure 5.10: SMR_{auto} and SMR_{man} of the 16mm diameter scatterer characterized by dielectric constants equal to (a) $\varepsilon = 15$ and (b) $\varepsilon = 4.4$.

Lowering ε further, SMR_{auto} and SMR_{man} tend still to diverge, and this effect increases as ε decreases. The limit cases is when the scatterers are filled only with seed-oil (Figure 5.11), in which we would expect both SMR_{auto} and SMR_{man} values almost equal to zero, instead the presence of artefacts is still visible out of the selected frequency range.

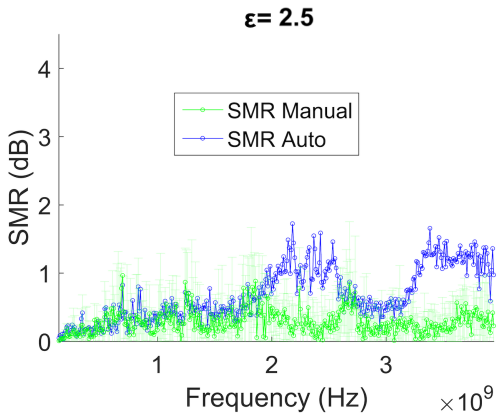

Figure 5.11: SMR_{auto} and SMR_{man} corresponding to the target filled with seed oil. Scatterer diameter equals to 16mm (a) and 10mm (b)

5.2 Multi-frequency Reconstructions in Homogeneous Medium

In the previous section, spatial feature and localization were studied as a function of the frequency in order to find the optimal working range, that was found between 2.5 and 3.2GHz. At this stage, the goal is to study spatial and contrast features as a function of ε. Indeed, in view of an early detection application of microwave imaging, a characterization of the performances in a low-contrast scenario is essential. In this section, we show the results obtained over reconstructed images (through IMUSIC, WB and ILOG algorithm) and compared with the mean value of that specific feature measured on every single-frequency reconstructions over the selected frequency range. Also, the results obtained from simulated datasets are shown as benchmark.

According to Mie Theory (Appendix B) results, if the linear dimension of the target is set and the wavelength of the incoming wave lowers, or viceversa linear dimension raises at a fixed wavelength, the scattering efficiency doesn't grow indefinitely. To put it in another way, the contrast, that depends in some way on the scattering cross section of the target, grows with a certain slope untill it reaches a plateau. In this range, SMR follows a pecular behaviour. Indeed, it tends to fluctuate around a specific value so that growing the scatterer size parameter may produce a decrease of the contrast (Figure 5.12). Scattering cross section depends on the linear dimensions of the target, and on its dielectric parameter aswell, so this effect occours also when the dielectric parameter grows.

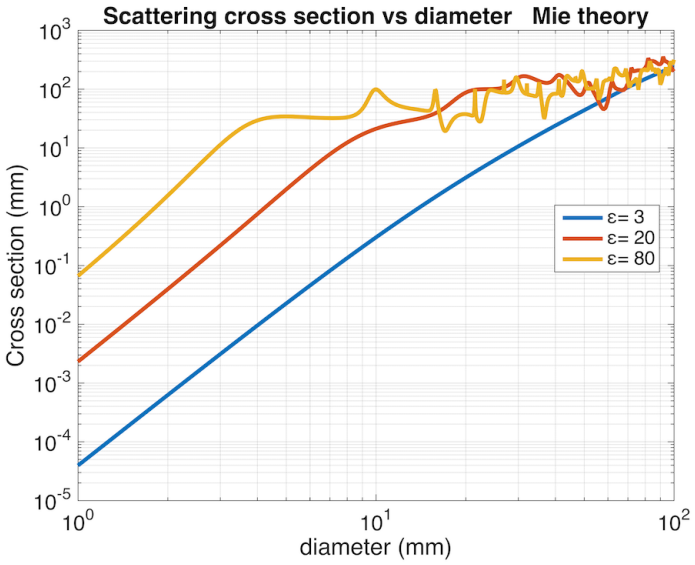

Figure 5.12: Scattering cross section of infinite cylinder target as a function of its diameter simulated for three different values of dielectric properies. The incident wave is characterized by a frequency equals to 2.5GHz and propagates in a medium of $\varepsilon = 2.5$.

Figure 5.13 shows the evolution of SMR as a function of ε. In these trends, three main behaviour are observable. The first one, that is notable in the first data points in Figure 5.13a, b, is the almost complete absence of contrast, indeed the signal doesn't react to changes in the dielectric parameter of the target. Also, the smaller the scatterer is, the more relevant this effect is, because the slope shifts to left as the diameter of the scatterer grows. Secondly, there is a range of ε values in which SMR increases with almost linear rate. Finally, for high value of permittivity, SMR starts bouncing around a certain value, and the amplitude of these oscillations decrease as ε grows (Figure 5.13 b, c).

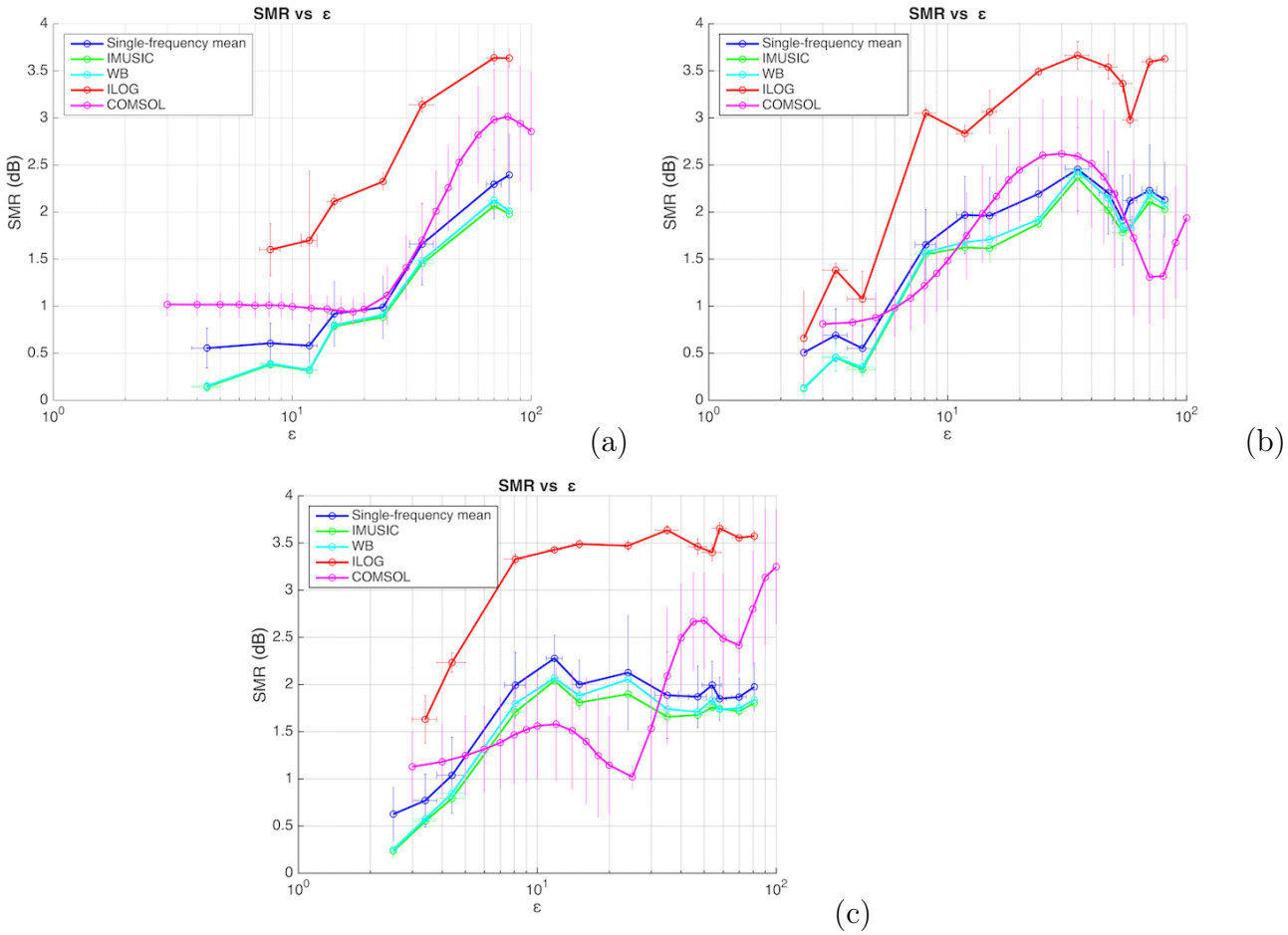

Figure 5.13: Evolution of the contrast varying ε for the (a) 5mm, (b) 10mm, (c) 16mm diameter scatterer. In a,b,c, the blue line is computed as mean and variance of the SMR corresponding to every single frequency reconstructions, whereas cyan and green line are calculated as mean and variance of the three WB and IMUSIC reconstructions performed for every measurement, over the 2.5-3.2GHz range spanned by 71 intervals. The magenta line is calculated as mean and variance of the SMR over data simulated over 5 frequencies (2.5, 2.6, 2.7, 2.8, 2.9 GHz). In (a) and (c) the first ILOG point is missing due to a numerical error.

Previous observations hold for every datasets shown in the figure. Their trends are very similar, even if the simulaed set (COMSOL) shows a more volatile behaviour, probably beacuse the mean was calculated over a few frequencies. Also, we can notice that IMUSIC and WB multi-frequency recombinations are not able to enhance the mean-contrast of the signal, at least with respect of the neighborhood where SMR is calculated. On the other hand, ILOG recombinations always show a large improvements of the contrast. Indeed, ILOG algorithm is able to expand the dynamic of the image, strongly stretching as if the high peaks were strongly stretched and leads

to an high contrast image.

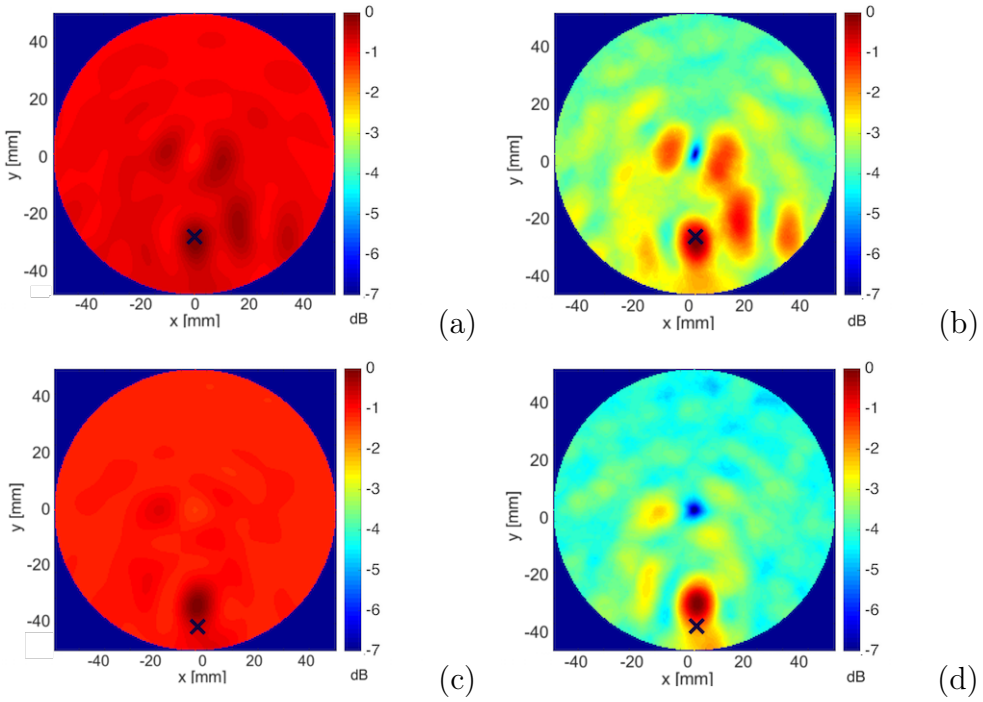

Figure 5.14: (a) IMUSIC and (b) ILOG reconstruction for 10mm diameter scatterer filled with $\varepsilon = 4.4$. (c) IMUSIC and (d) ILOG reconstruction for 5mm diameter scatterer filled with $\varepsilon = 8.1$. The cross represents the correct location of the scatterer. The reconstructions were sperformed on the optimal frequency range. The medium is charaterized by $\varepsilon = 2.5$.

In Figure 5.14 some reconstructions executed though ILOG and IMUSIC algorithm are shown. From the comparisons between ILOG and IMUSIC performances in low contrast scenario, it is possible to see that the expansion of dynamic range carried out by ILOG algorithm. For every couple of images, it is clearly observable that the "topology" is the same, indeed the principal maximum and other pleatings are located in the same areas, but what happens is that in ILOG reconstructions the background has a lower intensity than in IMUSIC ones. In other words, the information obtained from both the reconstructions is the same, but ILOG drastically lowers low signal. Also, in Figure 5.14b,d a small blue area is visible exactly in the center of the image. It is due to the preprocessing operations, in which a mean value filter is applied to erase all the centro-symmetric components, and it is visible in ILOG reconstructions thank to the lowering effect typical of this algorithm.

Let's recall what previously shown about the behaviour of SMR as a function of the dielectric constant. From our data, we observed a trend compatible with Mie

theory. In addition to this, we have performed the study of the dependence between SMR and the scatterer diameter, for different values of ε (Figure 5.15). We don't have many experimental points to describe the behaviour in a wide range of dimensions, but those data are enough to see that, when ε is small, SMR grows with the diameter, but when ε raises a sort of upper limit is reached.

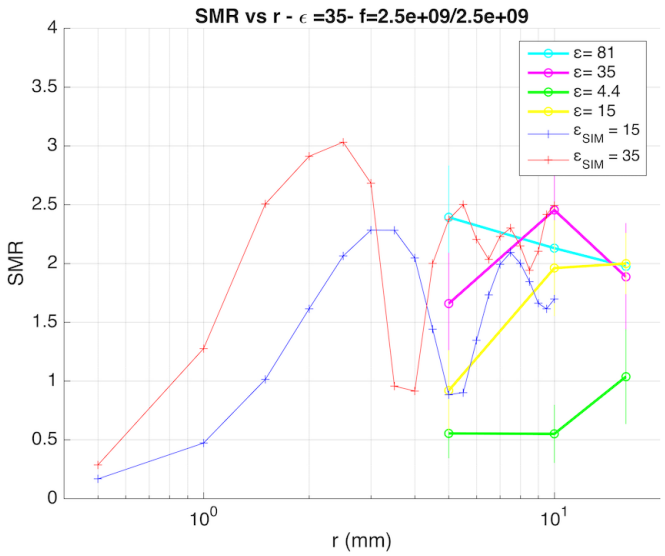

(d)

Figure 5.15: Evolution of the contrast as a function of the diameter, varying ε. Data are computed as mean and variance of the SMR corresponding to every single frequency reconstructions. here it is shown the comparison between real and simulated data.

Contrast feature have been studied so far. It was shown that SMR increases as the diameter or dielectric constant grow, until a plateau is reached. Experimental results were in accordance with simulated results, and the ILOG performances were shown and compared with other reconstruction algorithm. A further step was carried out to investigate the influence of the size.

Multi-frequency approach is useful to reduce artefacts because each single-frequency signal has a low weight on the final image, so that delocalizated targets will be neglected if they don't cluster in specific areas. In other words, the final image is the recombination of every single frequency contributions, and since single-frequency maximum location tends to correspond to the scatterer position, only the correct reconstructions will survive after the multi-frequency recombination. Hence, we would say that multi-frequency images are more stable than single-frequency ones.

As we saw in §5.1.1, maxima belonging to single-frequency images tend to shift their position according to the corresponding frequency. In the optimal working range

this effect is not strong as in the full frequency range, but it still occurs. As result of this behaviour, the main peak of the multi-frequency reconstruction tends to be wider than in single frequency image.

This effect is shown in Figure 5.16, through the study of the behaviour of $FWHM_{\rho,\phi}$ as a function of ε. The green, cyan and red line are almost everywhere higher than the blue line, so that we can state that IMUSIC, WB and ILOG actually spread out the signal. This effect is even more evident in ILOG reconstructions. Indeed, since the clutter surrounding the signal is very compressed, the peak height increases, producing an high FWHM.

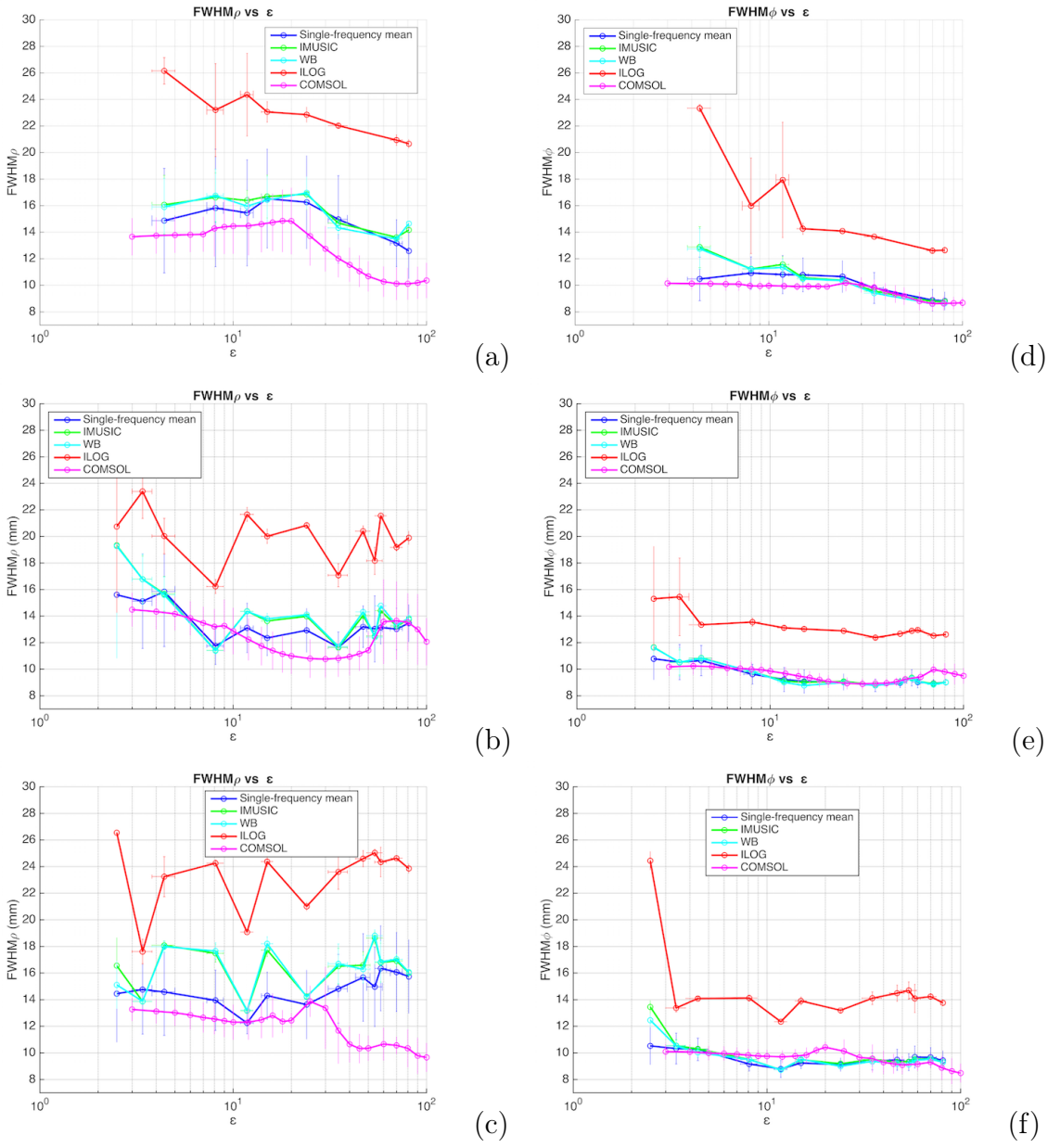

Figure 5.16: Evolution of $FWHM_\rho$ [mm] and $FWHM_\phi$ [mm] varying the target permittivity for the (a, d) 5mm, (b, e)10mm and (c, f) 16mm diameter scatterer. $FWHM_\rho$ appears to be lower than $FWHM_\phi$.

One of main drawbacks of microwave imaging is that the spatial resolution is low due to the use of high wavelenghts radiation. Small targets can be detected but the reconstructed spatial dimensions are not always reliable. Indeed, $FWHM_\rho$ tends to a realistic value only for the bigger scatterer (Figure 5.16c) reconstructed by IMUSIC and WB. Also, it slightly tends to lower values for the 10mm diameter scatterer (Figure 5.16b) but there is no further decrease for the smaller target. Moreover, no

trend is found along the angular component of the peak.

5.3 Heterogeneous medium

Heterogeneous medium are a typical scenario to stress reconstruction techniques. Indeed, so far it has been shown that this experimental set-up is able to detect both small and low-contrast targets in an homogeneus background. This ideal scenario doesn't find a clinical application in breast imaging, since breast cancer is usually located in fibroglandular tissue, which is characterized by slightly inferior dielectric constants than tumor tissue. In order to study the joint ability of the acquisition system and the reconstruction algorithm, an heterogeneous 50mm diameter phantom prototype was created (§4.1), which allows to insert the 16mm diameter scatter inside the fibroglandular tissue, that in turn is inserted in the adipose tissue. We filled the target with a solution whose dielectric properties was similar to the breast ones, and for every set of measurements the fibroglandular tissue was filled with a different emulsion of increasing dielectric constant (Table 5.2). Note that the heterogeneous medium was simulated with an homogeneous fibroglandular phantom, that is inside of it no further structures or inhomogeneities are present. Also, even if the reasons of the following statement will appear clearer further, it is important to underline that this phantom was developed in a specific way to avoid that the center of the target coincided with the center of the phantom itself (Figure 5.17b).

ε	$\Delta\varepsilon$
5.6	0.1
6.7	0.1
8	0.1
9.5	0.1

Table 5.2: Dielectric constants evaluations of the emulsions of seed-oil and acetone to simulate the fibroglandular tissue. The scatterer was filled with a solution composed of 90% glycerol 10% water, that is completely stable and characterized by $\varepsilon = 54$. We assumed those values as constant over the considered frequency range.

The measurements were performed in three different configurations. For every value of the fibroglandular tissue phantom, the acquisition was carried out with the scatterer both inside and outside the heterogeneous medium, and also without the scatterer at all (Figure 5.17). In light of previous results, the reconstructions were performed over the frequency range included between 2.5 and 3.2 GHz.

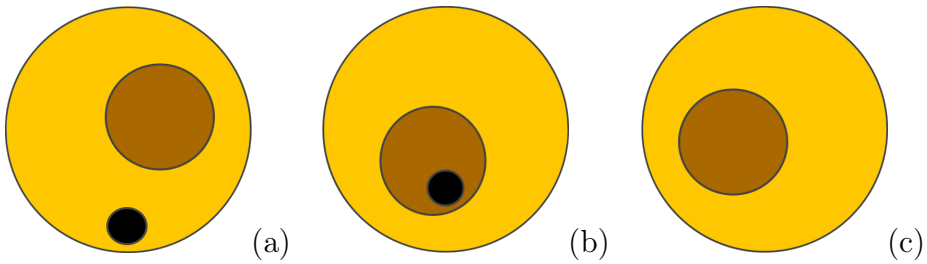

Figure 5.17: Different configurations of the measurements conditions. The scatterer is (a) outside and (b)inside the fibroglandular tissue. (c) The scatterer is not present at all. The brown and light brown colors represents seed oil and the emulsion of oil and acetone used to fill the fibroglandular phantom. The black circle stands for the target position. Note that the fibroglandular tissue doesn't touch the skinlayer, whereas in (a) tumor and fibroglandular phantoms touch eachother. The diameter of the fibroblandular phantom equals to 45mm, that is the half of the breast phantom diameter.

Three measurements were carried out for every configuration and for every fibroglandular tissue simulation. In order to investigate the correctness of the reconstruction, SMR and FWHM were calculated in a region surrounding the maximum, though automatic detection, and compared with the SMR and FWHM in the area where the scatterer is know to be located. This comparison is essential because we expect that, being the fibrobladular phantom a considerable presence in the scattering scenario, it could have a strong influence in the reconstructed image up to produce a signal higher than the scatterer itself.

As first configuration was considered the scenario where the scatterer is inserted directly in the "adipose" tissue (5.17a). The evolution of SMR as a function of the fibroglandular medium is shown in Figure 5.18. We observe a relatively low SMR values for IMUSIC and WB reconstructions, not significantly different from the simple single-frequency mean, whereas the ILOG reconstructions show very high SMR values, in accord with the results of previous analysis.

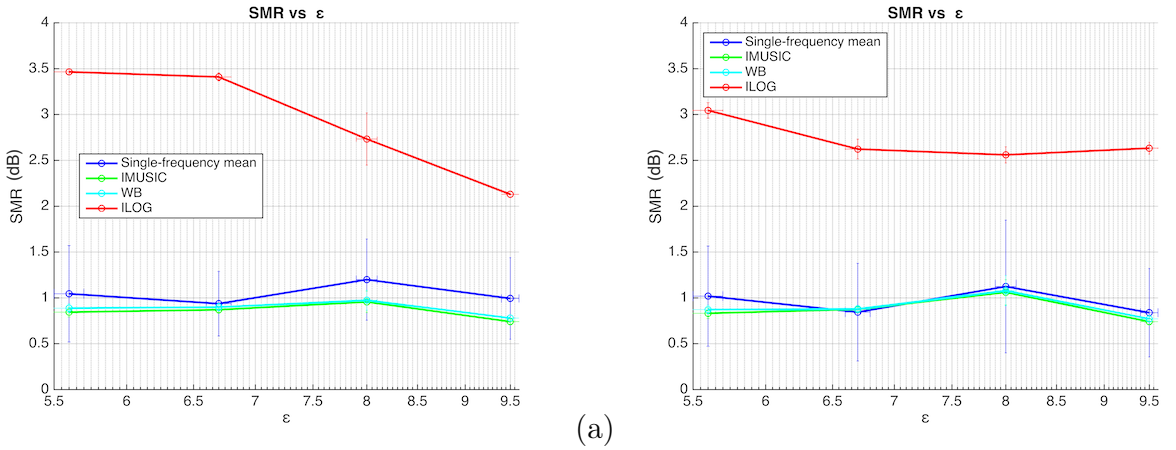

Figure 5.18: SMR of the reconstructed images as a function of the unhomogeneity permittivity in (a) the area surrounding the maximum value of the pseudospectrum, and (b) where the scatterer is know to be positioned. The target was characterized by $\varepsilon = 54$.

From the comparison between these two plots, it clearly appears that the signal intensty decreases as the dielectric properties of the fibrloglandular phantom increase. At this stage, we expect two possible scenarions, which are the presence of a very delocalized signal or the rising of clutter in the fibroglandular phantom area. We will see that both these two scenarions will show up theirself, according to the configuration of the scattering domain.

Observing the reconstructed images through IMUSIC and ILOG multifrequency algorithm, we note that the second scenario has occoured in both cases. Figure 5.19 gives a qualitative visualization of this phenomenon. Also, we can observe that both algorithms reconstruct correctly the scattering scenario showing a comparable image topology, and as expected the dynamic range of ILOG reconstructions are much higher than IMUSIC ones. In spite of the qualitative goodness of these reconstructions, in Figure 5.19a, c it is observable a slight delocalization of the target which produces a decrease of the SMR values in the actual target position, justifying the differeces between SMR trends shown in Figure 5.18.

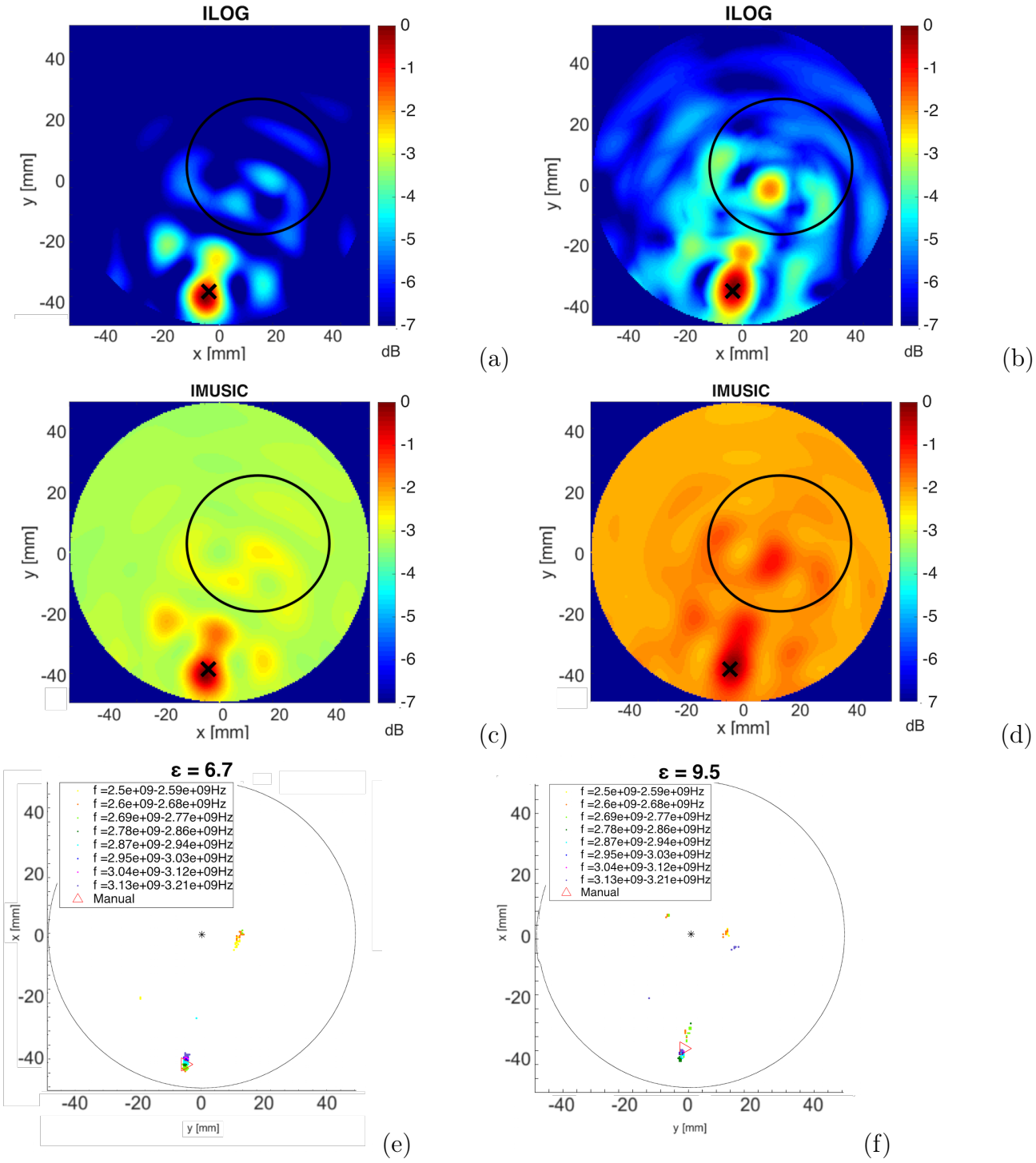

Figure 5.19: Reconstruction of multi-frequency images exploiting IMUSIC and ILOG algorithm. The fibroglandular phantom is filled with an emulsion characterized by (a,b) $\varepsilon = 6.7$ and (c,d) $\varepsilon = 9.5$. The black cross and circle stand for the actual target and fibroglandular phantom positions. In both cases the scatterer is correctly reconstructed, and the areas surrounding the fibroglandular phantom show an increasing presence of clutter, as expected. (e) and (f) show the distribution of the maximum values of the single-frequency pseudospectra.

Figure 5.19e, f show the maximum distributions of the single frequency reconstructions. It clearly appears that in Figure 5.19f maxima tend to group in spread out clusters more than in Figure 5.19e, that is growing dielectric properties of the fibroglandular tissue produces a wider distribution of single-frequency pseudospectrum maxima, and also the production of small artefacts. As result of the single-frequency contributes recombination, the peak in the multifrequency reconstructions is smaller and wider, and the SMR calculated over it will be smaller than over a thinner and higher peak (Figure 5.20).

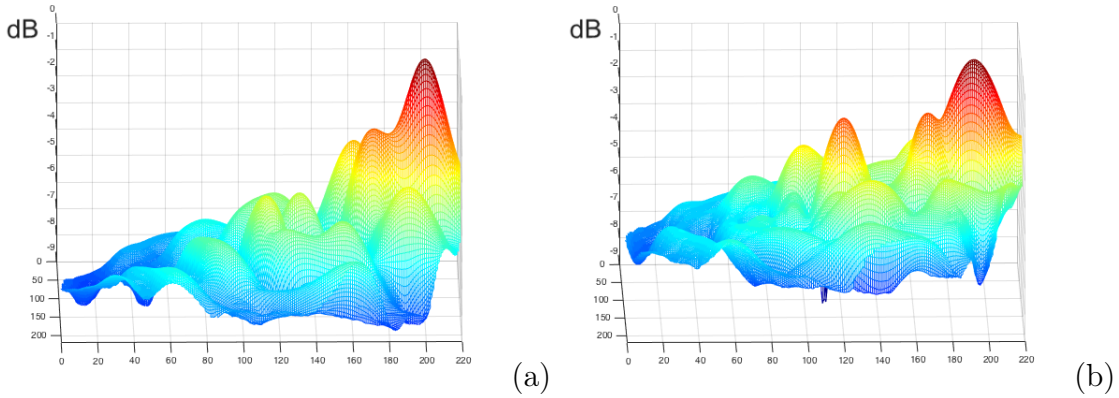

(a) (b)

Figure 5.20: Qualitative visualization of ILOG pseudospectrum reconstructions showed in Figure 5.19a, b. The peak corresponding to the fibroglandular phantom characterized by $\varepsilon = 6.7$ (a) is slimmer than (b), in which the phantom is filled with a $\varepsilon = 9.5$ emulsion.

A further proof of this behaviour is given in Figure 5.21, where it is shown that the FWHM of the peak tends to grow with the dielectric properites of the fibroglandular phantom along the radial directon. FWHM computed over ILOG reconstructions shows a slight increase, meaning that this algorithm always reduces the clutter in the area surrounding the maximum and perform a well shaped peak, whereas WB and IMUSIC are not able to reduce the spreadness of the single-frequency maxima.

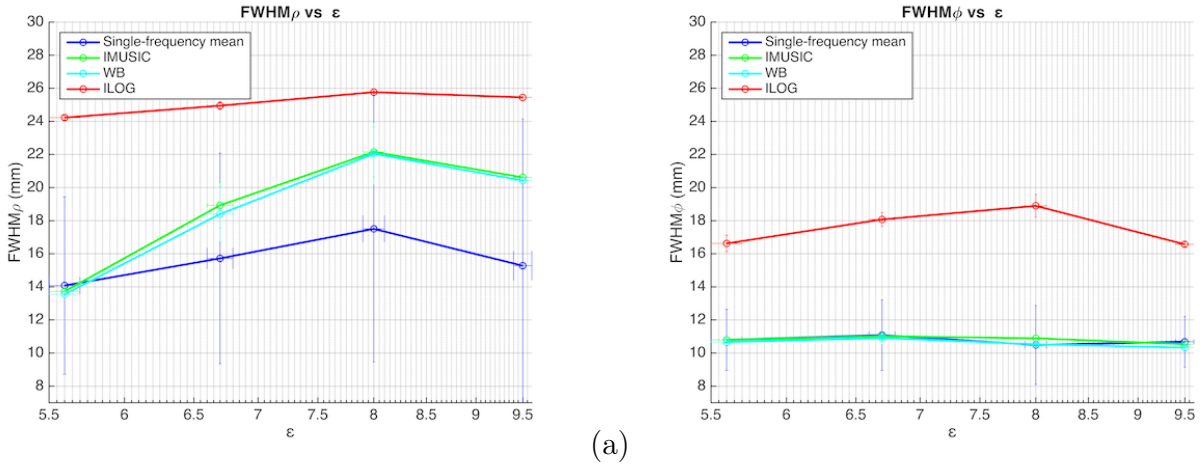

(a) (b)

Figure 5.21: (a) Radial and (b) angular component of FWHM of the reconstructed images as a function of fibroglandular ε. Values were computed in the area surrounding the maximum value of the pseudospectrum.

We have seen so far that the reconstructed image degrades as the dielectric properties of the fibroglandular phantom increases. In spite of this, the reconstructions produce a good target localization even in presence of a massive external unhomogeneity, that, in the worst faced case, is translated in the pseudospectrum as a secondary peak.

Now consider the second scattering scenario, in which the target is inserted in the fibroglandular tissue. As before, SMR was evaluated in the areas surrounding both the maximum pseudospectrum value and the scatterer position manually imposed.

Figure 5.22a shows the SMR calculated on the maximum value of the pseudospectra obtained through different reconstruction algorithms. It appears that the value of this feature is not strongly influenced by the dielectric properties of the fibroglandular tissue. Also, IMUSIC, WB and ILOG give quite similar results in terms of SMR as if the area surrounding the main pseudospectrum peak were only slightly affected by clutter presence. Now, consider Figure 5.22b, where the values of SMR calculated on a specific area are shown. Again, we observe that ILOG reconstruction performances are clearly better than IMUSIC and WB ones,. Also, SMR computed in the actual target location is slightly higher than the one computed in the area surrounding the maximum of the pseudospectrua, at least for these computed through ILOG algorithm. This evidence suggests us that, even if the target is not represented by the highest signal on the pseudospectrum, it produces the best contribution in terms of cleaness of the signal. In other words, the main peak, that is produced by the fibroglandular scatterer, is affected by an higher level of clutter in comparison to

the peak corresponding to the actual target.

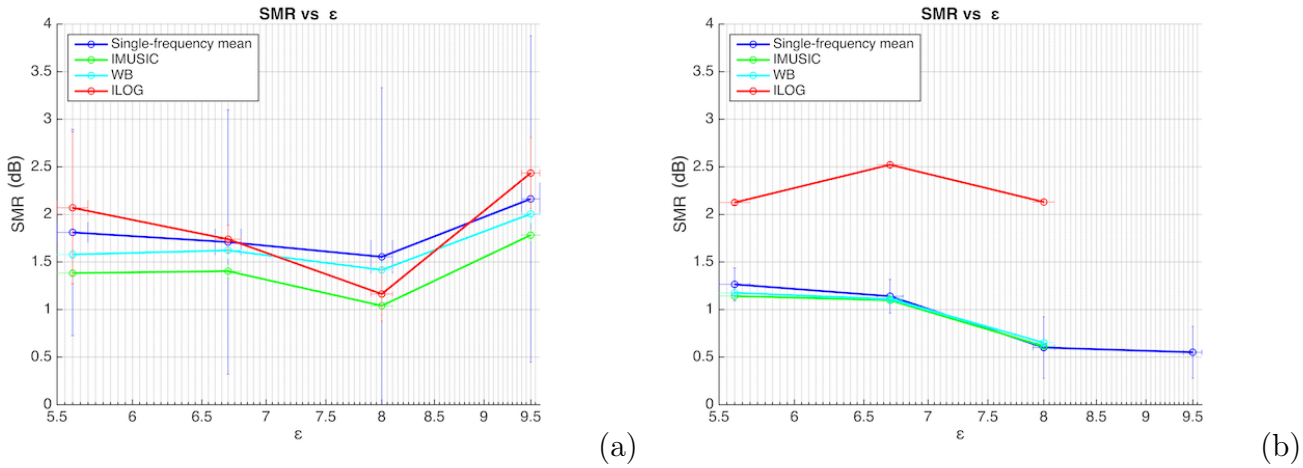

Figure 5.22: SMR of the reconstructed images as a function of fibroglandular ε in (a) the are surrounding the maximum value of the pseudospectrum, and (b) where the scatterer is know to be positioned. The target is inserted inside the "adipose" tissue. In (b), the last point of IMUSIC, WB and ILOG lines are missing because no signal was found in the imposed area in none of the three measurements performed, leading a NaN value. We observe that in (a) SMR is given by the unhomogeneity. This explain why for $\varepsilon = 9.5$ SMR grows in (a) and disappears in (b).

Comparing the SMR evolution as a function of ε with the final ILOG and IIMUSIC multifrequency reconstructions, we can conclude that the numerical results are compatible with the qualitative evaluation of the images. Indeed, we observe that the main peak always corresponds to a big artefact produced by the fibroglandular phantom, and also, expecially in IMUSIC reconstructions, the seconday peak that corresponds to the target drows in the background as the fibroglandular dielectric constant grows, till it completely disappears. This happening justifies the lack of the last value of SMR computed in the area surrounding the target position, and also it produces a decrease of the clutter surrounding the maximum given by the fibroglandular phantom, as proven by the SMR increase for the last two values of ε.

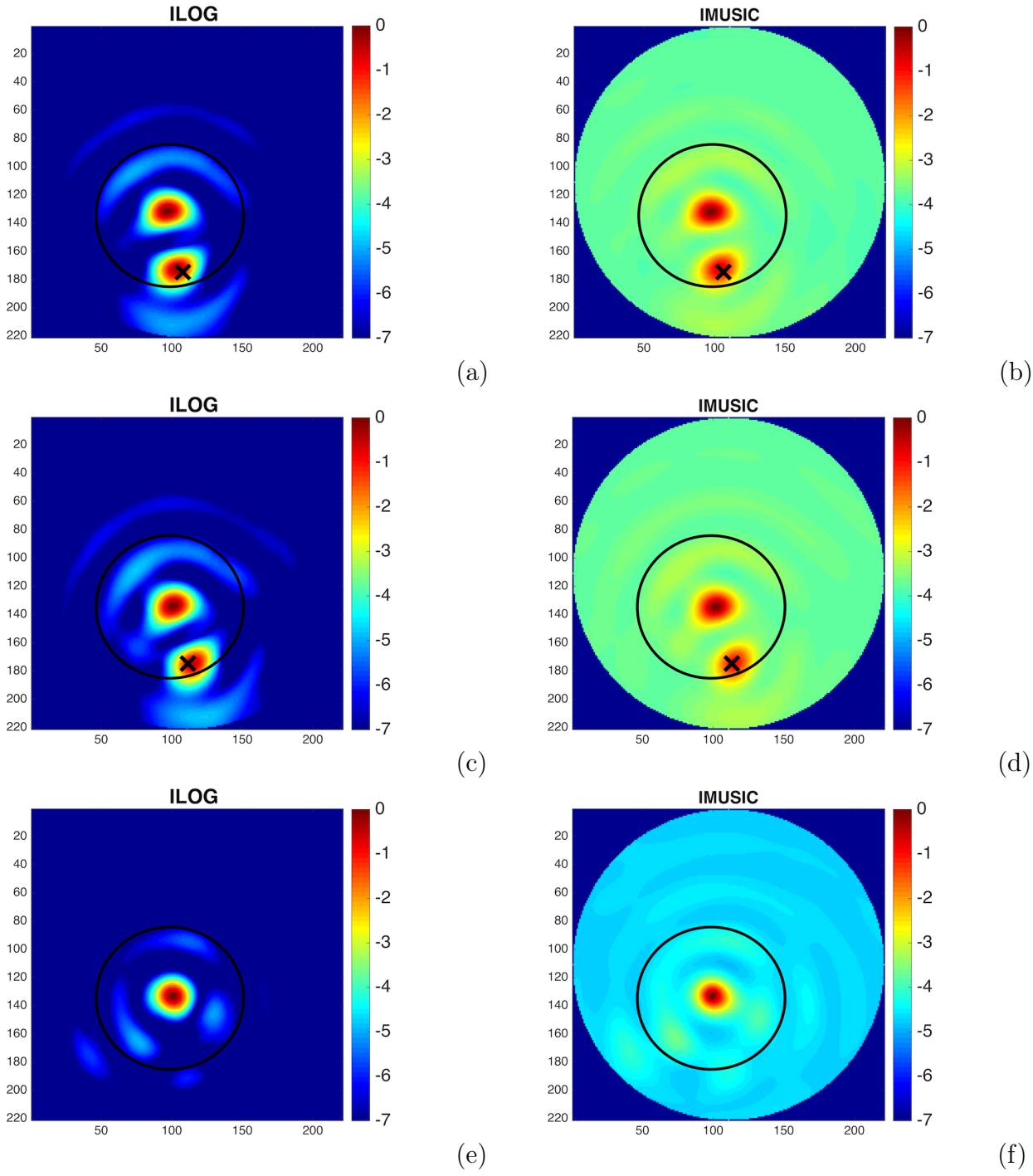

Figure 5.23: Reconstruction of multi-frequency images exploiting IMUSIC and ILOG algorithm. The fibroglandular phantom is filled with an emulsion characterized by (a,b) $\varepsilon = 6.7$, (c,d) $\varepsilon = 8$ and (e,f) $\varepsilon = 9.5$. The black cross and circle stand for the actual target and fibroglandular phantom positions. In all those cases, the main peak is given by the fibroglandular phantom. Also, a secondary peak is present in (a,b,c,d) that is correctly localed in the tumor position, but in (e,f) it completely disappears.

In this scattering configuration, we have obtained results very different than those achievedin the previous one. Indeed, a sudden and dramatic degradation of the reconstructed image has occured increasing the dielectric properties of the fibroglandular phantom, leading to the only reconstruction of the phantom itself. Also, in this configuration the fibroglandular phantom produces different effects, where the increase of its dielectric properties was traduced as an increase of the clutter intensity. Now, it arises as the principal component inside the scattering scenario, where concentric contributions are created by multiple scattering effects between the fibroglandular phantom and the scatterer itself, and also confer the idea of the phantom structure. Our reconstruction algorithm is not able to analyze the mutual interation between different scatterers, hence it completely fails the tumor reconstruction in the most extreme condition in which it was tested (Figure 5.23e, f)

Finally, in the third scattering scenario we have performed measurements without the scatterer in order to study the influence of the fibroglandular tissue over the reconstructed image. Since we are using TR-MUSIC algorithm in monostatic approach, we expect to find a punctiform signal even if the fibroglandular phantom has broad spatial dimensions. As in the previous cases, we have studied the SMR through automatic research and compared with the value measured in the area where the fibroglandular phantom is located. In this area we expect to find most of the signal because, as previously mentioned, the scatterer is missing. Observing Figure 5.24a we notice that SMR calculated over ILOG reconstructions slightly increases, whereas no significant trend is shown in IMUSIC and WB reconstructions. Also, these SMR values are identically equal to SMR computed in the barycenter of the fibroglandular phantom. In the light of this, we expect to find an high and punctiform-like signal in an almost clutter-free background, expecially for ILOG reconstructions, but no significant evolution is expected from variation of dielectric properties of fibroglandular phantom.

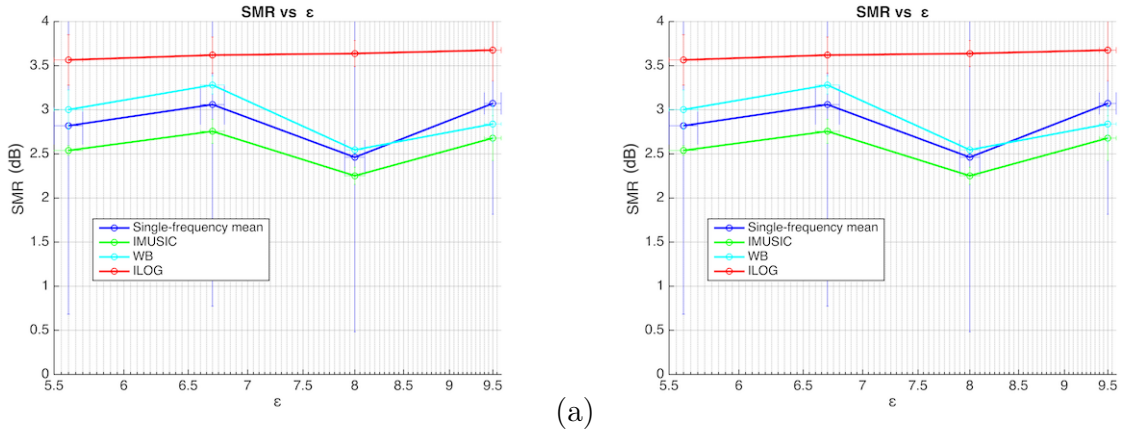

Figure 5.24: SMR of the reconstructed images as a function of fibroglandular ε in the area surrounding the maximum value of the pseudospectrum. This high level of SNR is given by the fibroblandular phantom since the scatterer is missing.

Analyzing the pseudospectrum reconstructed through ILOG and IMUSIC algorithm, we obtained a visual proof of what previously hypothesized. All the pseudospectra illustrated in Figure 5.25 show a very high and well defined peak inside the fibroglandular tissue. Also, exploiting the low-capability of IMUSIC algorithm to reduce clutter, a slight sign of the phantom boundary is shown here aswell. Note that the maximum localization in this scenario where the scatterer is missing is the same as in the last reconstruction performed on the previous scenario, i.e. in that case (Figure 5.23 e, f) the presence of the tumor was almost completely neglected, producing a simply increase of the clutter around the fibroglandular phantom.

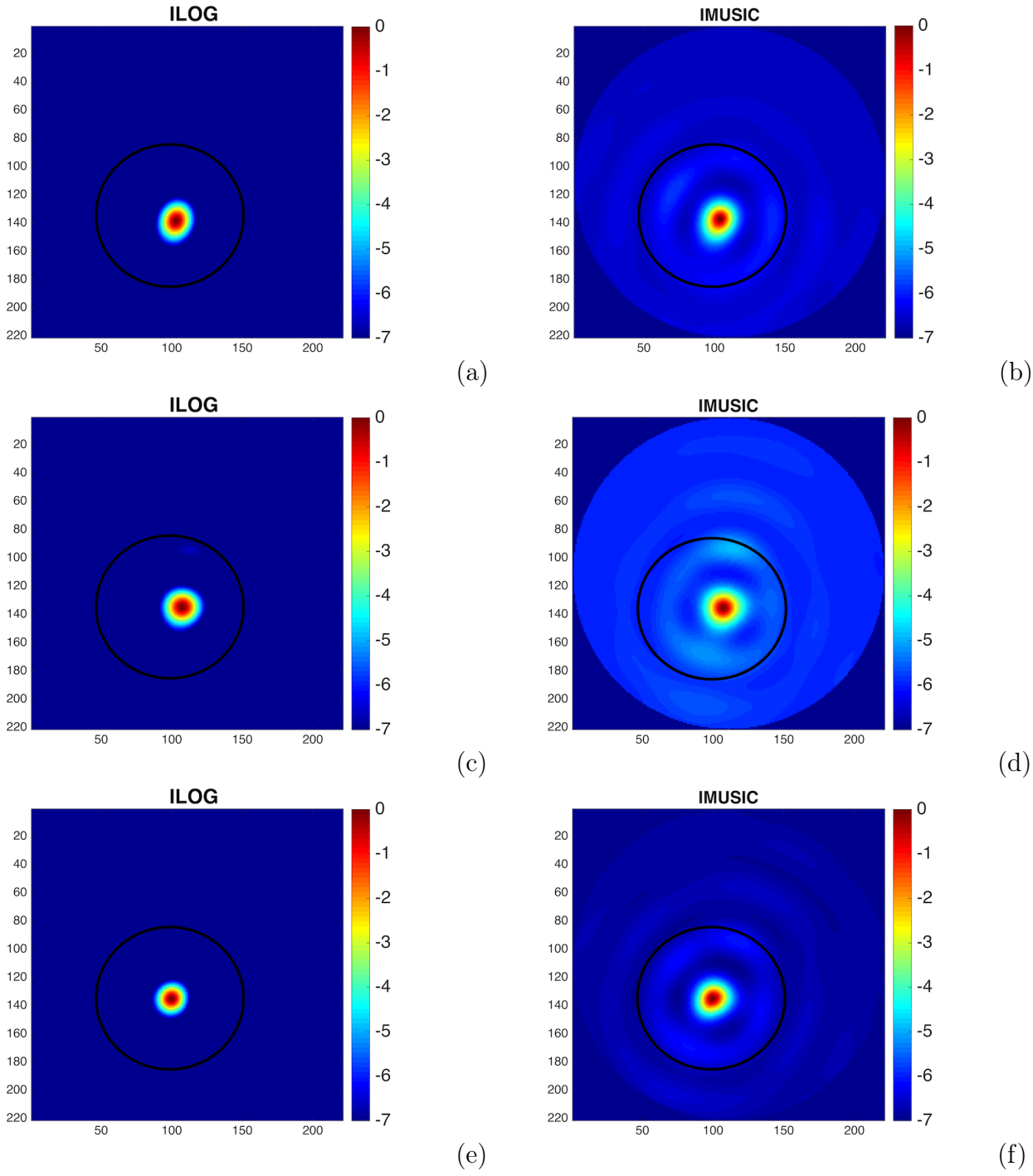

Figure 5.25: Reconstruction of multi-frequency images exploiting IMUSIC and ILOG algorithm. The fibroglandular phantom is filled with an emulsion characterized by (a,b) $\varepsilon = 6.7$, (c,d) $\varepsilon = 8$ and (e,f) $\varepsilon = 9.5$. As expected, only a tight peak produced by fibroglandular target is shown in these reconstruction. Also, phantom boundaries are slightly shown in IMUSIC reconstructions.

In addition to this, we computed spatial features aswell. As shown in the previ-

ous section, the radial component of FWHM is bigger the the angular one, but no significant dependence from dielectric properties of the fibroglandular phantom was found.

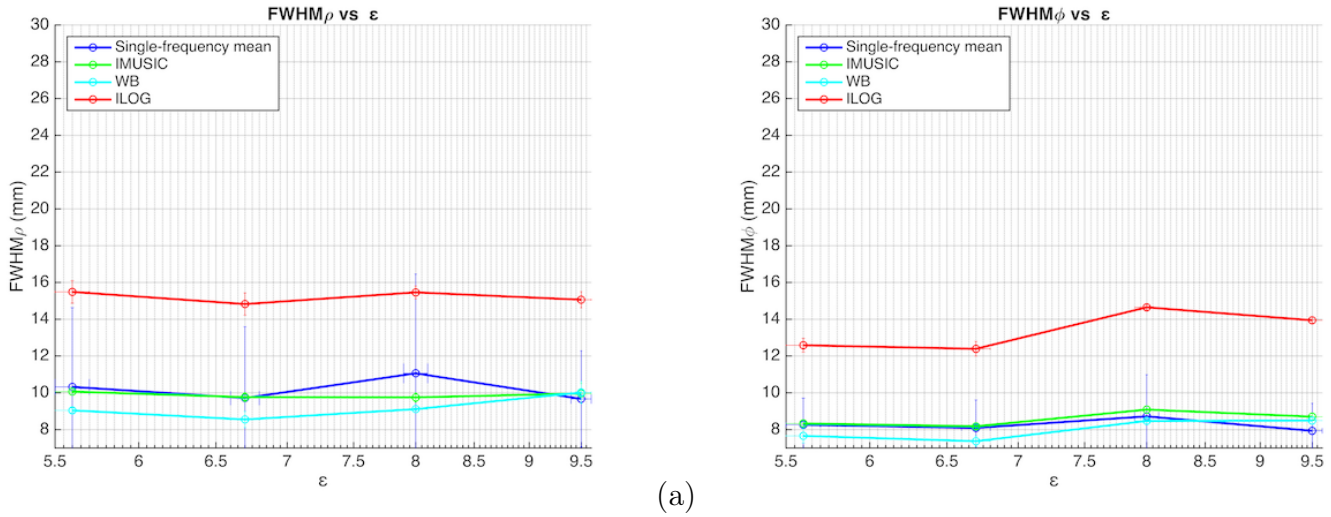

(a)

Figure 5.26: Radial and angular component of FWHM computed on the peak given by the fibroglandular phantom.

5.4 3D Reconstructions

In this final stage, some measurements were accomplished in order to study the behaviour of the acquisition system if the target is located out of the antenna plane. To do this, we performed different measurements fixing the finite dimensions scatterer at different depths (§4.1). Also, the imaging system was tested on both homogeneous and heterogeneous medium. In the first experiment we used GLASSBURGER, that is a low contrast scatterer suitable for homogeneous medium. In the second experiment we used PATROCLO, that is more appropriate than GLASSBURGER in an heterogeneous scenario since it is characterized by an higher dielectric permittivity.

The reconstructions of those datasets were performed though a reconstruction algorithm developed by the colleague Musca L. [57], that is able to execute 3D reconstruction emplying two different approaches. This algorithm is not the object of this work, hence only a qualitative description will be given and we will focus more on the results. The aim of this algorithm is to perform 3D reconstructions of a finite-dimension tumor, that was simulated by two different spherical-like scatterers.

In the previous measurements we employied an "infinite cylinder" scatterer, so that we had a sort of simmetry in respect to the antenna plane and, under this geo-

metrical assumpion, acquired signal was not affected by variations on the vertical axis (perpendiculart to the antenna plane). Now, we perform measurements at different distances from the antenna plane, so we need to take into account also the additional information along the heigth. As described in the §3.3, the signal vector, acquired at a precise heigth $h^{(a)}$, can be used to calculate the pseudospectrum at a specific frequency though the 2D-Green's propagator and TR-MUSIC algorithm. In this we obtain a single tomographic image given by the signal vector $\boldsymbol{S}(\omega, h_i^{(a)})$ corresponding to the heigh $h_i^{(a)}$. Repeating this method for different elevations, we obtain a set of tomographic images which can be used to infer the information along the heigth at discrete steps. The missing reconstructions associated to the intermediate volumes in between acquisition planes are derived by applying the cubic interpolation method to the available pseudospectra. This approach, called *Tomographic Superposition* (TS), is the 2D counterpart of the *Multi-Elevation* (ME) algorithm, which exploits the 3D Green's propagator for the infinitesimal dipole. This propagator allows to obtain the values out of the antenna plane through the calculus of the correlation between signal and monostatic signal vector for whichever point in the domain. This algorithm is able to reconstruct the whole imaging domain pseudspectrum with a single acquisition performed at a specific height. Data must be aquired at different antenna heights and, for each row of the signal matrix

$$\boldsymbol{S}(\omega) = \begin{bmatrix} \boldsymbol{S}(\omega, h_0^{(a)}) \\ \boldsymbol{S}(\omega, h_1^{(a)}) \\ \vdots \\ \boldsymbol{S}(\omega, h_N^{(a)}) \end{bmatrix} = \begin{bmatrix} S_{11}(\omega, h_0^{(a)}) & S_{22}(\omega, h_0^{(a)}) & \dots & S_{2020}(\omega, h_0^{(a)}) \\ S_{11}(\omega, h_1^{(a)}) & S_{22}(\omega, h_1^{(a)}) & \dots & S_{2020}(\omega, h_1^{(a)}) \\ \vdots & \vdots & \ddots & \vdots \\ S_{11}(\omega, h_N^{(a)}) & S_{22}(\omega, h_N^{(a)}) & \dots & S_{2020}(\omega, h_N^{(a)}) \end{bmatrix} \tag{5.2}$$

a mono-elevation volumetric image of the breast has to be reconstructed with 3D-propagator. Before attempting reconstruction, the signal matrix rows are filtered with the average subtraction filter.

In this stage we encountered a significant issue given by the selection of the optimal frequencies. 3D reconstructions can be still performed through a multi-frequency approach but it is necessary to carefully select a few optimal frequencies, since reconstructing pseudospectra at all the available frequencies would be too expencive from a computational point of view. The frequency range selected in the previous sections is still too populated, so we had to choose manually the best ones. In order to be conservative and use all the possible significan signal we have extended the working

range from 2 to 3.5GHz. Also, according to what previously shown, SMR is not always connectd to a well reconstructed image, so the selection of the best frequencies cannot be based only upon high SMR values. For this reason we developed an user interface able to show the frequencies associated to the highest SMR values in bidimensional pseudospectrum images, and to perform the reconstruction only at those frequencies whose maximum belong to a ROI selected by the user (Figure 5.27).

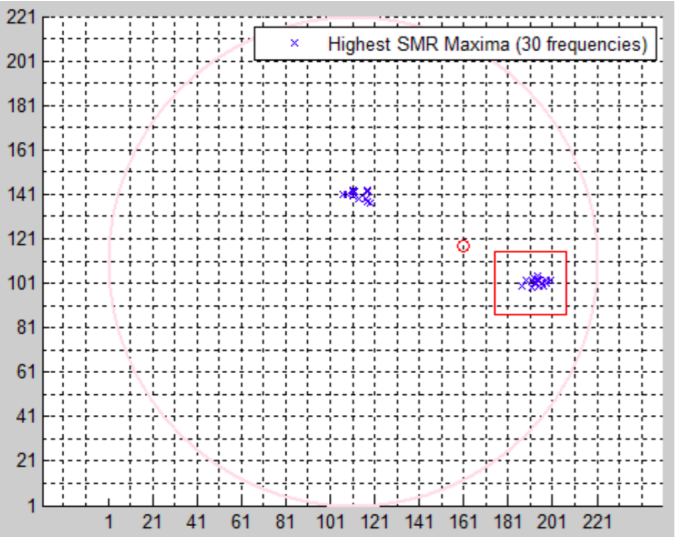

Figure 5.27: Frequency selection interface in the 2-2.5 GHz range. The red rectangle show the manual selection of a specific custer, while the red dot represents the clustering center of the maxima.

This way, we choose ex-post the few frequencies which both correspond to high SMR values and well localized reconstructions. Of course, this tool is very useful for our purposes, whereas for real appliacations in which the imaging domain is unknown, an algorythm for automatic tumor detection must be implemented.

Another considerable problem of 3D measurements is given by the finite scatterer dimension , that has to be acquired through multi-elevation aquisition method (i.e. perform the measurements at different depths). Since the antenna is fixed in a certain position, we have to immerse the tumor phantom inside the breast at different depths and then calculate the corresponding elevation from the antenna plane. We carefully executed this assesment because, if an error occurs in this stage, the reconstructed images will shown a delocalized object along the vertical axis. A source of delocalization could also occurs due to the rotational motion of the breast phantom, since the scatterer would swing for a long time after the rotation is executed. The measurements were performed in a viscous medium (i.e. seed oil or a seed-oil based

emulsion), so this effect should be neglectable, and also we waited 20 seconds between the end of the motion and the signal acquisition.

5.4.1 Homogeneous medium reconstructions

The first multi-elevation measurement session was performed in an homogeneous medium using the GLASSBURGER ($\varepsilon = 5$) as a finite dimension scatterer, that was inserted in the 16mm diameter external hole. The depth immersions have been estimed at $h_0 = -50$mm, $h_1 = -25$mm, $h_2 = 0$mm, $h_3 = 25$mm and $h_4 = 50$mm from the antenna plane. These measures were perfomes on the nylon string with a ruler, so the error is of the order of 1mm.

Through the user interface, we selected the frequencies which provide the best SMR value in the scattering plane evaluationg all the clustering maps deriving from three independent acquisition sets for every height. The result of this analysis leads us to the employment of only four frequencies during the reconstruction process (2.1, 2.3, 2.5, 3.0 GHz). We have approximated the frequency value at the first decimal digit, even if the real values have a much higher precision. We have exploited the exact frequency value during reconstruction at each elevation.

At this stage, we have performed the reconstructions through tomographic superposition and multi-elevation method over the five selected height. We executed single frequency, WB and ILOG reconstructions (Figure 5.28, 5.29).

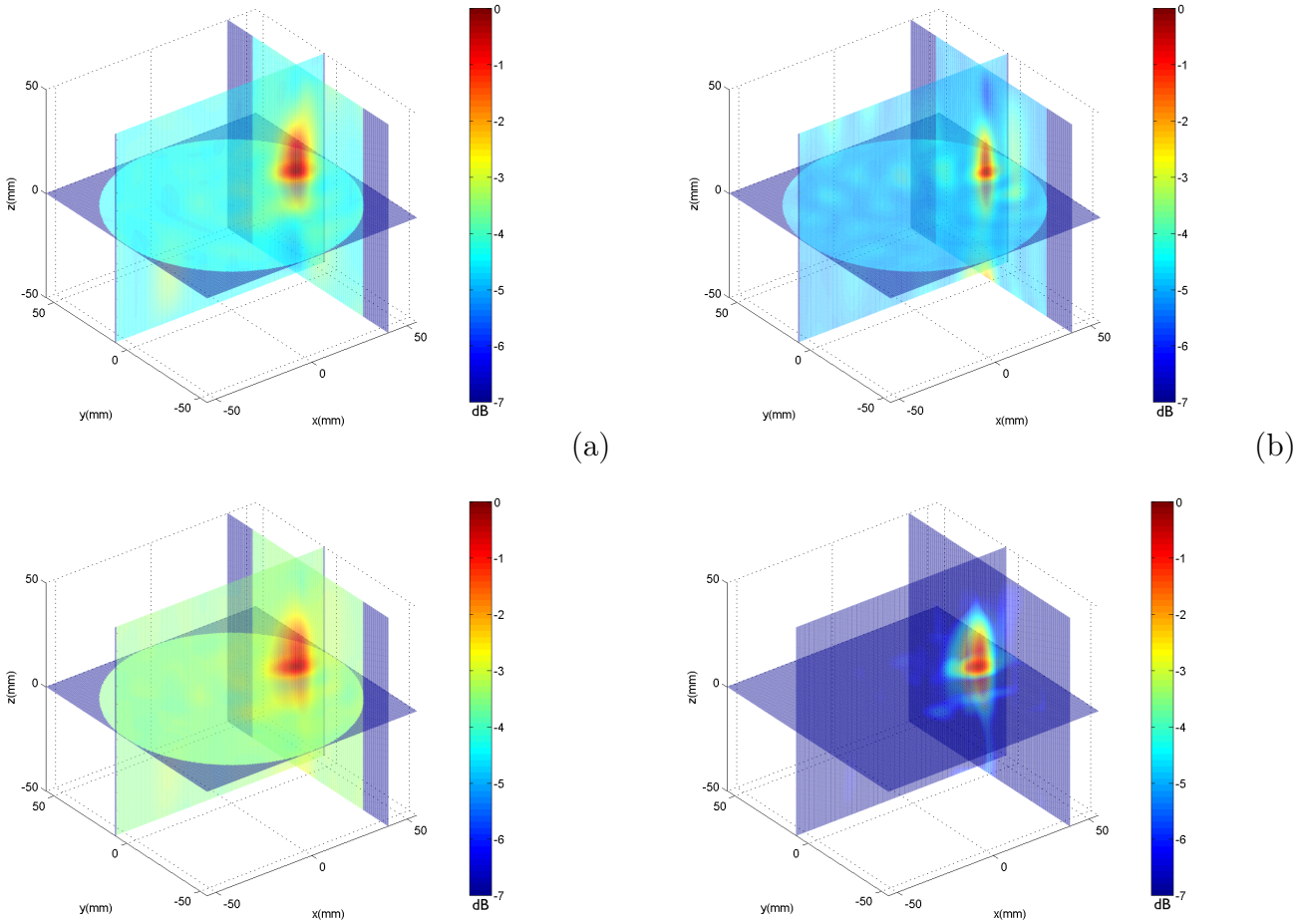

Figure 5.28: Samples of orhogonal-plane view of the tomographic superposition reconstruction method in the homogeneous breast-phantom with GLASSBURGER phantom. The reconstructions correspond to (a) 2.1GHz and (b) 3GHz. (d) and (e) are respectively WB and ILOG reconstructions.

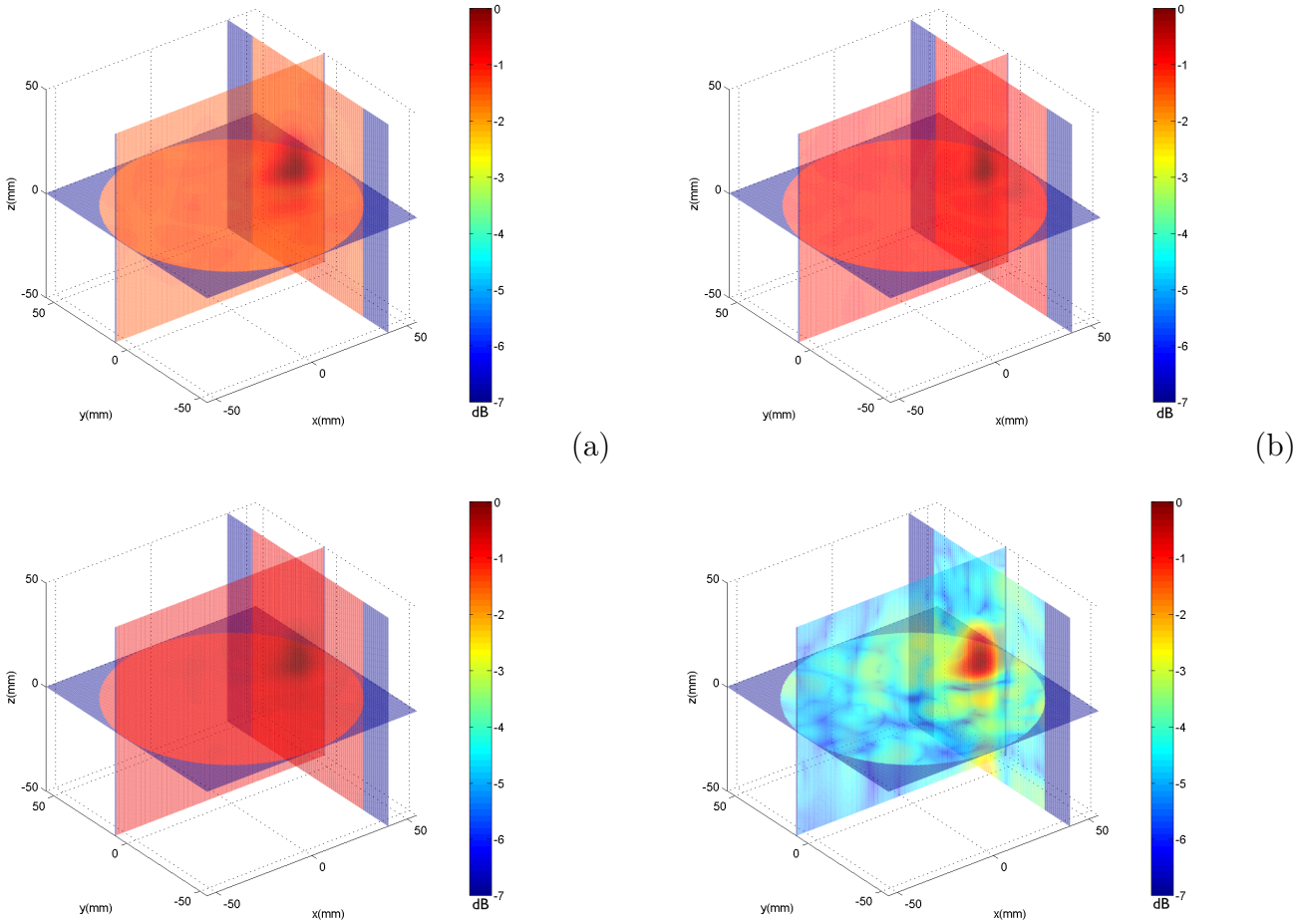

Figure 5.29: Samples of orhogonal-plane view of the multi-elevation reconstruction method in the homogeneous breast-phantom with GLASSBURGER phantom. The reconstructions correspond to (a) 2.1GHz and (b) 3GHz. (d) and (e) are respectively WB and ILOG reconstructions.

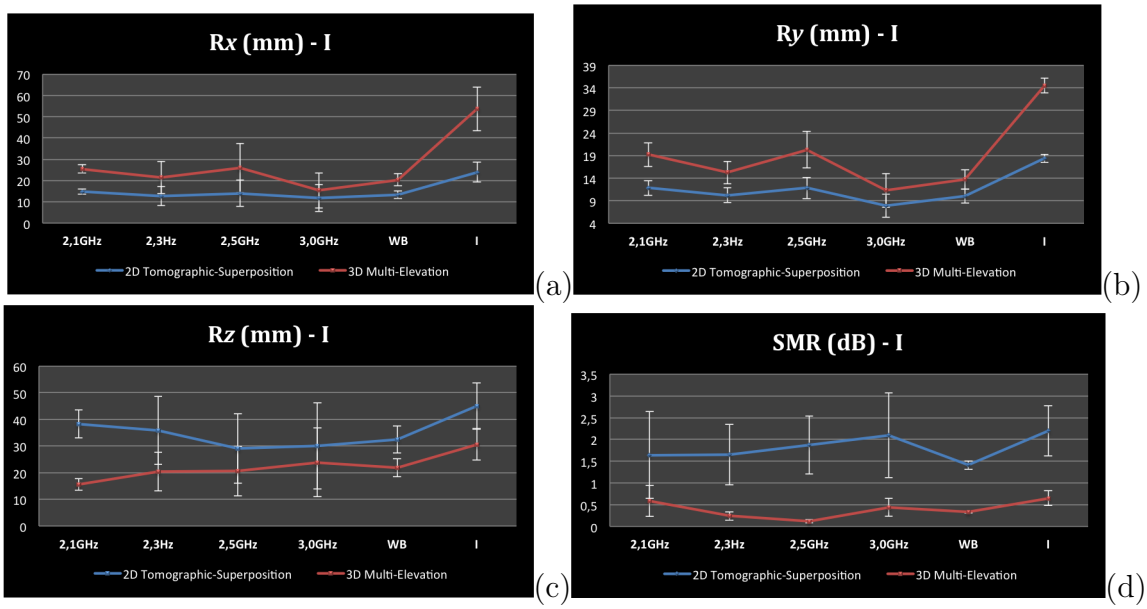

Figure 5.30: Comparison between metrics corresponding to TS and ME reconstructions. "WB" and "I" stands for WideBande and ILOG reconstructions.

From the comparison between the trends shown in Figure 5.30, we observe that, even in presence of very low dielectric contrast and large imaging planes spacing, ME algorithm is able to correctly reconstruct the object and mantain vertical resolution capability at all frequencies, whereas tomographic superposition tends to produce a wider object along the vertical direction. By the way, SMR performances of multi elevation algorithm are much lower than the tomographic superposition algorithm. As before, we note that ILOG reconstruction always increase the SMR and the FWHM aswell.

5.4.2 Heterogeneous medium reconstructions

In this final stage we have filled the fibroglandular phantom with an emulsion of oil and acetone, whose dielectric constant is equal to 5. We have inserted PATROCLO to perform this image reconstructions. In this case, the tumor was inserted in the adipose tissue.

External position

In this set of measurements, we have exploited a particular grid-configuration where the resulting reconstructed image is not symmetric in respect to the tumor plane. The five elevation planes are localized in a vertical range from -15 to +45mm from the antenna plane, spaced of 15mm.

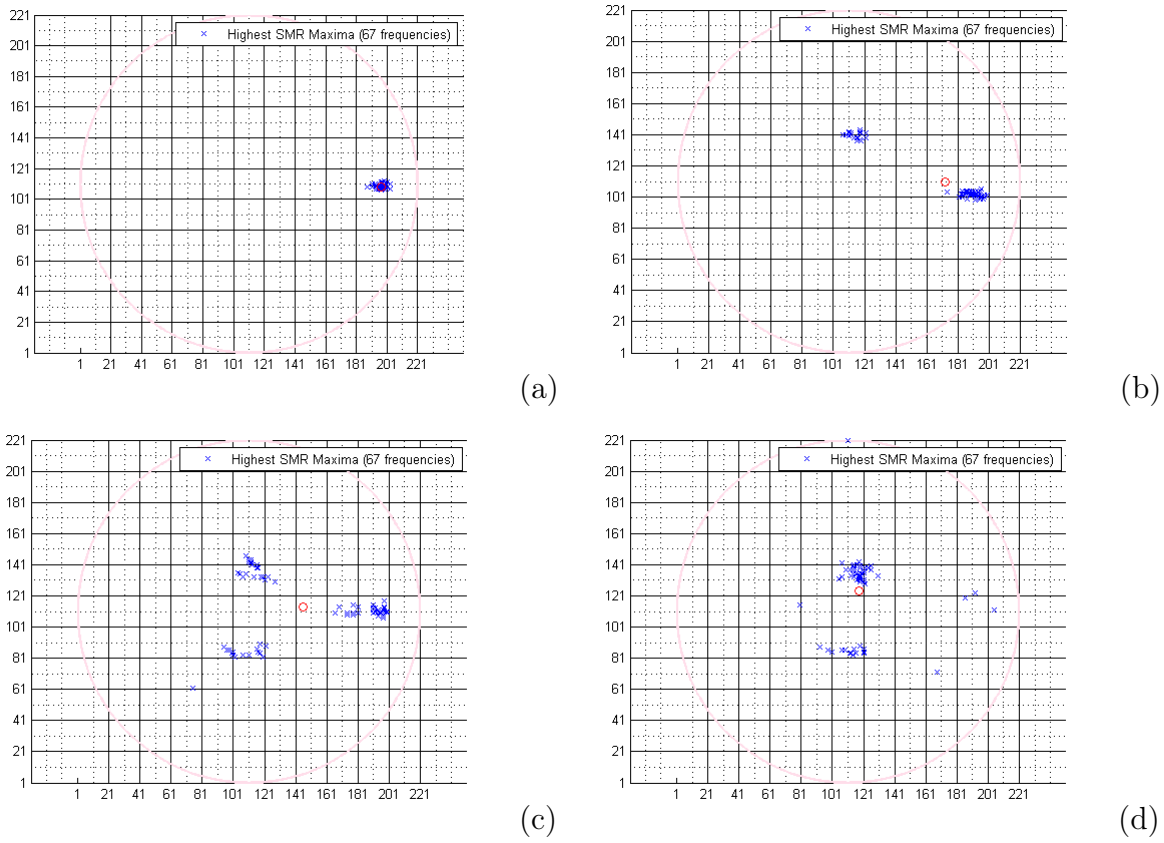

Figure 5.31: Distribution of the maxima corresponding to the highest SMR values in the range 2-3GHz, for different elevation planes: (a) 0mm, (b) 15mm, (c) 30mm, (d) 45mm. Coordinates are in image pixels.

In Figure 5.31 we observe that the tumor is correctly localized by all the frequencies when the tumor is located on the antenna plane. Moving away from this plane, maxima tend to spread out utill the distance becomes too high and maxima cluster around the fibroglandular phantom.

As before, we exploit the user interface to reconstruct over the frequencies at which correspon high SMR values and whose maximum is located in the area surrounding the tumor phantom. From this analysis performed on the three available datasets we obtain the value 2.0, 2.1, 2.2, 2.6, 2.7 GHz. The final reconstructions are shown in Figure 5.32, 5.33.

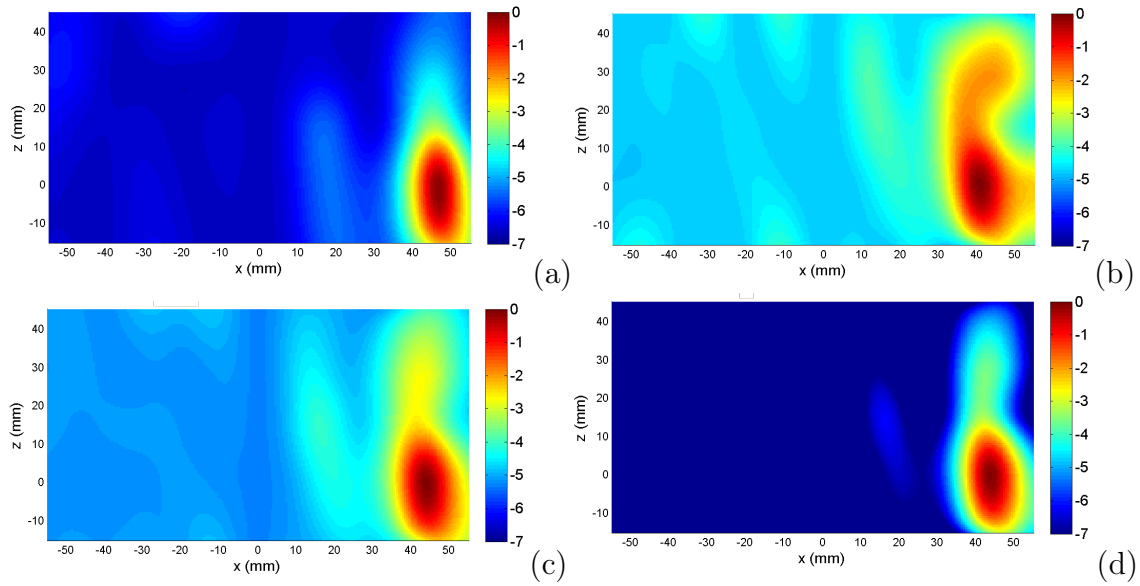

Figure 5.32: Samples of orhogonal-plane view of the tomographic superposition reconstruction method in the homogeneous breast-phantom with GLASSBURGER phantom. The reconstructions correspond to (a) 2.0GHz and (b) 2.7GHz. (d) and (e) are respectively WB and ILOG reconstructions.

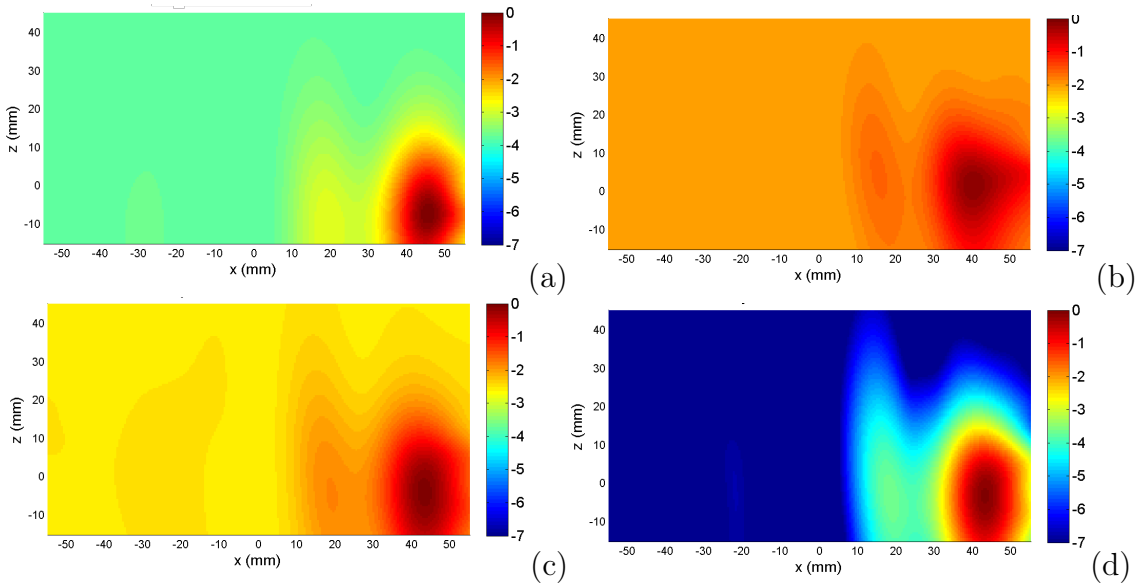

Figure 5.33: Samples of orhogonal-plane view of the multi-elevation reconstruction method in the homogeneous breast-phantom with GLASSBURGER phantom. The reconstructions correspond to (a) 2.0GHz and (b) 2.7GHz. (d) and (e) are respectively WB and ILOG reconstructions.

In this scattering configuration, the vertical resolution of ME algorithms appears to be much affected by the fibroglandular phantom in respect to tomographic superposition. This is probably due to the 3D propagator, because the signal obtained at

increasingly distant planes from tumor location is mainly given by the fibroglandular phantom, that tends to produce sparse, vertical artefacts. Figure 5.34 shows a comparison between the metrics computed on this scattering scenario.

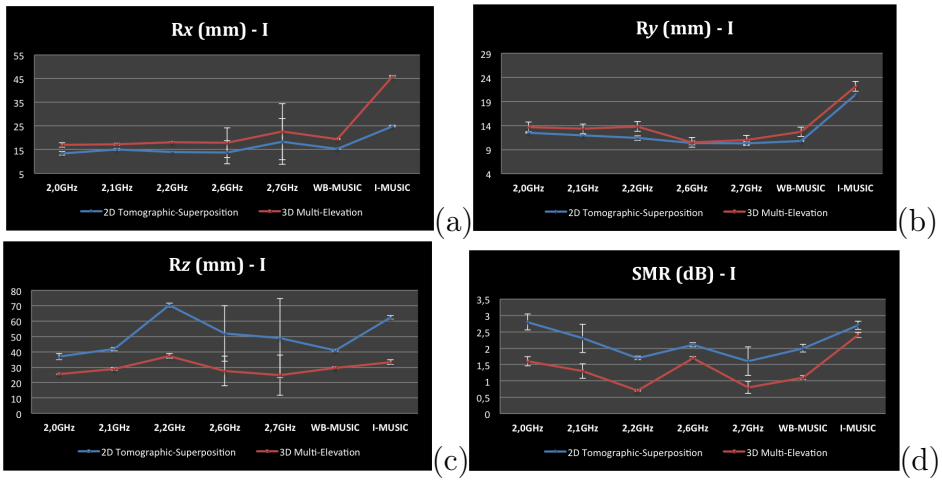

Figure 5.34: Comparison between metrics corresponding to TR and ME reconstructions.

Chapter 6

Conclusions

The work presented in this dissertation contributes to the major goal of developing a more effective diagnostic tool for detecting breast cancer in its earliest stages exploiting microwave imaging. Microwave imaging is novel imaging technique of growing popularity developed in the last decads. It owes its allure to the absence of ionizing radiations, and also offer secondary benefits, such as lower cost and patient comfort.

The goal of this thesis is to upgrade the existing instrumentation in order to develop a microwave imaging system able to perform automatic measurements and characterize its performances. In the preliminary stages, a specific wooden structure was created in order to host the breast phantom and all the instrumentation required to execute the measurements. We employed a VNA connected to a personal computer and to an half-wave sleeve dipole antenna to radiate microwaves and acquire the signal reflected by the breast phantom. This phantom is composed of a PVC cylinder (whose diameter equals to 110mm), that stands for the skin layer, immersed in seed oil that represent both the coupling medium and normal adipose breast tissue. Also, at its wall, it is possible to fix a 50mm diameter cylindric PVC tube that, being plugged in the lower side, can be filled with diffrents solution to simulate the fibroglandular tissue, where real breast cancers are usually located. This phantom was inserted only in the second stage of out measurment session. In our study, tumors are represented by tight PVC cylindric tubes of different sizes, which can be filled with different solutions. A crucial moment of our work was the proper selection of those solutions and emulsions to simulate an arbitrary number of scattering scenarios. In particular, we realized 14 different mixtures which were emploied to properly sample the behaviour of our instrumentation. We also realized a particular top for the breast phantom that was perforated in a specific points in which the tumor phantom was inserted. Moreover, this top was designed in order to host a pulley that was con-

nected to an high-precision motor through a belt in order to perform breast phantom rotations.

This mechanic structure is required because we explooted a particular acquisition system, called "monostatic configuration", in which the antenna acquires the reflected signal from different position around the imaging domain. For a matter of semplicity, in our system we fixed the antenna position and the breast phantom was rotated.

During the preliminary stage, a LabViews Virtual Instrument was specifically developed to drive the motor and the aquisition process. This software is able to automatically perform the signal acquisitions from an arbitrarly number of positions and over a selected range of frequencies. The development of this software was quite demanding, since we needed to syncronize two different instruments (VNA and the motor) whose LabView drivers couldn't be directly connected. Thanks to this software, every set of measurements can be achived in a few minutes so that we were able to performd a massive acquisition of data. Also, this software performed an automatic image reconstruction over a range of frequency selected by user interface, through TR-MUSIC algorithms.

In the following stage, we carried out three data acquisition in homogeneous medium for many different scatterer sizes and dielectric permittivity. The first goal was to carefully characterize the frequency working range of our imaging system. We found some facts based on the antenna signal trend, the evolution of the contrast in the reconstructed images and the target delocalization that the optimal working range was included between 2.5 and 3.2 GHz. Later, we studied the behaviour of our imaging system as a function of the scatterer diameter, position and its dielectric permittivity. For all the scatterer dimensions we found that, after a certain value of the dielecric parameters, the contrast of the image stops growing and reaches a plateau. This not intuitive result seems to be in accordance with the thoretical results found in literature.

Thereafter, we inserted the fibroglandualr phantom to perform measurements in the heterogeneous medium. We fixed the tumor dielectric permittivity and filled the fibroglandualr phantom with four mixtures of increasing dielectric properties. For each of those configurations, we performed measurements in three different configurations: the tumor inserted inside the fibroglandualr phantom , the tumor inserted in the adipose tissue in front of the fibroglandular phantom, and the tumor not inserted at all. From the anaysis of the results, we discovered that the fibroglandular phatom strongly degrades the image. In the external position, it was correctly reconstructed in the tested scenarios, whereas in the inter position the fibroglandular phantom

prevented the tumor detection.

Finally, we executed some measurements using a finite dimension scatterer in order to test the ability of a 3D reconstruction algorithm developed in our group that was previously tested only over synthetic data. We performed acqusitions in both homogeneous and heterogeneous medium exploiting our experimental system. Comparing two different 3D reconstruction approaches we found that through Tomographic Superposition we relatively high contrast images even if the spatial resolution degrades along the vertical axis. On the countrary, Multi Elevation technique mantains vertical resolution capability at all frequencies, whereas the corresponding SMR always assumes lower values than in the previous case.

Future works

Appendix A

Hertzian Dipole Antenna

The Hertzian dipole antenna is defined as an infinitesimal element excited with an alternating current. In practice a linear antenna can be approximated by a Hertz dipole if the linear antenna is of size much shorter ($l \ll \lambda$) and thinner ($a \ll \lambda$) than the wavelength, where l and a are respectively the length and the width of the antenna [59]. Thanks to this assumption, the spatial variation of the current can be considered constant.

Dipole current is given by definition as

$$\boldsymbol{I}(z') = \hat{\boldsymbol{a}}_{\boldsymbol{z}} I_0 \tag{A.1}$$

where I_0 is a constant value.

Since the Hertz dipole is small the vector potential $\boldsymbol{A}$ at point P is almost same as the Green's function multiplied by the volume integral of the current density:

$$\boldsymbol{A}(\boldsymbol{r}) = \mu_0\mu \int_V j(\boldsymbol{r'}) G_0(\boldsymbol{r}, \boldsymbol{r'}) dV' = \frac{\mu_0\mu}{4\pi} \int_V j(\boldsymbol{r'}) \frac{e^{\pm ik|\boldsymbol{r}-\boldsymbol{r'}|}}{|\boldsymbol{r}-\boldsymbol{r'}|} dV' = \hat{\boldsymbol{a}}_{\boldsymbol{z}} \frac{\mu_0\mu I_0 l}{4\pi r} e^{\pm ikr} \tag{A.2}$$

The final equality was reached reducing the colume integral into a line integral on a curve, being the Hertzian dipole and infinitesimal line-source positioned at the origin of the coordinate system ($\boldsymbol{r'} = 0$).

Since the coordinate system used for the antenna analysis is spherical, the components of the magnetic vector potential in spherical coordinates are given by

$$\begin{cases} A_r = A_z \cos\theta \\ A_\theta = -A_z \sin\theta \\ A_\phi = 0 \end{cases} \tag{A.3}$$

where $A_z = \frac{\mu_0 \mu I_0}{4\pi r} e^{\pm ikr}$.

Now, we can derive the expressions for the field $\boldsymbol{E}$, $\boldsymbol{H}$ applying the Lorentz gauge condition on the vector and scalar potential equations:

$$\begin{aligned} \boldsymbol{H}(\boldsymbol{r}) &= \tfrac{1}{\mu_0 \mu} \boldsymbol{\nabla} \times \boldsymbol{A}(\boldsymbol{r}) \\ \boldsymbol{E}(\boldsymbol{r}) = -\boldsymbol{\nabla}\phi(\boldsymbol{r}) - i\omega \boldsymbol{A}(\boldsymbol{r}) &= \tfrac{1}{i\omega \varepsilon_0 \varepsilon} \boldsymbol{\nabla} \times \boldsymbol{H}(\boldsymbol{r}) \end{aligned} \tag{A.4}$$

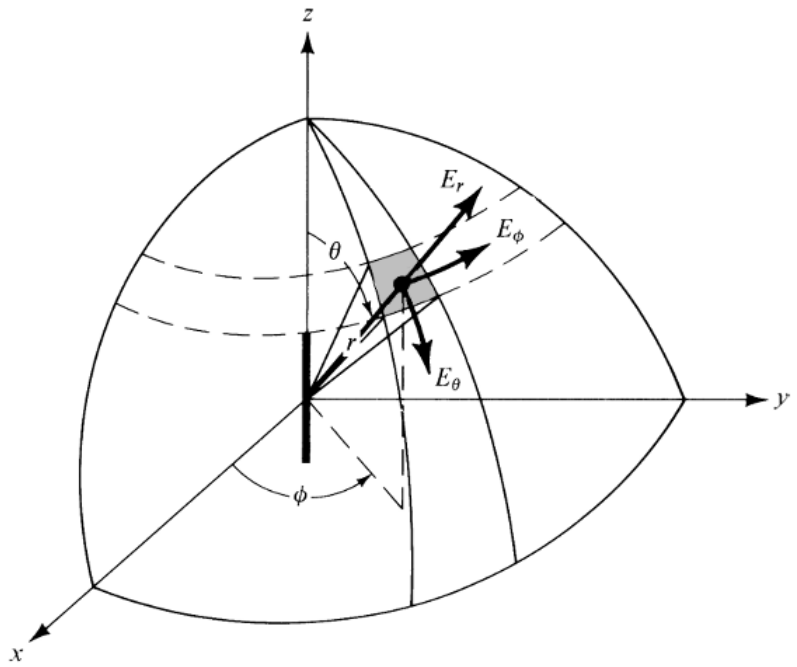

Figure A.1: Electric field components in spherical coordinates of an Hertzian dipole positioned symmetrically at the origin of the coordinate system and orientated along the vertical axis.

Exploiting the symmetry of the problem with respect to ϕ, we can obtain the field components though the expansion of $\boldsymbol{H}$ in spherical coordinates as follows

$$\begin{cases} H_\phi = \frac{ikI_0 l \sin\theta}{4\pi r}\left[1+\frac{1}{ikr}\right]e^{\pm ikr} \\ H_\phi = H_\theta = 0 \\ E_r = \frac{\eta I_0 l \cos\theta}{2\pi r^2}\left[1+\frac{1}{ikr}\right]e^{\pm ikr} \\ E_\theta = \frac{i\eta k I_0 l \sin\theta}{4\pi r}\left[1+\frac{1}{ikr}-\frac{1}{(kr)^2}\right]e^{\pm ikr} \\ E_\phi = 0 \end{cases} \tag{A.5}$$

where $\eta = \sqrt{\frac{\mu_0\mu}{\varepsilon_0\varepsilon}}$ is the wave impedence. These equations hold everywhere, except on the source itself, and can be devided in terms according to the dependence from r. Hence, we can define the field components depending from r^{-2} and r^{-3} as *inductive terms* and the componets depending from r^{-1} as *radiative terms*.

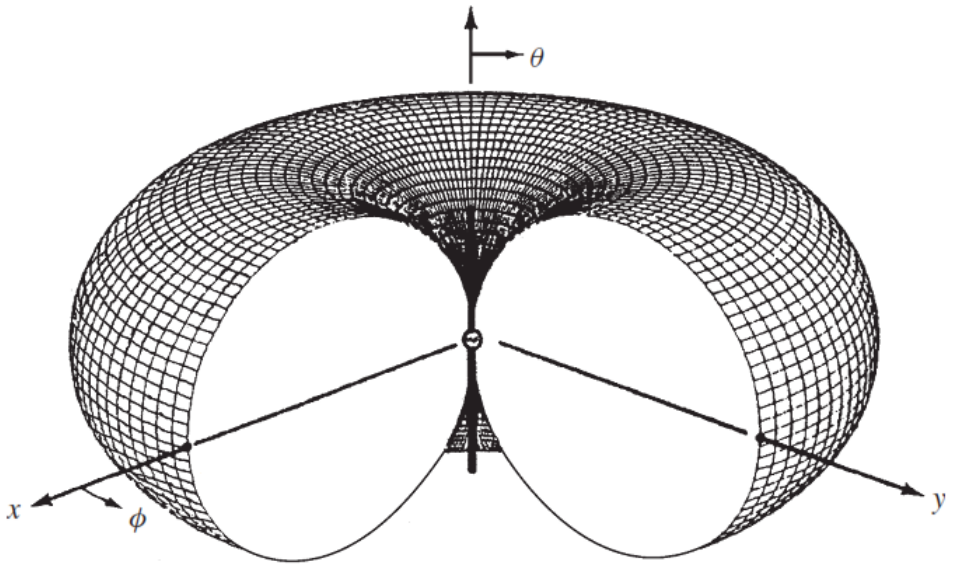

Figure A.2: Hertzian dipole radiation pattern.

Due to the different dependence from r, the radiation field propagates further away than inductive components, and for this reason the energy carried by the inductive field is stored near the antenna, whereas radiation fields provie energy propagation away from the antenna position. According to the value of (kr), we can approximate the field components in three different regions:

· Near-field approximation $(kr \ll 1)$

$$\begin{cases} E_r \simeq -\frac{i\eta I_0 l}{2\pi k r^3} e^{\pm ikr} \cos\theta \\ E_\theta \simeq -\frac{i\eta I_0 l}{4\pi k r^3} e^{\pm ikr} \sin\theta \\ H_\phi \simeq \frac{I_0 l}{4\pi r^2} e^{\pm ikr} \sin\theta \\ H_r = H_\theta = E_\phi = 0 \end{cases}$$

· Intermediate-field approximation ($kr > 1$)

$$\begin{cases} E_r \simeq \frac{\eta I_0 l}{2\pi k r^2} e^{\pm ikr} \cos\theta \\ E_\theta \simeq \frac{i\eta k I_0 l}{4\pi k r} e^{\pm ikr} \sin\theta \\ H_\phi \simeq i\frac{k I_0 l}{4\pi r} e^{\pm ikr} \sin\theta \\ H_r = H_\theta = E_\phi = 0 \end{cases}$$

· Far-field approximation ($kr \gg 1$)

$$\begin{cases} E_\theta \simeq \frac{i\eta k I_0 l}{4\pi k r} e^{\pm ikr} \sin\theta \\ H_\phi \simeq \frac{ik I_0 l}{4\pi r} e^{\pm ikr} \sin\theta \\ E_r \simeq E_\phi = H_r = H_\theta = 0 \end{cases}$$

Appendix B

Mie's Theory

The optical properties of a medium are characterized by its reflective index, and as lon as it is uniform, light will pass through the medium undeflected. If there are discrete variations of the refractive index due to the presence of particles, part of the radiation will be scattered in all directions. Scattering laws apply with equal validity to all the wavelengths and depend upon the specific value of the size parameter (called also form factor), that is defined as the ratio of the characteristic dimensions of the particle to the wavelength of the incoming wave. Apparently different phenomena, such as the study of the light scattering by water drops in meteorology or the aircrafts detection through radar applications, are indeed quite similar beacuse in each case the wavelength is of the same magnitude as that of the scatterer [60].

The theoretical investigation of electromagnetic scattering by small particles is of severe interest in different research fields. Scatterer samples emploied in scattering measurements are usually of complex shape and composition, leading to laborious mathematical models. By the way, much knowledge of scattering processes can be gained by looking at the theoretical scattering solutions for simplified geometries. For this pourpose, a various number of analytical solutions of the scattering of electromagnetic waves by semplified scatterers have been developed, such as spherical and other semplified variants [60]. The complete solution of the spherical scatterer interacting with an electromagnetic plane wave was developed by Gustav Mie in 1908. Mie's theory holds for scattering particles of every size, and describes situations where the size of the scattering particles is comparable to the wavelength of the incoming wave. When it is much bigger than the object size, Rayleigh scattering is obtained, that describes the behaviour of point type scattering particles.

Another fundamental scattering structure for which an analytical solution has been developed is the infinite cylinder [61]. If the length of the cylindrical scattering

structures is much larger than the diameter, the infinite cylinder approximation can be applied [62], which is the geometry exploited in this work, where the scatterer is represented by a tight and tall cylinder.

Schäfer et al. [63] developed a MATLAB package which contains different solutions for the scattering of electromagnetic radiation by a spherical or a cylindrical target, according Mie's theory. We are interested in the latter case, so we computed the scattering efficiency as a function of the scatterer diameter, for different values of its relative permittivity constant (Figure B.1). It is clearly visible that the scattering cross section grows with the diameter until it reaches a plateau. Here, it is approximatively constant for a tight range of diameters and then it starts bouncing, showing a slightly increasing trend. This effect is more evident for high values of dielectric relative permittivity, suggesting that the scattering cross section doesn't indefinitely increase beyond a limit given by the physical properties of the scattering scenario. Observing the figure carefully, it appears that the cross section corresponding to an high value of dielectric permittivity is inferior than the cross section of the target characterized by a lower ε. Hence, the behaviour of the cross section as a function of the dielectric constant, for a fixed diameter, is not necessarely increasing. In effect, from our experimental results we observe particular behaviors which are compatible with these observations.

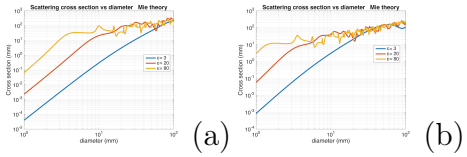

(a) (b)

Figure B.1: Scattering cross section of infinite cylinder target as a function of its diameter simulated for three different values of dielectric properies. The incident wave is characterized by a frequency equals to (a) 2.5GHz and (b) 7GHz. Comparing (a) and (b), we observe that the plateau is reached for different diameter due to the dipendence from the size parameter, defined as the rate between the diameter and the wavelength. As result, the cross section assumes bigger values in (b) that in (a) for the same diameter.

Bibliography

[1] Lindsey A. Torre, Freddie Bray, Rebecca L. Siegel, Jacques Ferlay, Joannie Lortet-Tieulent, Ahmedin Jemal. "Global Cancer Statistics, 2012". *CA: A Cancer Journal for Clinicians*. 65:87-108 (2015). Wiley Online Library.

[2] Jacques Ferlay, Isabelle Soerjomataram, Rajesh Dikshit, Sultan Eser, Colin Mathers, Marise Rebelo, Donald Maxwell Parkin, David Forman, and Freddie Bray. "Cancer incidence and mortality worldwide: sources, methods and major patterns in GLOBOCAN 2012". *International Journal of Cancer*, 136.5: E359-E386 (2015). Wiley Online Library.

[3] Associazione Italiana dei Registri TUMori AIRTUM. "ITACAN: Tumori in Italia, Versione 2.0." (2014). `http://www.registri-tumori.it`.

[4] Rebecca L. Siegel, Kimberly D. Miller, Ahmedin Jemal. "Breast cancer statistics, 2015". *CA: a cancer journal for Clinicians*, 65:5–29 (2015). American Cancer Society.

[5] Laszlo Tabar and Peter B Dean. "A new era in the diagnosis and treatment of breast cancer". *The Breast Journal*, 16.s1: S2-S4 (2010). Wiley Online Library.

[6] Phan T Huynh, Amanda M Jarolimek, and Susanne Daye. "The false-negative mammogram". *Radiographics*, 18.5: 1137-1154 (1998)

[7] Joann G Elmore, Mary B Barton, Victoria M Moceri, Sarah Polk, Philip J Arena, and Suzanne W Fletcher. "Ten-year risk of false positive screening mammograms and clinical breast examinations". *New England Journal of Medicine*, 338.16: 1089-1096 (1998). Mass Medical Soc.

[8] Amy Berrington de González and Sarah Darby. "Risk of cancer from di- agnostic X-rays: estimates for the UK and 14 other countries". *The lancet*, 363.9406: 345-351 (2004). Elsevier

[9] Wendie A Berg, Lorena Gutierrez, Moriel S NessAiver, W Bradford Carter, Mythreyi Bhargavan, Rebecca S Lewis, and Olga B Ioffe. "Diagnostic accuracy of mammography, clinical examination, US, and MR imaging in preoperative assessment of breast cancer ". *Radiology*, 233.3: 830-849 (2004). Radiological Society of North America.

[10] D. B. Kopans. "Breast Imaging". Lippincott Williams & Wilkins, 2007.

[11] Debra M Ikeda, Douglas R Baker, and Bruce L Daniel. "Magnetic resonance imaging of breast cancer: clinical indications and breast MRI reporting system". *Journal of Magnetic Resonance Imaging*, 12.6: 975-983 (2000). Wiley Online Library.

[12] S.M.W.Y. van de Ven, S.G. Elias, M.A.A.J. van den Bosch, P. Luijten, and W.P.Th.M. Mali, "Optical imaging of the breast", *Cancer Imaging*. 2008; 8(1): 206–215.

[13] J. H. Jacobi, L. E. Larsen and C. T. Hast, "Water-Immersed Microwave Antennas and Their Application to Microwave Interrogation of Biological Targets," *IEEE Trans. Microwave Theory Tech.*, vol. 27, pp. 70–78, Jan./ 1979.

[14] A. Joisel, J. Mallorqui, A. Broquetas, J. M. Geffrin, N. Joachimowicz, M. V. Iossera, L. Jofre and J. -C. Bolomey, "Microwave Imaging Techniques for Biomedical Applications," *IEEE Instrumen. Measure. Tech. Conf.*, 1999.

[15] Susan C Hagness, Allen Taflove, and Jack E Bridges. "Two-dimensional FDTD analysis of a pulsed microwave confocal system for breast cancer detection: Fixed-focus and antenna-array sensors". *Biomedical Engineering*, IEEE Transactions on 45.12: 1470-1479 (1998). IEEE.

[16] Xu Li and Susan C Hagness. "A confocal microwave imaging algorithm for breast cancer detection". *Microwave and Wireless Components Letters*, IEEE, 5.6: 509-513 (2001). IEEE.

[17] Susan C Hagness, Allen Taflove, and Jack E Bridges. "Three-dimensional FDTD analysis of a pulsed microwave confocal system for breast cancer detection: Design of an antenna-array element". *Antennas and Propagation*, IEEE Transactions on 47.5: 783-791 (1999). IEEE.

[18] M. Pastorino, *Microwave Imaging* , John Wiley & Sons.

[19] D. Faktorová. "Microwave Characterization of Frequency and Temperature Dependences of Beef Bone Dielectric Properties Using Waveguide Measurement System". Proceedings Measurement '09 Smolenice, Slovak Republic, pp. 402-405, (2009).

[20] Sverre Grimnes, Oslo Rikshospitalet, and Norway Herman P Schwan. "Interface phenomena and dielectric properties of biological tissue". 20: 2643-2653 (2002).

[21] Camelia Gabriel. "Compilation of the Dielectric Properties of Body Tissues at RF and Microwave Frequencies" (1996).

[22] Camelia Gabriel, Sami Gabriel, and E Corthout. "The dielectric properties of biological tissues: I. Literature survey". *Physics in medicine and biology*, 41.11: 2231 (1996). IOP Publishing.

[23] Sami Gabriel, RW Lau, and Camelia Gabriel. "The dielectric properties of biological tissues: II. Measurements in the frequency range 10 Hz to 20 GHz". *Physics in medicine and biology*, 41.11: 2251 (1996). IOP Publishing.

[24] Sami Gabriel, RW Lau, and Camelia Gabriel. "The dielectric properties of biological tissues: III. Parametric models for the dielectric spectrum of tissues". *Physics in medicine and biology*, 41.11: 2271 (1996). IOP Publishing.

[25] Mariya Lazebnik, Leah McCartney, Dijana Popovic, Cynthia B Watkins, Mary J Lindstrom, Josephine Harter, Sarah Sewall, Anthony Magliocco, John H Booske, Michal Okoniewski, et al. "A large-scale study of the ultrawideband microwave dielectric properties of normal breast tissue obtained from reduction surgeries". *Physics in medicine and biology*, 52.10: 2637 (2007). IOP Publishing.

[26] Mariya Lazebnik, Dijana Popovic, Leah McCartney, Cynthia B Watkins, Mary J Lindstrom, Josephine Harter, Sarah Sewall, Travis Ogilvie, Anthony Magliocco, Tara M Breslin, et al. "A large-scale study of the ultrawideband microwave dielectric properties of normal, benign and malignant breast tissues obtained from cancer surgeries". *Physics in Medicine and Biology*, 52.20: 6093 (2007). IOP Publishing.

[27] Lazebnik M, Madsen E L, Frank G R and Hagness S C 2005 "Tissue-mimicking phantom materials for narrowband and ulrawideband microwave applications" Phys. Med. Biol. 50 4245–58.

[28] Earl Zastrow, Shakti K. Davis, Mariya Lazebnik, Frederick Kelcz, Barry D. Van Veen, , and Susan C. Hagness "Development of anatomically realistic numerical breast phantoms with accurate dielectric properties for modeling microwave interactions with the human breast," IEEE *Transactions on Biomedical Engineering*, vol. 55, no. 12, December 2008.

[29] M. Clemens And T. Weiland "Discrete electromagnetism with the finite integration technique," Progress In Electromagnetics Research, Pier 32, pp. 65–87, 2001.

[30] Meaney, P.M. ; Thayer Sch. of Eng., Dartmouth Coll., Hanover, NH, USA ; Fanning, M.W. ; Li, Dun ; Poplack, Steven P. et al. "A clinical prototype for active microwave imaging of the breast". *Microwave Theory and Techniques*, 1841 - 1853 (2000).

[31] Ralph O Schmidt. "Multiple emitter location and signal parameter estimation". *Antennas and Propagation*, IEEE Transactions on, 34.3: 276-280 (1986). IEEE.

[32] Heinz Werner Engl, Martin Hanke, A. Neubauer. *Regularization of Inverse Problems*

[33] Anthony J. Devaney, Edwin A. Marengo and Fred K. Gruber, "Time-reversal-based imaging and inverse scattering of multiply scattering point targets ", *Journal of the Acoustical Society of America*

[34] M. O'Halloran, M. Glavin, and E. Jones, E ects of broglandular tissue distribution on data-independent beamforming algorithms," Progress In Electromagnetics Research, Vol. 97, 141-158, 2009. doi:10.2528/PIER09081701

[35] Klemm, M., et al. Improved delay-and-sum beamforming algorithm for breast can- cer detection." International Journal of Antennas and Propagation 2008 (2008).

[36] Bond, Essex J.; Li, Xu; Hagness, S.C.; Van Veen, B.D., Microwave imaging via space-time beamforming for early detection of breast cancer," in Antennas and Propagation, IEEE Transactions on , vol.51, no.8, pp.1690-1705, Aug. 2003 doi: 10.1109/TAP.2003.815446

[37] P. Kosmas et al. "Time reversal with the FDTD method for microwave breast cancer detection". *Transactions on Microwave Theory and Techniques*

[38] M. E. Yavuz and F. L. Teixeira. “Ultrawideband Microwave Sensing and Imaging Using Time-Reversal Techniques”.

[39] Anthony J Devaney. “Super-resolution processing of multi-static data using time reversal and MUSIC”. *J. Acoust. Soc.* Am (2000).

[40] Panagiotis Kosmas and Carey M Rappaport. “A matched-filter FDTD-based time reversal approach for microwave breast cancer detection”. *Antennas and Propagation*, IEEE Transactions on 54.4: 1257-1264 (2006). IEEE.

[41] N. Joachimowicz, C. Pichot and J. -P. Hugonin, “Inverse Scattering: An Iterative Numerical Method for Electromagnetic Imaging,” IEEE *Trans. Antennas Propagat.*, vol. 39, pp. 1742–1752, Dec. 1991.

[42] A. Franchois, C. Pichot. “Microwave Imaging–Complex Permittivity Reconstruction with a Levenberg-Marquardt Method,” IEEE *Trans. Antennas Propagat.*, vol. 45, pp. 203–215, Feb. 1997.

[43] Paul M Meaney, Keith D Paulsen, Alexander Hartov, and Robert K Crane. “An active microwave imaging system for reconstruction of 2-D electrical property distributions”. *Biomedical Engineering*, IEEE Transactions on 42.10: 1017-1026 (1995). IEEE.

[44] Hanoch Lev-Ari and AJ Devancy. “The time-reversal technique re-interpreted: Subspace-based signal processing for multi-static target location”. 509-513 (2000). IEEE.

[45] Fred K Gruber, Edwin A Marengo, and Anthony J Devaney. “Time-reversal imaging with multiple signal classification considering multiple scattering between the targets”. *The Journal of the Acoustical Society of America* 115.6: 3042-3047 (2004). Acoustical Society of America.

[46] Grandi, Massimiliano, et al. Breast microwave imaging with monostatic and multistatic approaches: Numerical simulations with MUSIC reconstruction." *Electromagnetics in Advanced Applications* (ICEAA), 2015 International Conference on. IEEE, 2015.

[47] David W. Winters, Jacob D. Shea, Panagiotis Kosmas, Barry D. Van Veen, and Susan C. Hagness. “Three-Dimensional Microwave Breast Imaging: Dispersive Dielectric Properties Estimation Using Patient-Specific Basis Functions”. *Medical Imaging.*

[48] Raffaele Solimene, Giuseppe Ruvio, Angela Dell'Aversano, Antonio Cuccaro, Max J Ammann, and Rocco Pierri. "Detecting point-like sources of unknown frequency spectra". Progress In Electromagnetics Research B, 50: 347-364 (2013). EMW Publishing.

[49] `https://en.wikipedia.org/wiki/Principal_component_analysis`

[50] Wikipedia: `https://en.wikipedia.org/wiki/Dipole_antenna`

[51] G. Ruvio, R. Solimene, A. Cuccaro, J.E. Browne, D. Gaetano and M.J. Ammann. "Experimental Microwave Breast Cancer Detection with Oil-on-Gelatin Phantom"

[52] "Introduction to Network Analyzer Measurements", National Instruments.

[53] Kaneyuki Kurokawa. "Power waves and the scattering matrix". *Microwave Theory and Techniques*, IEEE Transactions on 13.2: 194-202 (1965). IEEE.

[54] "Agilent Network Analyzer Basics", Agilent Technologies.

[55] John Edward Daniel. «Development of enhanced multiport network analyzer calibrations using non-ideal standards» (2005). American Studies Commons.

[56] Elise C. Fear, Member, IEEE, Xu Li, Student Member, Susan C. Hagness, Maria A. Stuchly, "Confocal Microwave Imaging for Breast Cancer Detection: Localization of Tumors in Three Dimensions", *TRANSACTIONS ON BIOMEDICAL ENGINEERING*, vol. 49 no. 8 august 2002

[57] Musca L. "TOMOGRAPHIC 3D RECONSTRUCTION THROUGH LINEAR INVERSION FOR BREAST MICROWAVE IMAGING"

[58] `http://hypertextbook.com/facts/2006/TingTingLuo.shtml`

[59] `http://nptel.ac.in/courses/117101057/downloads/lec48.pdf`

[60] Kerker M. The scattering of light and other electromagnetic radiation. New York: Academic Press; 1969.

[61] Bohren CF, Huffman DR. Absorption and scattering of light by small particles. New York: Wiley- Interscience; 1998.

[62] Wang RT, van de Hulst HC. Application of the exact solution for scattering by an infinite cylinder to the estimation of scattering by a finite cylinder. Appl Opt 1995;34(15):2811–21.

[63] J. Schafer, S.-C. Leeb, A. Kienle. "Calculation of the near fields for the scattering of electromagnetic waves by multiple infinite cylinders at perpendicular incidence"